https://doi.org/10.5194/essd-2026-762
Preprint. Discussion started: 6 November 2026
© Author(s) 2026. CC BY 4.0 License.



Open Access Earth System Science Data Discussions

Long-term time series of ground-based NDACC FTIR trace gases at Paris between 2011 and 2022

Hao. Fu[1], Pascal Jeseck[1], Christof Janssen[1], Corinne Boursier[1], Christian Rouillé[1], Patrick Marie-Jeanne[1], Julien Rozé[1], Tamer Abou Karroum[1] and Yao Té[1]

[1]Sorbonne Université, CNRS, MONARIS-IPSL, UMR8233, F-75005 Paris, France

Correspondence to: Yao Té (yao-veng.te@sorbonne-universite.fr) and Hao FU (hao.fu@sorbonne-universite.fr)

Abstract. We present long-term atmospheric trace gas measurements at Paris (48°50′04″ N, 2°21′02″ E; 60 m a.s.l.), using ground-based remote sensing technique and covering the period 2011-2022. The Fourier Transform Spectrometer of the Paris station (FTS-Paris) has been operated regularly since 2011 and has been part of the Total Carbon Column Observing Network (TCCON) since 2014. It recently joined the Network for the Detection of Atmospheric Composition Change – InfRared Working Group (NDACC-IRWG). Here we describe the instrument setup, the automated operation mode, and the SFIT4 retrieval strategy for ten Paris NDACC-IRWG products: CH_4, N_2O, CO, C_2H_6, H_2CO, NO_2, OCS, HCl, HF and HCN. The nominal retrieval settings were selected by comparing and evaluating the OEM and TP methods, using spectral fit quality, vertical profiles, degrees of freedom, averaging kernels, and retrieval errors as criteria. Data quality is assessed through error characterization, instrument line shape sensitivity study, comparison with previous PROFFIT9 retrievals, and evaluation of the post-processing filtering criteria. Retrieval noise dominates the random error, while spectroscopic uncertainties are the main source of the systematic error. Post-processing filtering removes about 2–6% of data, mostly outliers. The 2011-2022 time series show increasing trends for CH_4 and N_2O, decreasing trends for CO, C_2H_6, H_2CO, NO_2 and OCS, and an undefined long-term evolution for HCl. HF and HCN records only cover the 2018-2022 period and derived trends require caution. The Paris FTIR measurements have been archived in the NDACC data repository and on Zenodo using the Hierarchical Data Format version 4 (HDF4).

1 Introduction

Monitoring atmospheric constituents is vital for understanding climate change, air quality, and their impacts on ecosystems and society. Despite their low concentrations, trace gases such as carbon dioxide (CO_2), methane (CH_4), ethane (C_2H_6), and nitrous oxide (N_2O) play crucial roles in atmospheric chemistry and radiative forcing. Precise continuous observations of these gases provide crucial information for quantifying emissions, evaluating atmospheric models, and validating satellite measurements used in global climate assessments. They also provide data support for the development of policies aiming at sustainable development.

https://doi.org/10.5194/essd-2026-762
Preprint. Discussion started: 6 November 2026
© Author(s) 2026. CC BY 4.0 License.



Fourier Transform Infrared (FTIR) spectroscopy represents a mature and widely deployed technique for atmospheric observation via ground-based and spaceborne instruments. The measurement of high-resolution solar absorption spectra allows for retrieving multiple trace gases with high precision. Through forward modelling and retrieval strategies applied to specific spectral regions targeting different gases, the atmospheric concentrations of multiple trace gases can be retrieved. Long-term FTIR measurements, in particular, allow the detection of both short-term variations and long-term trends of various species relevant to climate and air quality (Hase et al., 2004; Kohlhepp et al., 2012; Vigouroux et al., 2018; Wunch et al., 2016; Zhou et al., 2016).

The FTIR spectrometer in Paris (FTS-Paris) operates within two major international ground-based networks. The Total Carbon Column Observing Network (TCCON; Wunch et al., 2011) employs near-infrared (NIR) solar spectra to retrieve column densities of key greenhouse gases (e.g., CO_2, CH_4, and N_2O), serving as a primary reference for satellite calibration and validation. The Network for Detection of Atmospheric Composition Change – Infrared Working Group (NDACC-IRWG, De Mazière et al., 2018) operates in the mid-Infrared (MIR) region and focusses on the long-term monitoring of stratospheric and tropospheric components to investigate atmospheric trends, transport, and chemical processes.

The FTS-Paris instrument (Té et al., 2010) has been installed on the Campus Pierre et Marie Curie of Sorbonne Université in 2006. It is located in the heart of the downtown Paris and provides a unique urban perspective. Paris is the third largest European megacity with more than 2 million inhabitants in the city of Paris covering an area of 105 km^2 and with about 12 million inhabitants in the greater Paris area (Île de France region) that covers about 12 000 km^2. Similar to other megacities, large emissions of anthropogenic pollutants and greenhouse gases are expected. The city lies on the Seine River in a general fault basin with low surrounding hills, which can favour accumulation of pollutants under certain meteorological conditions. Regular atmospheric observations based on the FTS-Paris instrument have been performed since 2011 (Té et al., 2010, 2012), covering the spectral ranges of both networks.

FTS-Paris has joined the TCCON network in 2014 and is part of the NDACC-IRWG since 2024. Within the TCCON network, FTS-Paris data have contributed to a series of studies focusing on greenhouse gases and carbon cycle processes. For instance, these measurements supported the validation of satellite observations, for example OCO-2 (Orbiting Carbon Observatory; Taylor et al., 2022) or TROPOMI Sentinel-5P (Sha et al., 2021) and were utilised to quantify carbon dioxide emissions from northern forest fires through the assimilation of TROPOMI and TCCON observations (Voshtani et al., 2025). Furthermore, data from FTS-Paris have been employed in recent assessments of global methane fluxes (Tsuruta et al., 2025) and investigations into interannual variations in global satellite-observed carbon dioxide (Guan et al., 2023).

In the frame of NDACC, FTS-Paris data have been employed to investigate several key trace gases retrieved from mid-Infrared spectra, including CO, C_2H_6, H_2CO, and OCS. These datasets have facilitated analyses of seasonal variations across multiple FTIR sites (Té et al., 2016), coordinated multi-species assessments during COVID-19 lockdowns across NDACC stations (Ortega et al., 2023), and contributed to global OCS trend analyses across different atmospheric layers (Hannigan et al., 2022a). For H_2CO, FTS-Paris data have been incorporated into the following studies: a unified FTIR study (Vigouroux et al., 2018), OMI Collection 4 product evaluation (Ayazpour et al., 2025), satellite validation of OMPS-NM data (Kwon et al., 2023),

https://doi.org/10.5194/essd-2026-762
Preprint. Discussion started: 6 November 2026
© Author(s) 2026. CC BY 4.0 License.



Open Access Earth System Science Data Discussions

European weekly VOC (Volatile Organic Compound) flux estimation based on TROPOMI H_2CO (Oomen et al., 2024), and bias correction of OMI H_2CO data (Müller et al., 2024).

All previous FTS-Paris NDACC-related studies were based on retrievals using the PROFFIT9 software (Hase et al., 2004), employing earlier versions of spectral databases (e.g., HIgh-resolution TRANsmission (HITRAN) 2008 (Rothman et al., 2009)) and previous prior models 41-year Whole Atmosphere Community Climate Model from 1980 to 2020 (WACCM6, Marsh et al., 2013). While both PROFFIT9 and SFIT4 are officially recognised inversion tools by the NDACC-IRWG, the majority of NDACC sites currently utilise SFIT4, which has been updated from its predecessor SFIT2 (Hase et al., 2004; Pougatchev et al., 1995; Rinsland et al., 1998). To ensure consistency and minimise potential systematic differences with other sites, we have transitioned to use SFIT4 for FTS-Paris spectra inversions. This paper presents, for the first time, NDACC-Paris results obtained using SFIT4 v1.0.21, which incorporates the updated HITRAN 2020 (Gordon et al., 2022) spectral database and the latest NDACC-IRWG a priori profile set, commonly referred to as IRWG7, which is derived from 61-year Whole Atmosphere Community Climate Model from 1980 to 2040 (Gettelman et al., 2019).

The paper is organised around the construction and evaluation of the Paris NDACC-IRWG data product. Section 2 describes the station, instrument configuration, and automated operation. Section 3 summarizes the retrieval principles needed to understand the subsequent choices. Section 4 then gives the reproducible retrieval recipe: the forward model inputs, the inversion strategy, the use of representative OEM and TP examples, and the data quality checks that support the routine product. Section 5 presents the automated SFIT4 processing and the 2011-2022 timeseries. Section 6 provides summary and conclusions.

2 Description of the Paris station

2.1 Description of the FTS-Paris spectrometer

The FTS-Paris instrumentation has been well described in previous studies (Koshelev, 2018; Té et al., 2010, 2012). We therefore give only a short account with focus on recent modifications and improvements. The Bruker Optics IFS 125HR (FTS-Paris; 48°50′04″ N, 2°21′02″ E; 60 m a.s.l.) (Té et al., 2010) is a Michelson interferometer (Griffiths and de Haseth, 2006), installed on the 5th floor of the Qualair station in central Paris (https://qualair.fr/), an experimental research platform dedicated to observing the chemical and dynamic variability of the atmosphere using complementary in situ measurements and remote sensing observations. The spectrometer is coupled to a dedicated sun tracker on the rooftop, as shown in Fig. 1. The sun-tracker consists of two plane mirrors that rotate along an azimuth and elevation axis driven by two stepper motors. The first mirror can rotate around the horizontal axis to follow the elevation position of the Sun and the second is fixed on the base plate, which can rotate around the vertical axis to follow the azimuth of the Sun. The arrangement of the two mirrors guarantees that the solar light is always reflected downward with a constant direction into the spectrometer, independent of the solar position. A dome from Astroplast (www.lichtbauelemente.de) shields the sun-tracker from environmental factors like rain and wind when it is not in use. To start sun tracking, the system calculates the expected position of the sun using local

https://doi.org/10.5194/essd-2026-762
Preprint. Discussion started: 6 November 2026
© Author(s) 2026. CC BY 4.0 License.

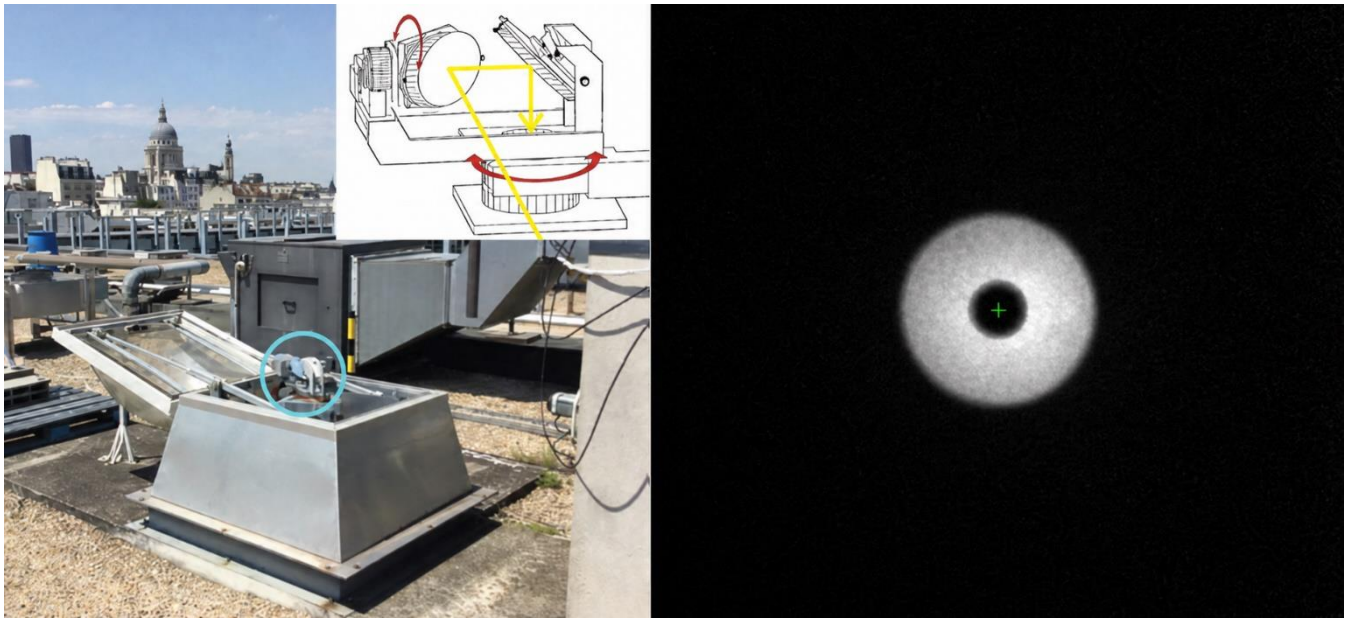


Figure 1: Left: a photo of the sun-tracker and its protective dome of the FTS-Paris instrument, top right is a schematic setup of the tracker reproduced from Gisi et al. (2011, Fig. 3). Right: Camtracker image capturing the sun image centre through the spectrometer input collimator iris centre.

coordinates and astronomical ephemerides data. Fine tracking is then accomplished by a charge-coupled device (CCD) camera and a feedback loop software, called Camtracker (Gisi et al., 2011), which keeps the sun image centre on the centre of the spectrometer input collimator iris (see right panel of Fig. 1). The whole system achieves a high pointing accuracy, within 1 arcminute and compensates the apparent daily trajectory of the sun.

The mid-infrared spectra are recorded by passing the light through an entrance aperture of 0.8 mm before a calcium fluoride (CaF_2) beam splitter onto a liquid-nitrogen cooled InSb detector combined with one of 4 possible optical filters to cover the spectral region from 1850 to 5000 cm^{-1}, see Table 1. Table 1 summarizes the spectral acquisition settings, the retrieved NDACC-IRWG species, and the instrumental setups. The optical filter NDACC11 has been used throughout at the beginning of our NDACC-IRWG activities. Other optical filters (NDACC01, NDACC02 and NDACC05) have been installed in June 2018. Until March 2015, NDACC-IRWG solar spectra were acquired with a spectral resolution of 0.0035 cm^{-1} (258 cm of maximum optical path difference, MPD). Since then, the resolution has been reduced to 0.005 cm^{-1} (MPD 180 cm). As the instrument has operated in both NDACC-IRWG and TCCON configuration, the photoconductive mercury–cadmium telluride (MCT) detector covering 650-1300 cm^{-1} is no longer used for NDACC activities, because TCCON measurement require a CaF_2 beam splitter which cuts the radiation below 1200 cm^{-1}. The recording scheme is the following: 8 TCCON, 8 TCCON

https://doi.org/10.5194/essd-2026-762
Preprint. Discussion started: 6 November 2026
© Author(s) 2026. CC BY 4.0 License.



LowRes[1], 2 NDACC11, 2 NDACC05, 2 NDACC02 and 2 NDACC01 spectra. The acquisition of one NDACC spectrum takes around 3 minutes. A full sequence of TCCON and NDACC measurements takes around 35 minutes. Figure 2 shows an example of spectra measured with the different optical filters.

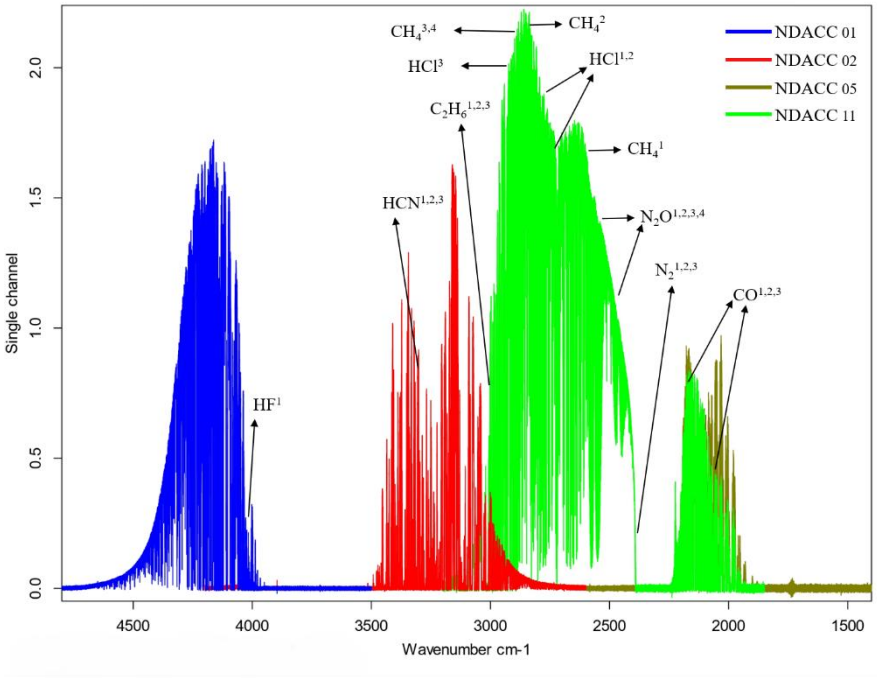


Figure 2: Example of the solar spectra measured with the FTS-Paris using 4 different filters. Standard NDACC-IRWG products are indicated together with the micro-windows used for the retrieval. The upper index attached to the molecular formula represents the micro-window where the gas is retrieved.

Table 1: Description of FTS-Paris atmospheric spectra in NDACC-IRWG range and history.

	NDACC optical filters			
	NDACC11	**NDACC02**	**NDACC05**	**NDACC01**
Spectral region (cm^{-1})	1850-3200	2600-4200	1400-2600	3500-4800
Focal length (mm)		418.00		
Aperture Setting (mm)		1 or 1.15		
Beam splitter setting		CaF_2		
Scan time (s)		143.66		
Number of scans		2		
Resolution (cm^{-1})		0.005		
NDACC retrieved species	CO, C_2H_6, HCl, CH_4, N_2O	CO	HCN	HF

NDACC 11 setup list						
Setup	Resolution (cm^{-1})	Aperture Setting (mm)	Field of View	Start	End	Scan time (**s**)

[1] TCCON LowRes indicates a measurement at lower spectral resolution (0.5 cm^{-1}) corresponding to EM27/SUN spectrometer, in order to compare with collocated EM27/SUN measurements.

https://doi.org/10.5194/essd-2026-762
Preprint. Discussion started: 6 November 2026
© Author(s) 2026. CC BY 4.0 License.



			(FOV, mrad)			
1	0.0035	1.0	2.3923	16/10/2007	14/10/2009	204.63
				16/02/2010	04/03/2013	204.63
2	0.0035	0.8	1.9139	02/04/2013	24/09/2013	204.64
				21/10/2013	13/04/2015	71.86
3	0.005	0.8	1.9139	15/04/2015	28/12/2017	205.27
				20/06/2018	03/06/2024	143.66
4	0.005	1.0	2.3923	03/06/2024	Up to now	143.66
NDACC01, 02 and 05 setup list						
1	0.005	0.8	1.9139	20/06/2018	03/06/2024	143.66
2	0.005	1.15	2.7512	03/06/2024	Up to now	143.66

2.2 Description of the automation software

In order to optimize spectra acquisition for both, the TCCON and NDACC-IWRG configurations, we have developed the FTSpectRA software (Rozé et al., 2024) that allows for automatic operation of the FTS-Paris since May 2024. The FTSpectRA software based on a state machine is written in Python for easy distribution and maintenance and its goal is to minimize manual intervention. It controls the whole instrumentation chain and comprises four main modules: a security device interface, a sun-tracking system interface, a spectrometer interface, and a pyranometer interface (see Fig. 3), which will be described in the following.

The sun-tracker installed on the rooftop requires protection from rain and heavy winds. This protection is provided by a dome, which opens during measurements (Fig. 1, left panel). To automate the dome operation, independent sensors monitor the solar flux, the mechanical positioning of the sun-tracker and the rainfall. A dedicated MCU (Microcontroller Unit) board (Fig. 3, orange box) manages the communication with these sensors via a RS232 serial interface, ensuring safety through built-in checks and redundancies. For instance, the dome remains locked unless the sun-tracker is in its parking position, because the actuator that controls opening or closing the dome could damage the sun-tracker if it is not in parking position during opening or closing. A Kipp & Zonen SMP3-A pyranometer (Kipp & Zonen, 2023) provides solar radiation flux data. By comparing the measured flux with a model (Aigner et al., 2023; Duchon and O'Malley, 1999; Meyers and Dale, 1983), the system (Fig. 3, green box) determines whether to start measurements. SMP3-A pyranometer acquisitions run continuously. Averaged readings and hysteresis are used to reduce sensitivity to brief cloud bursts and prevent on-off oscillations near the model threshold. Both, the averaging window and the number of pyranometer measurements (greater or lower than a threshold) to trigger opening or closing of dome are configurable (hysteresis). FTSpectRA will open the dome to start measurements even during relatively short periods of favourable conditions. It will halt them as soon as rain is detected or the solar flux is under the threshold.

However, the Camtracker software lacks an API, making external interfacing challenging. We solved this problem by running Camtracker commands via the operating system. The key challenge was to retrieve the system status which is sent to Camtracker via User Datagram Protocol (UDP) messages. To obtain the status information, we implemented a method to sniff

https://doi.org/10.5194/essd-2026-762
Preprint. Discussion started: 6 November 2026
© Author(s) 2026. CC BY 4.0 License.

and decode the UDP frames using scapy (https://scapy.readthedocs.io/en/latest/), therefore enabling real-time system state monitoring. FTSpectRA also launches measurements using Bruker's OPUS software (Fig. 3, blue box) via its HTTP-based Application Program Interface (API). This API allows external control, enabling FTSpectRA to execute OPUS macros. To enhance reliability, we have also established direct communication between FTSpectRA and the spectrometer control server. This ensures system recovery in case of an OPUS crash. OPUS itself does not provide a signal to the spectrometer to stop acquisition if it fails, therefore leaving the instrument in an unknown state after a software crash. We have therefore implemented a reset mechanism.

Before the introduction of FTSpectRA (between May 2020 and May 2024), measurements were available on (31 ± 11) % of the annual operational days, where operational days denote days without any instrumental failure, and the reported uncertainties represent the observed standard deviations. After the implementation of FTSpectRA (June 2024 to June 2026), this fraction increased to (56 ± 5) %. This corresponds to an approximately 81% relative increase compared with the pre-FTSpectRA period. This improvement in operational efficiency allows us to achieve a greater number of measurements per year.

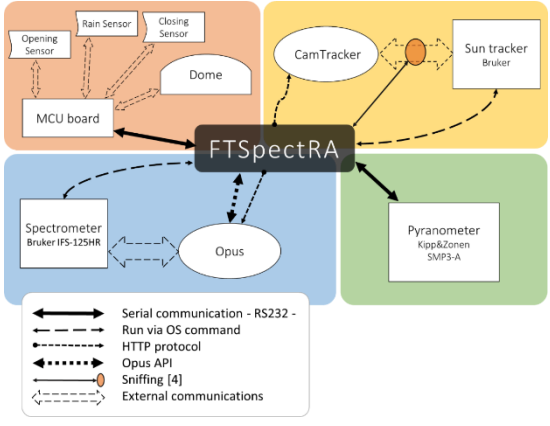


Figure 3: Operation scheme of the FTSpectRA software indicating the interactions with different interfaces. The orange box is the security device interface, the yellow box is the sun-tracking system interface, the blue box is the spectrometer interface and the green box shows the pyranometer interface.

3 Principles of atmospheric retrieval

The primary objective of our measurements is to derive the concentration of target trace gases within the atmosphere by analysing observed solar absorption spectra. Each spectrum contains the absorption characteristics of the atmospheric constituents, enabling the extraction of total columns or vertical profiles of the absorbing target gases. FTS-Paris spectra (example in Fig. 2) represent the spectral radiance $L(\nu, z)$ entering the instrument after transmission through the atmosphere. The radiance can be described by the radiative transfer equation (García et al., 2021; Rodgers, 2000):

$$L(\nu, z) = L(\nu, 0)\, \tau(\nu, 0, z) + e' \quad (1)$$

https://doi.org/10.5194/essd-2026-762
Preprint. Discussion started: 6 November 2026
© Author(s) 2026. CC BY 4.0 License.



where $L(\nu, 0)$ is the incoming solar radiance at the top of the atmosphere, and $\tau(\nu, 0, z)$ is the atmospheric transmittance between the surface and altitude z. The term e' represents the contribution from atmospheric emission along the path, which depends mainly on the temperature. This contribution is negligible for ground-based solar absorption measurements, because the thermal emission from the atmosphere is extremely weak compared to the direct solar radiation.

The transmittance $\tau(\nu, 0, z)$ can be written as

$$\tau(\nu, 0, z) = \exp\left[-\int_0^z \sum_i k_i[\nu, T(z')] f_i[\nu, p(z'), T(z')] \rho_i(z') \mathrm{d}z'\right] \quad (2)$$

where $k_i[\nu, T(z')]$ is the line strength of species i at wavenumber ν, which depends on the temperature $T(z')$ through the population of the molecular energy levels, $f_i[\nu, p(z'), T(z')]$ describes the spectral line shape function that characterizes how the absorption is distributed around the line centre. The shape and width of this function depend on the local pressure and temperature at altitude z'. Finally, $\rho_i(z')$ is the number density of species i at altitude z'.

By integrating these physical quantities within a radiative transfer framework, the measured absorption spectrum can be quantitatively correlated with the vertical distribution of the atmospheric absorbers. Equation (2) forms the basis for the inversion procedure, where the forward model calculates a theoretical spectrum from atmospheric state parameters, which is then compared and fitted to the observed spectrum. In this retrieval procedure, the measured spectrum is represented as the simulation result with an additional error:

$$\boldsymbol{y} = \boldsymbol{F}(\boldsymbol{x}, \boldsymbol{n}) + \boldsymbol{\varepsilon}\,, \quad (3)$$

where $\boldsymbol{y}$ represents the measurement vector $L(\nu, z)$ and $\boldsymbol{F}(\boldsymbol{x}, \boldsymbol{n})$ denotes the simulated values from the forward model in Eqs. (1-2). The unknowns include a state vector $\boldsymbol{x}$ and a parameter vector $\boldsymbol{n}$, which describe the atmospheric state and the instrumental parameters, respectively. $\boldsymbol{\varepsilon}$ signifies the measurement error. The problem described by Eq. (3) is ill-posed, meaning that multiple atmospheric states $\boldsymbol{x}$ can result in nearly identical spectra $\boldsymbol{y}$. To address this, a cost function is used to constrain the calculation results:

$$\boldsymbol{C}(\boldsymbol{x}) = [\boldsymbol{y} - \boldsymbol{F}(\boldsymbol{x}, \boldsymbol{n})]^T \boldsymbol{S}_m^{-1} [\boldsymbol{y} - \boldsymbol{F}(\boldsymbol{x}, \boldsymbol{n})] + [\boldsymbol{x} - \boldsymbol{x}_a]^T \boldsymbol{S}_a^{-1} [\boldsymbol{x} - \boldsymbol{x}_a], \quad (4)$$

The cost function $\boldsymbol{C}(\boldsymbol{x})$ consists of two terms. The first term represents the difference between the measured spectrum $(\boldsymbol{y})$ and the simulated spectrum for a given atmospheric state $(\boldsymbol{x})$. $\boldsymbol{S}_m$ is the measurement covariance matrix of $\boldsymbol{y} - \boldsymbol{F}(\boldsymbol{x}, \boldsymbol{n})$. The second term is the regularization term, which constrains the atmospheric state $(\boldsymbol{x})$ towards the most likely state $(\boldsymbol{x}_a)$, also called the a priori profile, whereby the kind and strength of the constraint are defined by the a priori covariance matrix $(\boldsymbol{S}_a)$. The convergence is reached by numerically minimizing the cost function in Eq. (4). The $(i+1)^{\text{th}}$ iteration of the minimization procedure yields the approximated atmospheric state vector $\hat{\boldsymbol{x}}_{i+1}$:

$$\hat{\boldsymbol{x}}_{i+1} - \boldsymbol{x}_a = \boldsymbol{G}_i[\boldsymbol{y} - \boldsymbol{F}(\hat{\boldsymbol{x}}_i, \boldsymbol{n}) + \boldsymbol{K}_i(\hat{\boldsymbol{x}}_i - \boldsymbol{x}_a)], \quad (5)$$

where $\boldsymbol{x}_a$ is the a priori atmospheric state, $\hat{\boldsymbol{x}}_i$ is the retrieved atmospheric state vector at the i^{th} iteration, $\boldsymbol{K}_i = \boldsymbol{K}(\hat{\boldsymbol{x}}_i)$ is the Jacobian matrix evaluated at $\hat{\boldsymbol{x}}_i$, $\boldsymbol{K}_i$ describes the sensitivity of the simulated spectrum to changes in the state vector $\boldsymbol{x}$. $\boldsymbol{G}_i$ is the gain matrix which describes the sensitivity of the retrieved state to changes in the measurement vector $\boldsymbol{y}$. To characterize the relationship between the retrieved results and the actual atmospheric state due to the imperfect vertical profile resolution

https://doi.org/10.5194/essd-2026-762
Preprint. Discussion started: 6 November 2026
© Author(s) 2026. CC BY 4.0 License.

of the ground-based remote sensing FTIR instrument. This relationship is theoretically characterised by the averaging kernel (AVK) matrix $\boldsymbol{A}$, which is calculated by $\boldsymbol{A} = \boldsymbol{GK}$. It captures how the retrieval depends on changes in the atmospheric state:

$$\hat{\boldsymbol{x}} - \boldsymbol{x}_a = \boldsymbol{A}(\boldsymbol{x} - \boldsymbol{x}_a), \quad (6)$$

Each element of the AVK matrix $\boldsymbol{A}$ represents the sensitivity of the retrieved parameter in a specific atmospheric layer with respect to the true state vector in the different layers.

Furthermore, the retrieval error can be decomposed into smoothing error, model parameter error, and retrieval noise as:

$$\hat{\boldsymbol{x}} - x = (\boldsymbol{A} - \boldsymbol{I_n})(\boldsymbol{x} - \boldsymbol{x}_a) + \boldsymbol{GK}_n(\boldsymbol{n} - \hat{\boldsymbol{n}}) + \boldsymbol{G\varepsilon}, \quad (7)$$

where $(\boldsymbol{A} - \boldsymbol{I_n})(\boldsymbol{x} - \boldsymbol{x}_a)$ describes the smoothing error, $\boldsymbol{I_n}$ is the identity matrix, $\boldsymbol{K}_n = \frac{\partial F(x,n)}{\partial n}\Big|_{n=\hat{n}}$ represents the Jacobian matrix with respect to forward model parameters $\boldsymbol{n}$, such as temperature profiles, spectroscopic parameters and interfering species, $\hat{\boldsymbol{n}}$ denotes the corresponding parameter values adopted in the retrieval, $\boldsymbol{GK}_n(\boldsymbol{n} - \hat{\boldsymbol{n}})$ describes how uncertainties in these parameters propagate into the retrieved state, and the term $\boldsymbol{G\varepsilon}$ represents the retrieval noise (Rodgers, 2000).

In the NDACC-IRWG retrieval, two different retrieval methods are commonly used: the Optimal Estimation method (OEM) or the Tikhonov-Phillips regularization method (TP) (García et al., 2021; Yamanouchi et al., 2023). OEM is a Bayesian retrieval technique. It is based on the principle of combining measurements with prior knowledge to find the most probable atmospheric state. TP is a mathematical technique for solving ill-posed inverse problems by adding a regularization term to the cost function. In this work we have tested and used both methods.

3.1 Optimal Estimation method

The optimal estimation method (OEM) is based on Optimal Estimation Theory as developed by Rodgers (2000). The OEM approach is based on the solution of Eqs. (3-6) as outlined above. The optimal solution is given by:

$$\hat{\boldsymbol{x}}_{i+1} = \hat{\boldsymbol{x}}_i + (\boldsymbol{S}_a^{-1} + \boldsymbol{K}_i^T \boldsymbol{S}_\varepsilon^{-1} \boldsymbol{K}_i)^{-1}\left[\boldsymbol{K}_i^T \boldsymbol{S}_\varepsilon^{-1}\left(\boldsymbol{y} - \boldsymbol{F}(\hat{\boldsymbol{x}}_i)\right) - \boldsymbol{S}_a^{-1}(\hat{\boldsymbol{x}}_i - \boldsymbol{x}_a)\right], \quad (8)$$

where i represents the iteration number, $\boldsymbol{S}_\varepsilon$ is the observation covariance matrix, which accounts for the observational uncertainties and errors, which is given by:

$$\boldsymbol{S}_\varepsilon = \sigma^2 \cdot \boldsymbol{I}, \quad (9)$$

where $\boldsymbol{I}$ is the identity matrix, and σ represents standard deviation of noise in the residuals of the spectral fit. When the retrieval is completed by fitting the spectra within the selected micro-windows, the best estimate of the vertical profile of the target gas, $\hat{\boldsymbol{x}}$, is obtained.

https://doi.org/10.5194/essd-2026-762
Preprint. Discussion started: 6 November 2026
© Author(s) 2026. CC BY 4.0 License.



3.2 Tikhonov-Phillips regularization

The Tikhonov-Phillips regularization (Phillips, 1962; Tikhonov, 1963) is an alternative retrieval approach. Similar to OEM, it uses the forward model $\boldsymbol{F}$ to map the atmospheric state vector $\boldsymbol{x}$ into the measurement vector $\boldsymbol{y}$. Following Sussmann et al. (2011), the inversion is formulated as a regularised least-squares problem, :

$$\|\boldsymbol{F}(\boldsymbol{x}) - \boldsymbol{y}\|^2 + \|\boldsymbol{\Gamma}(\boldsymbol{x} - \boldsymbol{x}_a)\|^2, \quad (10)$$

where the first term represents the least squares between modelled and measured states, and the second term represents the regularization term, given by the Tikhonov matrix $\boldsymbol{\Gamma}$. This latter term is used to constrain the solution and thereby avoid oscillating profiles base on the a priori $\boldsymbol{x}_a$. For the nonlinear retrieval used here, the TP solution is obtained iteratively.

The regularization matrix $\boldsymbol{\Gamma}$ is a real matrix with m rows and m columns, with m being the vertical altitude grid of the site (Sussmann et al., 2011), in fact, it can be scaled with a tuning parameter α:

$$\boldsymbol{\Gamma} = \alpha \boldsymbol{L}_1^T \boldsymbol{L}_1 \in \boldsymbol{\mathcal{R}}^{m*m}. \quad (11)$$

Here we set m = 48 and $\boldsymbol{L}_1$ designates the discrete first derivative operator:

$$\boldsymbol{L}_1 = \begin{pmatrix} -1 & 1 & 0 & \cdots & 0 \\ 0 & -1 & 1 & \ddots & \vdots \\ \vdots & \ddots & \ddots & \ddots & 0 \\ 0 & \cdots & 0 & -1 & 1 \end{pmatrix} \in \boldsymbol{\mathcal{R}}^{(m-1)*m}, \quad (12)$$

Similar to Eq. (8), a TP iteration is given by:

$$\hat{\boldsymbol{x}}_{i+1} = \hat{\boldsymbol{x}}_i + (\boldsymbol{\Gamma} + \boldsymbol{K}_i^T \boldsymbol{S}_\varepsilon^{-1} \boldsymbol{K}_i)^{-1} \left[\boldsymbol{K}_i^T \boldsymbol{S}_\varepsilon^{-1} \left(\boldsymbol{y} - \boldsymbol{F}(\hat{\boldsymbol{x}}_i)\right) - \boldsymbol{\Gamma}(\hat{\boldsymbol{x}}_i - \boldsymbol{x}_a)\right]. \quad (13)$$

The TP method constrains $\boldsymbol{x}$ such that a constant profile is favoured for the difference $(\boldsymbol{x} - \boldsymbol{x}_a)$, indicating that a shifted a priori is the preferred solution. Evidently, the solution will depend on the choice of the regulation strength α. The process of determining α is detailed in section 4.2.3.

4 The nominal retrieval strategy

Spectra with insufficient signal quality (a signal-to-noise (SNR) below 50) are excluded from the retrieval. The SNR is calculated from predefined signal and noise intervals for each NDACC filter, see Appendix Table A1. The retrieval of the atmospheric spectrum to obtain the trace gas abundance needs many parameters. The nominal retrieval strategy includes the choice of these parameters and the selection of methods or tools used to optimise the quality and the accuracy of the retrieved results. Two retrieval codes are relevant and recommended in this context: SFIT4 (Pougatchev et al., 1995; Rinsland et al., 1998), and the PROFFIT9 code developed by Hase et al. (2004). Both have been used within the NDACC-IRWG network for long-term analyses and satellite validations (e.g., Buchholz et al., 2017; García et al., 2021; Kohlhepp et al., 2012; Vigouroux et al., 2018; Yamanouchi et al., 2021). An intercomparison of SFIT2 (the predecessor of SFIT4) with PROFFIT9 on O_3, HNO_3, HDO and N_2O has shown that differences between retrieved total columns derived from high-resolution ground-based solar

https://doi.org/10.5194/essd-2026-762
Preprint. Discussion started: 6 November 2026
© Author(s) 2026. CC BY 4.0 License.



FTIR spectra using either code is below 1% (Hase et al., 2004). The radiative transfer code is usually based on two separated models: the first model is the "forward" model followed by the "inversion" (second) model.

4.1 Forward model

The forward model calculates the solar absorption spectrum that is compared with the measured FTS-Paris spectrum during the retrieval. In Eqs. (1)-(3), the measured radiance is mainly controlled by the incoming solar radiance, the atmospheric transmittance along the optical path, and molecular absorption by the target and interfering species. For each target gas, the micro-windows (MW) listed in Table 2 are the selected wavenumber intervals following previous recommendations (García et al., 2021; Hannigan et al., 2022a; Harrison et al., 2010; Kohlhepp et al., 2012; Ortega et al., 2025; Sun et al., 2023; Sussmann et al., 2011; Té et al., 2016; Vigouroux et al., 2018; Yamanouchi et al., 2023; Zhu et al., 2024). These intervals contain absorption lines of the target species, but they can also include absorption from interfering gases that must be fitted simultaneously. The spectroscopic parameters define how the absorption is represented in the forward model. The line position fixes the centre of each transition, the line intensity controls its absorption strength, and the line shape parameters describe how the absorption is distributed around the line centre as pressure and temperature vary with altitude. In SFIT4 calculations, the absorption line shape is modelled using a standard Voigt line profile. HITRAN 2020 is used as the current spectroscopy where appropriate (Gordon et al., 2022; Hannigan and Mahieu, 2023), replacing the older HITRAN 2008 spectroscopy used in previous NDACC-IRWG retrievals (García et al., 2021; Rothman et al., 2009; Yamanouchi et al., 2023). Dedicated spectroscopy is retained for species for which it improves the retrieval: pseudo-lines are used for C_2H_6 (Franco et al., 2015; Harrison et al., 2010), while ATM2020 is used for CH_4 and H_2O (Chesnokova et al., 2020; Gordon et al., 2022; Ortega et al., 2019), as summarised in Table 2.

The a priori profiles are based on the updated WACCM6 model results covering the time period from 1980 to 2040 (Gettelman et al., 2019), referred to within NDACC-IRWG as IRWG7. Temperature and pressure profiles are taken from the National Centers for Environmental Prediction (NCEP) from the surface to 56 km and merged with IRWG7 above this altitude. These profiles affect both molecular number density and pressure- and temperature-dependent line shapes. Finally, instrumental parameters, including the spectral resolution and the instrument line shape (ILS), are included to make the simulated and measured spectra comparable. An ideal ILS is assumed in the Paris retrieval, and the impact of this assumption is evaluated in Sect. 4.3.2.

Table 2: Summary of the retrieval strategy for different species at the Paris NDACC-IRWG site

Target Gas	Micro-windows [cm^{-1}]	Interfering species	A Priori	Linelist	Column or Profile	Method
C_2H_6	[1] 2976.66-2977.059 [2] 2983.20-2983.500 [3] 2986.45-2986.850	H_2O, O_3, CH_3Cl, CH_4	IRWG7	Pseudo-line for C_2H_6[#1], HITRAN 2020 for the rest, except for O_3[#2]	Profile for C_2H_6, column for the rest	TP, α=100

https://doi.org/10.5194/essd-2026-762
Preprint. Discussion started: 6 November 2026
© Author(s) 2026. CC BY 4.0 License.



Open Access Earth System Science Data Discussions

HF	[1] 4038.81-4039.07	H_2O, HDO, CH_4	IRWG7	HITRAN 2020	Profile for HF, column for the rest	OEM
HCl	[1] 2727.73-2727.83 [2] 2775.70-2775.80 [3] 2925.80-2926.00	O_3, HDO O_3, HDO CH_4, NO_2	IRWG7	HITRAN 2020	Profile for HCl, column for the rest	OEM
N_2O	[1] 2481.30-2482.60 [2] 2526.40-2528.20 [3] 2537.85-2538.80 [4] 2540.10-2540.70	CH_4, CO_2 CH_4, CO_2 HDO	IRWG7	HITRAN 2020	Profile for N_2O, column for the rest	TP, α=1000
CO	[1] 2057.70-2058.00 [2] 2069.56-2069.76 [3] 2157.50-2159.15	O_3, CO_2, OCS O_3, CO_2, OCS O_3, CO_2, N_2O, H_2O	IRWG7	HITRAN 2020	Profile for CO, O_3 and N_2O, column for the rest	OEM
HCN	[1] 3268.05-3268.40 [2] 3287.10-3287.35 [3] 3299.40-3299.60	H_2O, C_2H_2 H_2O, CO_2, C_2H_2 H_2O, $H_2{}^{18}O$	IRWG7	HITRAN 2020	Profile for HCN, column for the rest	TP, α=200
CH_4	[1] 2613.70-2615.40 [2] 2835.50-2835.80 [3] 2903.60-2904.03 [4] 2921.00-2921.60	HDO, CO_2 HDO NO_2 HDO, NO_2, H_2O	IRWG7	ATM 2020	Profile for CH_4, column for the rest	TP, α=3000
H_2CO	[1] 2763.42-2764.17 [2] 2765.65-2766.01 [3] 2778.15-2779.10 [4] 2780.65-2782.00	HDO, CO_2, O_3, N_2O, CH_4	IRWG7	ATM 2020	Profile for H_2CO, HDO and CH_4, column for the rest	TP, α=1000
NO_2	[1] 2914.30-2914.85	CH_4, H_2O, O_3, C_2H_6, H_2CO, OCS, CH_3D, HDO	IRWG7	ATM 2020	Profile for NO_2 and CH_4, column for the rest	TP, α=100
OCS	[1] 2030.75-2031.06 [2] 2047.85-2048.24 [3] 2049.77-2050.18 [4] 2051.18-2051.48 [5] 2054.33-2054.67	CO_2, O_3 O_3, CO_2 O_3, H_2O, CO, $CO^{18}O$ O_3, H_2O O_3, H_2O $H_2{}^{18}O$	HIPPO (<14 km) and ACE-FTS (>14 km)	HITRAN 2012	Profile for OCS, CO and O_3, column for the rest	OEM

[#1] C_2H_6 spectroscopy taken from Franco et al. (2015)

[#2] O_3 Hitran2020 spectroscopy modified by Chelin personal communication

4.2 Inversion model

After the forward model has been defined, the inversion step estimates the atmospheric state vector $\boldsymbol{x}$ that best reproduces the measured spectrum. The simulated spectrum $\boldsymbol{F}(\boldsymbol{x}, \boldsymbol{n})$ is convoluted with the ILS and then compared with the measured spectrum

https://doi.org/10.5194/essd-2026-762
Preprint. Discussion started: 6 November 2026
© Author(s) 2026. CC BY 4.0 License.



according to Eq. (3). The inversion is a constrained estimate of the atmospheric state within the measurement and modelling uncertainties.

Following Rodgers (2000), the inversion is formulated as a constrained optimisation problem. The optimal estimate of $\boldsymbol{x}$ is obtained by minimizing the cost function Eq. (4) which balances two requirements: the simulated spectrum must fit the measurement, and the retrieved state must remain physically consistent with the a priori information $\boldsymbol{x_a}$.

In the Paris retrieval strategy, the inversion procedure is applied after defining the forward model inputs listed in Table 2. Water vapour is treated separately before the target gas retrievals, as described in Sect. 4.2.1, while the choice between OEM (see Sect. 4.2.2) and TP (see Sect. 4.2.3) constraints for retrieval named "in profile" for the target gases is discussed in Sect. 4.2.4. Retrieval "in column" corresponds to a scaling of the whole a priori profile.

4.2.1 Pre-retrieved H_2O profile

Water vapour is one of the most important interfering species for Paris retrievals. Its vertical distribution is highly variable and spatially inhomogeneous, especially in the troposphere and at humid sites of low-altitude. Model or meteorological profiles, such as IRWG7 or NCEP+IRWG7, are therefore not always expected to represent the local water vapour state at the time of each measurement with sufficient accuracy. To obtain an H_2O profile that is representative of the water vapour state at the time of the analysed spectrum, we perform a dedicated H_2O retrieval before the target gas retrieval. Here, we follow the FTIR water vapour strategy of Ortega et al. (2019), with the updates used in the present Paris SFIT4 setup. H_2O is retrieved with OEM method from 4 micro-windows in the 2600-2940 cm^{-1} region: 2611.40-2613.40, 2659.00-2661.00, 2819.00-2819.80, and 2929.80-2931.40 cm^{-1}, see Fig. A7. These windows include H_2O and HDO absorption lines and also contain the interfering species CH_4, CO_2, N_2O and HCl. H_2O, HDO and CH_4 are treated as profile retrieval using the OEM method while CO_2, N_2O and HCl are using column retrieval. In our implementation, the initial H_2O a priori profile is the NCEP+IRWG7 profile, temperature and pressure are taken from NCEP up to 56 km and merged with IRWG7 above this altitude. ATM 2020 spectroscopy is used for H_2O while the spectroscopy of the other gases is taken from HITRAN 2020. The product of this dedicated H_2O profile retrieval is what we refer to as the pre-retrieved H_2O profile. This is then used as the H_2O a priori in the target gas retrieval whenever H_2O is included as an interfering species.

To evaluate whether this pre-retrieved H_2O profile improves the representation of H_2O absorption in the Paris spectra, we performed a controlled sensitivity test using one of the NDACC11 spectra measured at Paris on 6 August 2020. The same H_2O retrieval setup was applied three times, using IRWG7, NCEP+IRWG7, and the pre-retrieved H_2O profile as the a priori profile, respectively. A scaling retrieval was used deliberately for this comparison, where the vertical shape of each a priori profile is kept fixed. This test examines whether the fixed shape of each a priori can reproduce the measured H_2O amount. Among the three tests, the pre-retrieved H_2O profile gives the lowest root-mean-square of the spectral fitting residuals (FITRMS), indicating that the pre-retrieved profile provides a more suitable spectral representation of H_2O absorption than the two other profiles for this particular spectrum. This result is consistent with Ortega et al. (2019), who showed that retrieval performance

https://doi.org/10.5194/essd-2026-762
Preprint. Discussion started: 6 November 2026
© Author(s) 2026. CC BY 4.0 License.



improves when site- and time-specific H_2O information is used. In the routine retrieval processing, the H_2O profile retrieved from each spectrum is therefore used as the H_2O a priori profile for the retrieval of other species from the same spectrum whenever H_2O is an interfering species, replacing the default IRWG7 profile.

Table 3: H_2O scaling retrieval results using three different a priori profiles for the NDACC11 spectrum measured on 2020-08-06 at 11: 52:15 UTC

	FITRMS	χ^2	Total column [molecules cm^{-2}]
H_2O IRWG7	0.388	1.919	7.22319E+22
H_2O NCEP+IRWG7	0.383	1.872	7.21081E+22
H_2O pre-retrieved	0.323	1.339	7.58102E+22

4.2.2 Implementation of the OEM method at Paris

At the Paris site, the vertical profile is computed on a 48-layer grid extending from 60 m to 106 km altitude, based on the IRWG7 model. Temperature and pressure profiles from the NCEP were from the surface up to 56 km and then merged with IRWG7 above 56 km until the top of the layer grid. The constraint $\boldsymbol{S_a}$ matrix is determined using diagonal elements corresponding to the ratio of the standard deviation to the mean volume mixing ratio (VMR) of the IRWG7 model at each layer.

The OEM iteratively refines the target gas VMR profile by minimizing the discrepancies between measured and simulated spectra while balancing measurement information with a priori constraints. The method accounts for retrieval uncertainties and incorporates physical constraints through prior knowledge. However, the quality of OEM strongly depends on the choice of a priori information and associated constraints.

Taking CO as an example, Fig. 4 presents a representative fit between measured and simulated spectra in the three micro-windows that were used. The quality of the fit can be seen from the residuals (difference between simulated and measured spectra) which are well within the measured noise. HITRAN 2020 spectroscopy was used for CO and all interfering species, except for H_2O. A priori profiles of all species were taken from the IRWG7, while the H_2O profiles were pre-retrieved, see Sect. 4.2.1. During the retrieval tests, the original diagonal constraints of $\boldsymbol{S_a}$ derived from IRWG7 were found to provide excessive flexibility in the upper atmosphere, particularly above 30 km where the standard deviation of the IRWG7 CO profiles is about 250% higher than in the troposphere. Under these conditions, the inversion may produce unrealistically large VMR values and oscillatory structures in the retrieved upper-atmospheric profile, despite having negligible impact on the retrieved total column. Because CO is a tropospheric gas, the diagonal elements of $\boldsymbol{S_a}$ above 30 km were artificially reduced by a factor of 10 to strengthen the constraint in this altitude range and improve the retrieval sensitivity in the troposphere. This adjustment stabilised the retrieved CO vertical profile while the retrieved total column remained nearly unchanged. After applying the

https://doi.org/10.5194/essd-2026-762
Preprint. Discussion started: 6 November 2026
© Author(s) 2026. CC BY 4.0 License.



stronger constraint, the degrees of freedom (DOF), defined as the trace of the averaging kernel matrix (see Rodgers (2000) decreased from approximately 3 to 2. The final retrieved CO profile is presented in Fig. 5.

The corresponding OEM fitted spectra and vertical profile figures for other gases (HF, HCl and OCS) using the same approach are provided in Appendix A1.

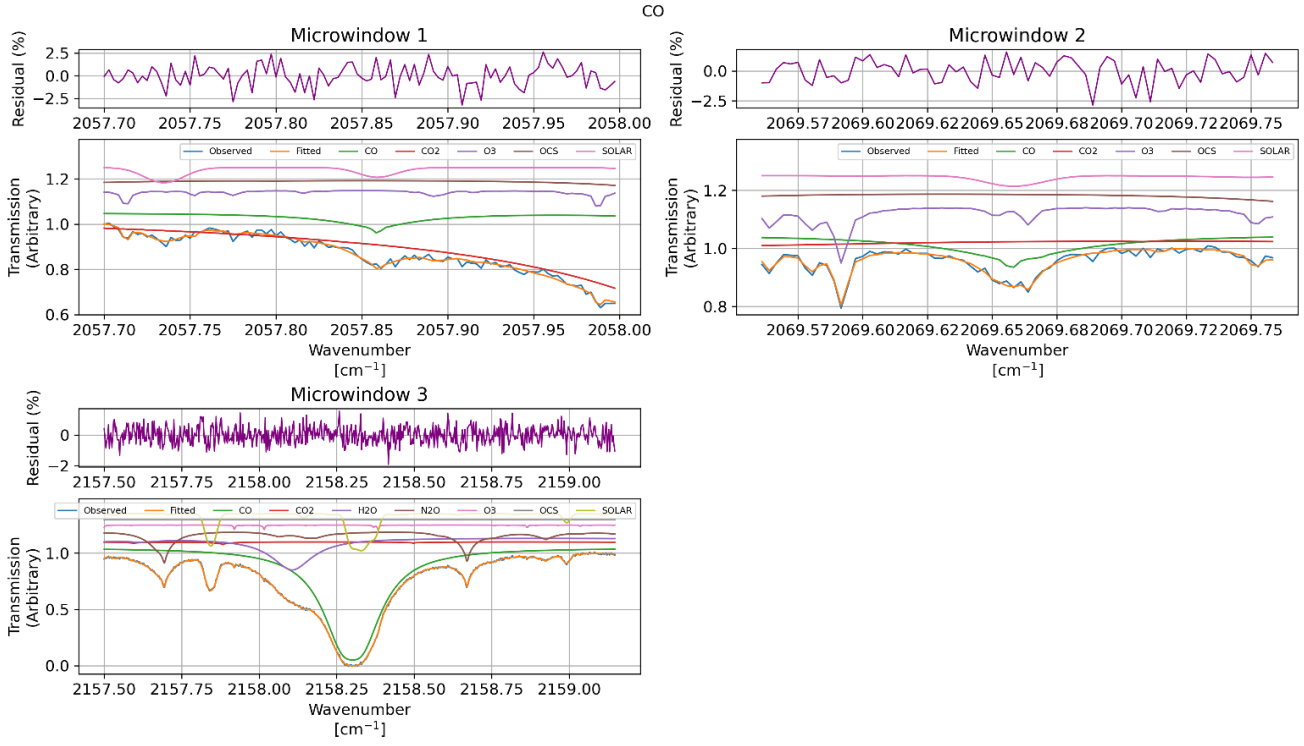


Figure 4: Measured (blue) and fitted (orange) spectrum in the 3 CO MWs recorded on 6 of August 2020 at Paris. The residuals are shown in purple.

https://doi.org/10.5194/essd-2026-762
Preprint. Discussion started: 6 November 2026
© Author(s) 2026. CC BY 4.0 License.

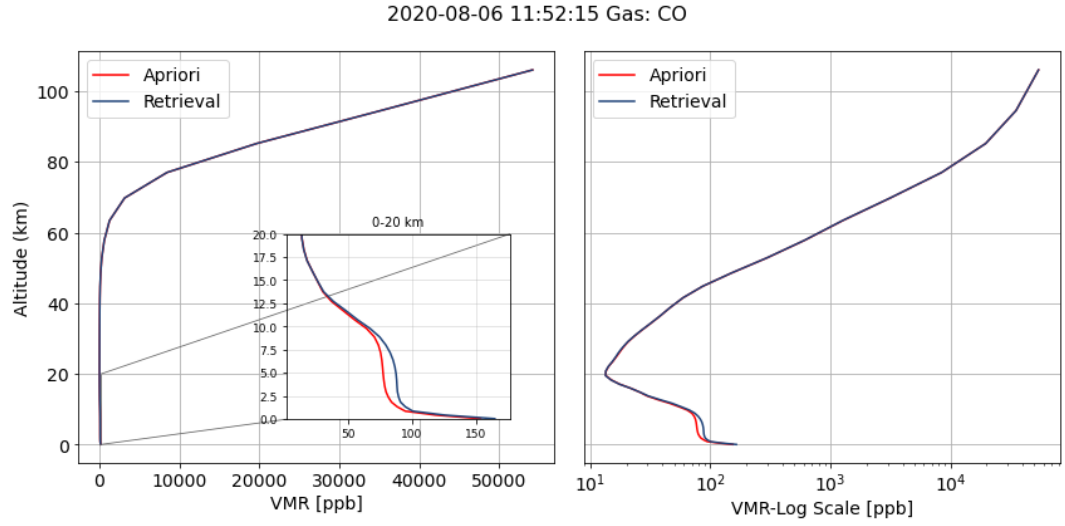


Figure 5: A priori (red) and retrieved (blue) CO profiles of the spectrum shown above. Left: volume mixing ratio in linear scale. Right: volume mixing ratio in logarithmic scale.

365

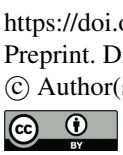
4.2.3 Implementation of the TP method at Paris

Following the theoretical framework presented in Sect. 3.2, we now detail the procedure for selecting the TP regularization strength α. Unlike the OEM method, which primarily relies on the a priori covariance $\boldsymbol{S_a}$ matrix to constrain the solution, the TP method restricts the retrieval by tuning the parameter α. To determine the optimal α, we evaluate its impact on several
370 retrieval output metrics: the DOF, the retrieved total column, FITRMS, and χ^2 (which quantifies the uncertainty-weighted difference between observed and simulated spectra), and the total error (representing the combination of measurement and smoothing errors).

Using CH_4 as an example (see Fig. 6), we perform a systematic sensitivity test across a wide range of α values. OEM retrieval provides an approximate DOF of 2.5 for CH_4 in Paris. The optimal α is determined by identifying the point where the DOF,
375 total column, FITRMS, and χ^2 stabilize, while simultaneously minimizing the total error.

As shown in Fig.6b, at lower α values (e.g., $\alpha < 1000$), the retrieval is under-constrained. In this range, the measurement error $\boldsymbol{\varepsilon}$ dominates and the total column exhibits a high sensitivity to minor α variations. Correspondingly, the retrieved VMR profiles display obvious oscillations (Fig. 6a). The left panel of Fig. 6 illustrates this behaviour directly: for very small α, the retrieved CH_4 profile departs strongly from a smooth vertical structure and shows alternating positive and negative deviations
380 with altitude. These oscillations are not interpreted as atmospheric features, but as a symptom of an insufficiently constrained retrieval. As α increases, the vertical structure becomes progressively smoother, while the main profile shape remains consistent. For $\alpha \geq 3000$, further increases in α lead only to small changes in the retrieved profile. This indicates that the solution has become stable with respect to the regularization strength. Conversely, high α values over-constrain the retrieval,

https://doi.org/10.5194/essd-2026-762
Preprint. Discussion started: 6 November 2026
© Author(s) 2026. CC BY 4.0 License.



resulting in an increase in the smoothing error, and a profile shape that changes only weakly relative to the a priori, approaching a scaling-like retrieval.

At $\alpha = 3000$, the retrieval output metrics enter a plateau. The unconstrained profile oscillations are limited, yielding a smooth VMR profile without overly degrading the measurement information. The total column, FITRMS and χ^2 stabilize. Consistently, the DOF decreases from the unconstrained state and stabilizes at approximately 2.5, which is similar than that obtained from an OEM retrieval.

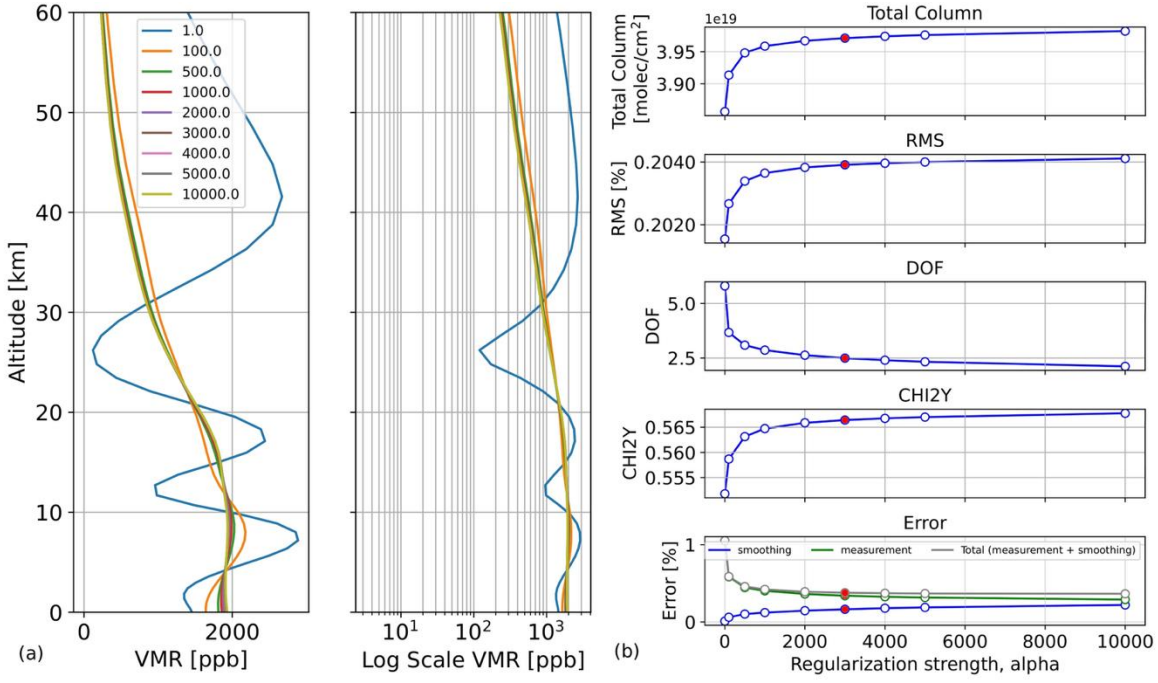


Figure 6: Sensitivity of CH_4 retrievals using Tikhonov-Phillips regularization strength α at Paris. Panel (a) shows the retrieved CH_4 VMR profiles for different α values, while panel (b) presents the corresponding retrieval diagnostics, including total column, FITRMS, χ^2 (or CHI2Y), and total error. The selected value a = 3000 is coloured as red dots.

Figure 7 represents spectral fits for CH_4 across four selected micro-windows using the TP optimised configuration. The spectroscopy and a priori profiles employed here follow the same configuration as the CO retrievals, with the exception that the CH_4 spectroscopy has been taken from ATM2020. In addition to the spectral fits, an example of the retrieved CH_4 vertical profile is shown in Fig. 8. The retrieved profile generally follows the vertical structure of the a priori profile, but shows moderate enhancements in the lower and middle troposphere. The largest difference appears below 20 km, where most of the column sensitivity is expected from ground-based absorption measurements. Above the stratosphere (60 km), the retrieved and a priori profiles remain close, indicating that the retrieval is mainly constrained by the a priori where the measurement sensitivity is limited. The same profile is also shown on a logarithmic VMR scale to highlight the agreement over the full

https://doi.org/10.5194/essd-2026-762
Preprint. Discussion started: 6 November 2026
© Author(s) 2026. CC BY 4.0 License.



Open Access Earth System Science Data Discussions

altitude range. The corresponding TP fitted spectra and vertical profile figures for the other gases (N_2O, C_2H_6, HCN, H_2CO and NO_2) retrieved using this approach are provided in Appendix A2.

The TP method is particularly useful for unstable inverse problems or when prior information is limited (Steck, 2002), as it enforces smoothness and other constraints on the solution. It is flexible, capable of operating without strong initial guesses, and can be implemented efficiently. More details can be found elsewhere (Phillips, 1962; Tikhonov, 1963; Sussmann et al., 2011; Vigouroux et al., 2018).

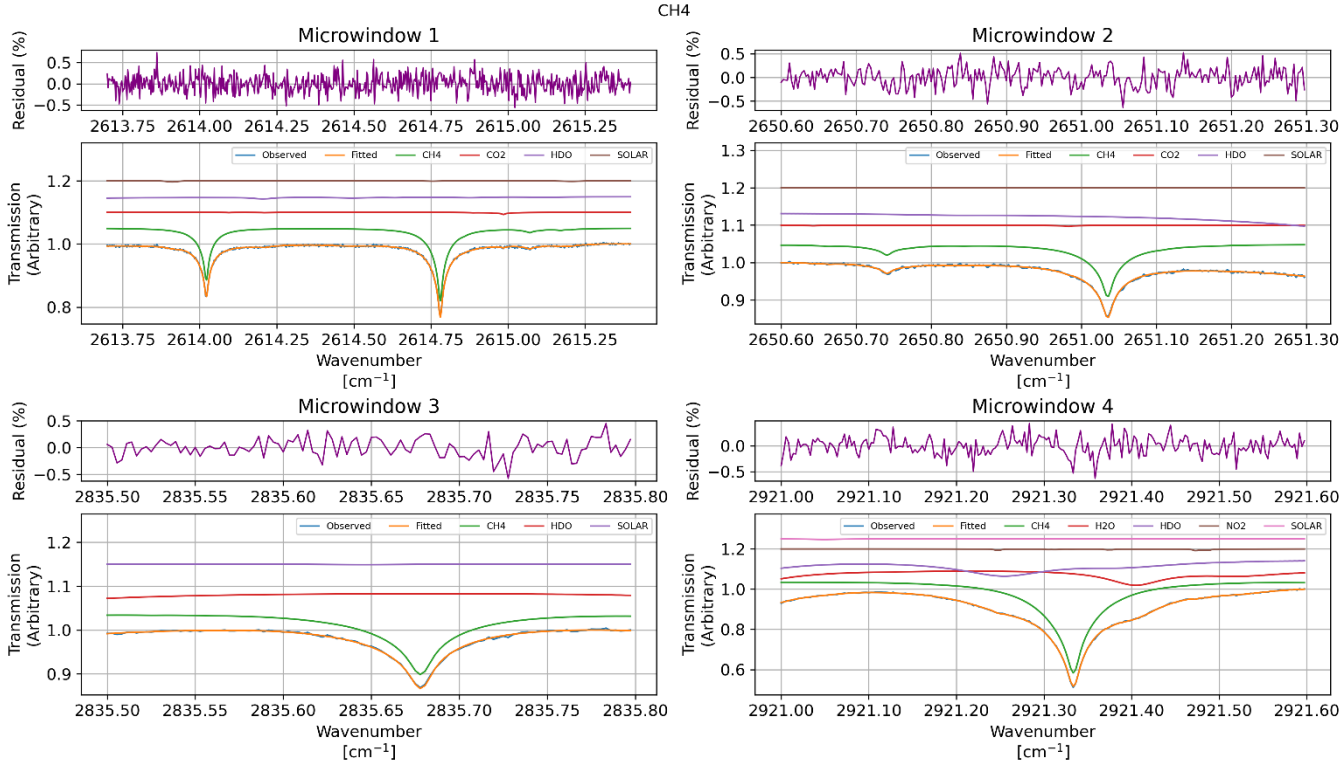


Figure 7: Measured (blue) and fitted (orange) spectrum in the 4 CH_4 MW's recorded on 6 of August 2020 at Paris. The residuals are shown in purple.

https://doi.org/10.5194/essd-2026-762
Preprint. Discussion started: 6 November 2026
© Author(s) 2026. CC BY 4.0 License.

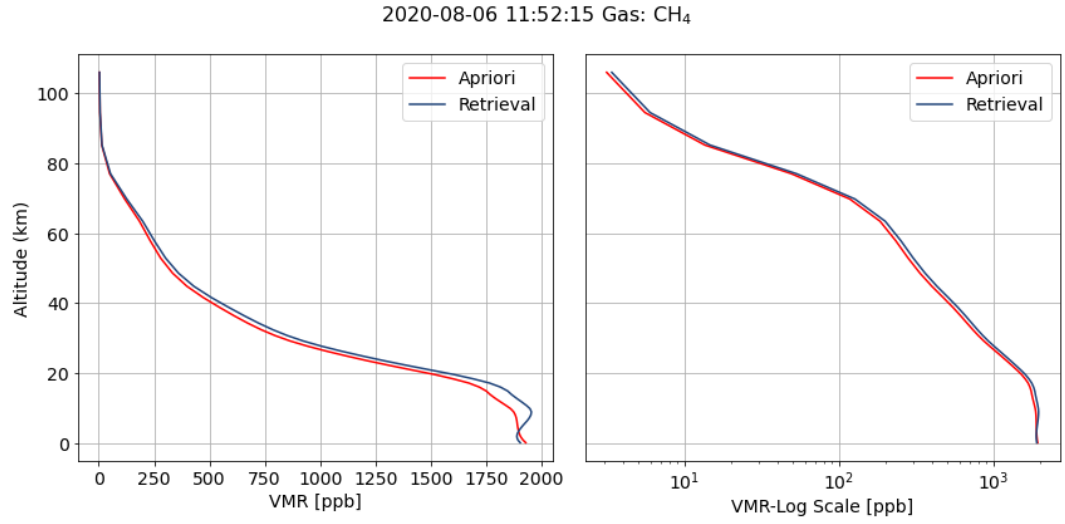


Figure 8: A priori (red) and retrieved (blue) CH_4 profiles of the spectrum shown above. Left: volume mixing ratio in linear scale. Right: volume mixing ratio in logarithmic scale.

4.2.4 How to choose between OEM and TP

Following the theoretical descriptions and examples of the OEM and TP methods, we systematically evaluate both strategies. For each target gas, the optimal constraints are determined following the examples detailed in Sect.4.2.2 and 4.2.3, respectively. The choice between OEM and TP is driven by evaluating the FITRMS, the DOF, retrieved total column variations, and retrieved vertical profiles. The AVKs are provided in Fig. A19 only to document the vertical sensitivity of the final nominal retrievals, not as the basis for choosing between OEM and TP. During these tests, all other parameters (such as the spectroscopy listed in Table 2 and the a priori profiles) have been fixed in order to isolate the impact of the inversion method alone. In certain specific cases, one method (OEM or TP) is more suitable than the other. However, in most cases, the two methods yield fairly similar results. Choosing one method over the other is not straightforward and sometimes depends on the user's sensitivity and interpretation of the results obtained.

For C_2H_6, both OEM and TP yield similar FITRMS, and DOFs (~1.0), see Table 4. However, the OEM vertical profile occasionally exhibited a subtle "S"-shaped feature in the lower atmospheric layers (Fig. 9, sky-blue dashed curve), a behaviour not observed at most NDACC-IRWG sites. To avoid this possible "S"-shaped feature over the long-term time series, TP emerges as the preferred method for C_2H_6. Conversely, OEM is preferred for CO to limit overfitting at high altitude (> 30 km). As shown in Table 4, the DOF for CO using OEM indicates two independent pieces of information while TP gives three independent pieces of information. The last independent half or point corresponds to an altitude above the stratosphere (~60 km), with a negligible air density. The resulting DOF from OEM: are more consistent with previous studies, where CO DOF retrieved from FTS instruments are typically below 3, for example, CO is 2.0±0.2 (1σ) at St Denis and 2.3±0.2 (1σ) at Maïdo

https://doi.org/10.5194/essd-2026-762
Preprint. Discussion started: 6 November 2026
© Author(s) 2026. CC BY 4.0 License.



(Zhou et al., 2018), 2.5 ±0.3 at Eureka (Viatte et al., 2014), 2.2 at Jungfraujoch and 2.7 at Wollongong (Té et al., 2016). For this reason, OEM has been selected for CO at the Paris site.

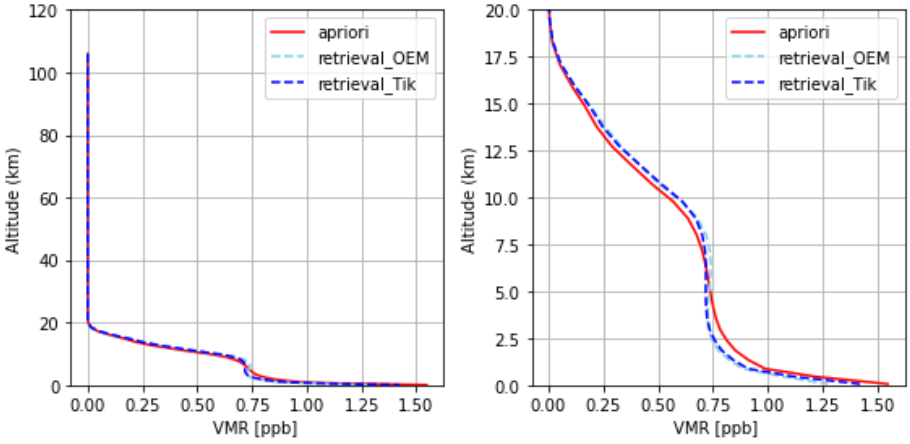


Figure 9: Vertical profile of ethane using different inversion methods: OEM (sky-blue), TP100 (blue), result from FTS-Paris spectrum 2020-08-06 11:52:15 UTC. Left: vertical profiles of ethane from 0.06 to 106 km; right: vertical profiles of ethane from 0 to 20km.

Gases with weak absorption signatures (absorptance of 1-2%, see Figs A13 and A17), such as HCN and NO_2, are highly sensitive to retrieval noise. For these species, OEM and TP yield similar FITRMS, while there are sizable differences in the retrieved total column of -7% and -27% for HCN and NO_2, respectively. The retrieved DOF for HCN are comparable between two methods, whereas NO_2 shows DOF lower than 1 (0.611) when using OEM, as shown in Table 4. Additionally, applying OEM resulted in DOF consistently below 1 for over 30% of the spectra. TP is better suited for these gases at Paris, providing more stable results than the OEM method. Moreover, for NO_2, the TP method is also consistent with the retrieval strategy of Vigouroux et al. (2018).

HF, HCl and OCS have peak sensitivity in the upper troposphere and stratosphere. We find that the OEM method performs better than TP in these cases. OEM also provides greater flexibility in representing the vertical distribution in the stratosphere without imposing additional smoothing on the profile, while TP smooths the profile by reducing stratospheric sensitivity and redistributing retrieval sensitivity toward troposphere. For this reason, we prefer to use OEM method for both HF and HCl. Specifically for OCS, OEM yields a higher DOF (~2.1) compared to TP (~1.5) and no significant differences can be found in the RMS or in the total columns, capturing vertical gradients more effectively and ensuring consistency with the approach of Hannigan et al. (2022a).

For gases such as N_2O, CH_4, and H_2CO, both OEM and TP produced comparable results, yielding similar RMS, DOF, and total columns (differences below 3%), as presented in Table 4. To maintain consistency with the harmonization with the

https://doi.org/10.5194/essd-2026-762
Preprint. Discussion started: 6 November 2026
© Author(s) 2026. CC BY 4.0 License.



standardised NDACC-IRWG retrieval strategy (Angelbratt et al., 2011a; Sussmann et al., 2011; Vigouroux et al., 2018), the TP method was applied for these gases, since no significant differences were found between the TP and OEM methods at Paris.

In summary, OEM and TP methods do not provide significantly different total columns, with differences below 3% except for HCN (7%) and NO_2 (27%). For these very weak absorption line species (less than 1%), another possibility to retrieve their abundance is scaling the entire a priori vertical profile, because the information contained in the spectrum may be limited. However, in this study, we aim to extract as much information as possible about the vertical distribution of these species, even at low absorption levels. The TP method is a good alternative. By individually assessing profile stability, we established a customised nominal retrieval strategy for each species observed by the Paris site. The final adopted strategies and corresponding spectroscopy databases are summarised in Table 2. The spectral fitting results, corresponding a priori and retrieved vertical profiles for all gases, except CO and CH_4, using nominal retrieval strategies are illustrated in Appendix A.

Table 4: Comparison of OEM and TP methods applied to different trace gases, spectra are NDACC11 recorded at 2020-08-06 11:52:15, NDACC01 same day at 11:57:25 and NDACC02 same day at 12:02:36

Gas	Spectra	Method	RMS [%]	DOF [-]	Total Column [molecules cm^{-2}]	Relative difference [%]
C_2H_6	NDACC11	OEM	0.447	1.067	1.383E+16	1.08
		TP100*	0.444	1.137	1.398E+16	
HF	NDACC01	OEM	0.348	1.696	1.584E+15	0.13
		TP100	0.343	1.830	1.586E+15	
HCl	NDACC11	OEM	0.163	1.757	3.547E+15	1.49
		TP100	0.163	2.116	3.600E+15	
N_2O	NDACC11	OEM	0.318	2.984	6.775E+18	0.04
		TP1000	0.319	3.087	6.778E+18	
CO	NDACC11	OEM	0.867	2.009	1.663E+18	-0.84
		TP100	0.866	3.023	1.649E+18	
HCN	NDACC02	OEM	0.380	1.366	5.478E+15	-6.83
		TP200	0.379	1.464	5.104E+15	
CH_4	NDACC11	OEM	0.204	2.625	3.958E+19	0.33
		TP3000	0.204	2.494	3.971E+19	
H_2CO	NDACC11	OEM	0.205	0.987	1.735E+16	-1.56
		TP1000	0.204	1.008	1.708E+16	
NO_2	NDACC11	OEM	0.157	0.611	1.165E+16	-26.73
		TP100	0.155	1.164	8.536E+15	
OCS	NDACC11	OEM	1.288	2.075	8.996E+15	2.63

https://doi.org/10.5194/essd-2026-762
Preprint. Discussion started: 6 November 2026
© Author(s) 2026. CC BY 4.0 License.



TP500	1.289	1.457	9.233E+15

* TP100, 100 is the α constrain

475

4.3 Retrieved data quality control

The retrieval strategy described above has been adopted as nominal setup for Paris and should be usable and reproducible for other sites. This section evaluates the main uncertainty sources and processing checks. The quality chain includes (i) random, systematic, and smoothing error characterization, (ii) the sensitivity of the retrievals to the instrument line shape, (iii) a
480 comparison between SFIT4 and the previous PROFFIT9 processing, and (iv) post-processing filters applied to remove low quality or outlying retrievals.

4.3.1 Error characterization

Retrieval errors have been characterised following the framework of Rodgers (2000). As shown in Eq. (7), the error can be
485 decomposed into three components: the retrieval noise, the smoothing error and the error in the parameters of the forward model. Tables 7 and 8 list the calculated random and systematic uncertainties, respectively. The atmospheric temperature profiles have an uncertainty of about 2 K for the vertical range from the surface to 30 km, and 6 K above. The total temperature uncertainty was assumed to be equally divided between random and systematic components. In addition, as shown in Table 5, spectroscopic uncertainties from HITRAN 2020 (Gordon et al., 2022) were considered, including the uncertainties in line
490 intensity, the temperature dependence of the line width (which affects the temperature sensitivity of absorption feature and is different from temperature profiles uncertainty) and the air-broadening of the line width (which influences the line shape). Table 6 summarizes the partitioning of the random and systematic components for each parameter used in SFIT4. All these error inputs were specified for the SFIT4 retrieval, which provides the corresponding output error components. Tables 7 and 8 present the random and the smoothing errors and the systematic errors obtained from representative spectra recorded on
495 August 6, 2020. In SFIT4, the total random error primarily consists of contributions from retrieval noise, retrieval parameters, interfering species and temperature profiles, while the systematic error mainly includes uncertainties in line intensity, temperature dependence and air-broadening of the line width and systematic temperature profile errors. The smoothing error, see Equation (7), is treated separately from the random and systematic error components in the SFIT4 calculation.

500 **Table 5: Input uncertainty from the spectroscopy database and temperature profile that used by SFIT4 error calculation.**

Gas	Temperature	Line intensity	Temperature dependence of line width	Air-broadening of line width
C_2H_6		4%	4%	4%
HF	2-6K	2%	10%	2%
HCl		2%	10%	5%

https://doi.org/10.5194/essd-2026-762
Preprint. Discussion started: 6 November 2026
© Author(s) 2026. CC BY 4.0 License.

N_2O	2%	5%	10%
CO	2%	5%	10%
HCN	10%	5%	10%
CH_4	3%	10%	5%
H_2CO	10%	10%	10%
NO_2	5%	10%	20%
OCS	2%	5%	5%

Table 6: Partitioning of the uncertainties between random and systematic contribution.

Uncertainty	Random/Systematic
Retrieval noise	100/0
Retrieval parameters	100/0
Interfering species	100/0
Temperature profile	50/50
Line intensity	0/100
Temperature dependence of line width	0/100
Air-broadening of line width	0/100

Most trace gases exhibit total random errors below 4% (see Table 7), except OCS, NO_2, and HCN, which show only weak absorption signals. Weak absorption lines provide smaller spectral sensitivities, i.e. smaller elements in the Jacobian matrix $\boldsymbol{K}_i$, and therefore less measurement information to constrain the retrieved state. As a result, spectral residuals and retrieval noise are more strongly propagated into the retrieved profile through the retrieval noise term $\boldsymbol{G\varepsilon}$ in Eq. (7), leading to larger retrieval noise. NO_2, in particular, shows a high total random error of 22.7%, driven primarily by its retrieval noise of 21.2%. Regarding total systematic uncertainties (Table 8), most species have errors below 6%, with the exceptions of C_2H_6, NO_2, H_2CO, and HCN, which are primarily affected by spectroscopic uncertainties concerning the line intensity and the air-broadening parameter. The smoothing errors (Table 7) for NDACC-Paris species are generally below 4%, except for NO_2, which exhibits a much higher value of 45%. This elevated smoothing error arises because NO_2 has the weakest spectral absorption among all gases measured by FTS-Paris and utilizes only one micro-window. Since this micro-window primarily captures stratospheric information while failing to resolve tropospheric NO_2, the retrieval cannot construct an effective retrieved vertical profile, resulting in a large smoothing error for NO_2 (see Eq. (7)).

Tables 5-8 summarize representative retrieval performance for the Paris setup. These examples show that most routine retrievals meet the expected NDACC-IRWG standard, while also identifying the species for which weak absorption or spectroscopy uncertainties dominate the error budget.

Table 7: Random error output from the measurement examples.

Gas	Retrieval noise (%)	Retrieval parameters (%)	Interfering species (%)	Temperature profile (%)	Total random error (%)	Smoothing error (%)
C_2H_6	0.34	0.34	0.34	0.34	0.34	0.52
HF	1.85	0.49	0.14	0.84	2.09	1.50

https://doi.org/10.5194/essd-2026-762
Preprint. Discussion started: 6 November 2026
© Author(s) 2026. CC BY 4.0 License.



Open Access Earth System Science Data Discussions

HCl	3.03	1.36	0.65	0.38	3.41	3.62
N_2O	0.16	0.01	0.01	0.04	0.17	0.04
CO	0.34	0.24	0.02	1.03	1.11	0.35
HCN	10.68	3.78	3.40	2.91	12.18	0.12
CH_4	0.34	0.03	0.01	0.55	0.65	0.17
H_2CO	2.69	0.07	2.76	0.78	3.93	1.01
NO_2	21.15	2.95	7.37	1.82	22.67	44.65
OCS	4.99	1.40	0.78	1.16	5.13	0.34

Table 8: Systematic error output from the measurement examples.

Gas	Line intensity (%)	Temperature dependence of line width (%)	Air-broadening of line width (%)	Temperature profile (%)	Total systematic error (%)
C_2H_6	8.16	0.66	7.71	0.26	11.25
HF	1.96	0.12	0.14	1.59	2.53
HCl	1.96	0.30	0.90	0.61	2.26
N_2O	5.00	0.27	2.78	0.06	5.73
CO	1.90	0.14	2.17	0.86	3.01
HCN	10.40	0.61	4.79	1.83	11.73
CH_4	3.01	0.01	1.65	0.52	3.47
H_2CO	10.00	0.28	8.02	0.69	12.84
NO_2	5.10	0.28	5.31	3.23	8.04
OCS	1.90	0.01	2.03	1.07	2.98

4.3.2 Impact of the instrument line shape on the gas retrieval

As introduced in Section 4.1, the ILS must be considered in the forward model. Since the Paris data were retrieved by assuming the line shape to be that of an ideal instrument, this section aims at evaluating the impact of this approximation by comparing the retrieval results using a realistic ILS with the results obtained from the ideal ILS.

Hase et al. (1999) have developed the LINEFIT software that can characterize the instrument line shape based on the measurement of a cell with a known quantity of HBr gas. LINEFIT takes into account the Field Of View (FOV), the spectral resolution, and the Signal to Noise Ratio (SNR) of the gas cell spectrum to determine the ILS of the instrument corresponding to the actual optical alignment. For an ideal instrument, the instrument line shape is given by a sinc function, which is determined as the Fourier transform of the boxcar apodization function (Bell, 1972). The real ILS is characterized by two parameters: modulation efficiency (ME) which is characterizing how the modulation intensity is maintained as a function of the Optical Path Difference (OPD), and phase error (PE) which is capturing the deviation of the measured interferogram phase from the ideal zero phase. The ideal ILS is considered to have ME and PE values of 1 and 0 as a function of the OPD, respectively.

https://doi.org/10.5194/essd-2026-762
Preprint. Discussion started: 6 November 2026
© Author(s) 2026. CC BY 4.0 License.

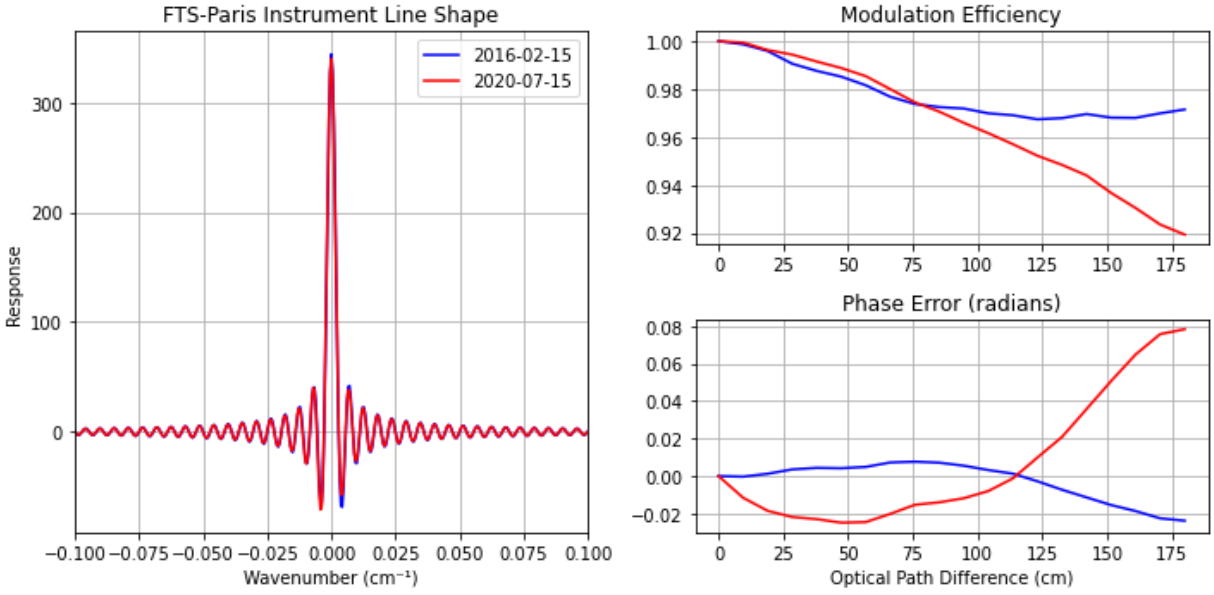


Figure 10: Two examples of FTS-Paris instrument line shape measurements from 2016-02-15 (blue) and 2020-07-15 (red): (left) instrument line shape, (top, right) modulation efficiency, and (bottom, right) phase error of the IFS125HR FTIR in Paris, retrieved from the HBr cell #80 with a maximal optical path difference of 180 cm.

Starting from 2016, ILS measurements of FTS-Paris spectrometer have been performed using the HBr cell #80 every 6 months. Examples of such measurements are shown in Fig. 10, with the blue curves corresponding to an ILS close to the ideal case (max. 3% deviation of ME along the OPD), and the red curves indicating the most extreme case of all ILSs measured ever since, with a maximum deviation of the ME up to 8%. The deviation above 5% necessitated a realignment of the instrument in order to fulfil the requirements of the TCCON network for a maximal OPD of 45 cm.

We used spectra recorded on August 6, 2020 and the most extreme ILS from July 15, 2020 for the study of the ILS sensitivity. Despite the degraded ME (8%), the comparison with results using the ideal ILS (see Table 9) shows that the total columns of all gases differ by less than 1%. Other ILS measurements at Paris have revealed smaller deviations from the ideal case. We can thus assume that the impact on the total columns is smaller in these cases and conclude that using an ideal ILS introduces a bias of less than 1%. This finding is consistent with a previous study of Whaley (2014), who reported a minimal impact of the ILS on total columns amounts. For the time being, we use an ideal ILS for the retrieval of FTS-Paris solar spectra in nominal configuration.

Table 9: Impact of using a measured ILS instead of an ideal ILS on retrieval results, spectra from 2020-08-06 at 11: 52:15, 11:57:25 and 12:02:36 UTC.

Gas	Ideal ILS	Real ILS	Difference *

https://doi.org/10.5194/essd-2026-762
Preprint. Discussion started: 6 November 2026
© Author(s) 2026. CC BY 4.0 License.



	Total column (molecules cm^{-2})	RMS (%)	Total column (molecules cm^{-2})	RMS (%)	(%)
CO	1.663E+18	0.867	1.669E+18	0.875	+0.4%
HCl	3.547E+15	0.163	3.542E+15	0.163	-0.1%
HCN	5.478E+15	0.380	5.454E+15	0.380	-0.4%
N_2O	6.778E+18	0.319	6.732E+18	0.314	-0.7%
C_2H_6	1.398E+16	0.444	1.412E+16	0.443	+1.0%
HF	1.584E+15	0.348	1.582E+15	0.346	-0.1%
CH_4	3.979E+19	0.205	3.961E+19	0.202	-0.5%

*Relative total column difference = (Real ILS – Ideal ILS)/Ideal ILS*100

4.3.3 Comparison of PROFFIT9 vs SFIT4 retrieval results

Previously published data retrievals from FTS-Paris were performed using the PROFFIT9 code for gases including CO, C_2H_6 and H_2CO. Té et al. (2016) retrieved CO relying on the HITRAN 2008 spectroscopic database (Rothman et al., 2009), while the retrieval of C_2H_6 used pseudo-lines provided by G. C. Toon (Harrison et al., 2010). The H_2CO retrievals followed the harmonized retrieval strategy from Vigouroux et al. (2018), based on the ATM 2016 database. A priori profiles for these gases were derived from the WACCM version 6 climatology spanning 1980–2020 (Marsh et al., 2013). Similar to the nominal configuration introduced in Section 4.1, the daily meteorological parameters, including temperature and pressure profiles were provided by NCEP (0-56 km) merged with WACCM6 (higher than 56 km). CO and C_2H_6 were retrieved using the OEM technique, while H_2CO was retrieved using scaling method provided by PROFFIT9.

So far, only a small number of groups have employed both PROFFIT9 and SFIT4 retrieval codes, and no quantitative comparison between PROFFIT9 and SFIT4 has been published. Hase et al. (2004) compared PROFFIT9 and SFIT2. We therefore compare the two retrieval software packages and the different database updates in order to reveal potential differences and their implications. The main differences between the two configurations are listed in Table 10. The goals of the comparison are (i) to determine the differences introduced by the two retrieval codes when the same configuration is used and (ii) to quantify the total column differences introduced by each individual parameter. In particular, the following factors are analysed:

(a) The difference between nominal configuration (NC) using SFIT4 and the previous setup (PF) using PROFFIT9 code

(b) The difference between SFIT4 and PROFFIT9 using the same setup (PF).

(c) The difference due to updates in the spectroscopic database: HITRAN 2008 vs. HITRAN 2020 for example.

(d) The impact of the WACCM Model Versions: WACCM6 (41 years, 1980–2020) vs. IRWG7 (61 years, 1980–2040).

(e) The effect of using pre-retrieved H_2O profiles (Ortega et al., 2019).

https://doi.org/10.5194/essd-2026-762
Preprint. Discussion started: 6 November 2026
© Author(s) 2026. CC BY 4.0 License.



(f) The changes due to updates of the nominal setup retrieval strategy: CO remained OEM (Sect. 4.2.2), C_2H_6 changed from OEM to TP (Sect.4.2.3), and H_2CO changed from scaling to TP.

Table 10: Configurations used in the two retrieval codes.

Parameter	PROFFIT9 Configuration	SFIT4 / Nominal Configuration
Spectroscopic database	HITRAN 2008 or ATM2016	HITRAN 2020 or ATM 2020
T, P, a priori model and S_a	NCEP+WACCM6 (1980–2020)	NCEP+IRWG7 (1980–2040)

The comparison is quantified in terms of relative differences in total column (TC) evaluations of CO, C_2H_6 and H_2CO between a particular setup and a reference setup, for example the nominal setup in SFIT4 and the PROFFIT9 retrieval using the previous setup in the case (a):

$$\Delta TC = (TC_{SFIT4_NC} - TC_{PROFFIT9})/TC_{PROFFIT9}. \quad (14)$$

Here, TC_{SFIT4_NC} denotes the total columns from SFIT4 using nominal configuration, and $TC_{PROFFIT9}$ are the total columns from PROFFIT9.

The difference between the two codes (b), i.e. using the PROFFIT9 configuration (PF) within the SFIT4 code yields total column differences relative to PROFFIT9 of -0.30% for CO, +4.06% for C_2H_6 and -0.96% for H_2CO. The total column CO and H_2CO difference between two codes are in agreement with the finding from Hase et al. (2004) who found that deviations between the codes are smaller than 1% (C_2H_6, however, had not been investigated in this paper).

The relative total column differences (c) to (f) were computed as:

$$\Delta TC_{SFIT4_i} = (TC_{SFIT4_PF_i} - TC_{SFIT4_PF})/TC_{SFIT4_PF}, \quad (15)$$

ΔTC_{SFIT4_i} is the total column difference between $TC_{SFIT4_PF_i}$ and TC_{SFIT4_PF}, where TC_{SFIT4_PF} denotes the gas total column retrieved by SFIT4 using the PROFFIT9 configuration and i runs over the cases (c) to (f), with one parameter updated at a time from (c) to (f).

ΔTC_{SFIT4_i} of CO, C_2H_6 and H_2CO is shown for the different cases (c) to (f) in Table 11. According to Eqs. (14)-(15), $\Delta TC_{(a)}$ should be the sum of the individual of ΔTC_{SFIT4_i} for cases (c) to (f). The sums of individual contributions agree well with difference the value for case (a) for CO (-0.69% compared to -0.61%) and C_2H_6 (6.41% compared to 6.86%) H_2CO, however, shows a larger discrepancy, with a sum of -1.56% being about half of $\Delta TC_{(a)}$ = -3.03%. This discrepancy could be due to the implementation of the PROFFIT9 setup for SFIT4 which is not entirely equivalent. The PROFFIT9 configuration, the interfering species HDO and CH_4 were retrieved using a vertical constraint function which is not available in SFIT4. Consequently, the H_2CO $\Delta TC_{SFIT4_(b)}$ of -0.96% does not consider this difference, the summation from (b) to (f) should not completely reflect $\Delta TC_{(a)}$.

As presented in Table 11, after excluding the differences between the two retrieval codes (b), the main contributions to the total column difference are the update of IRWG7 model and the spectroscopic database. Notably, the application of the pre-

https://doi.org/10.5194/essd-2026-762
Preprint. Discussion started: 6 November 2026
© Author(s) 2026. CC BY 4.0 License.



retrieved H_2O profiles introduces a difference of around 1.5% in C_2H_6 (1.66%) and H_2CO (1.51%) retrievals, while its impact on CO is marginal (0.03%). As discussed in Section 4.2, pre-retrieved H_2O profiles are expected to better capture daily variations than the NCEP+IRWG7 model. These differences are larger for C_2H_6 and H_2CO than for CO, because the CO absorption lines are strong in the selected retrieval micro-windows, whereas the absorption lines for C_2H_6 and H_2CO contribute only about 5% and 2% to the spectral intensity within their retrieval micro-windows, respectively. Consequently, the larger discrepancies in the C_2H_6 and H_2CO retrieval is primarily due to the influences of interfering species. C_2H_6, for example, is primarily impacted by H_2O, whose absorption lines contribute roughly 50% of the spectral intensity within the C_2H_6 retrieval micro-windows (Fig. A11). H_2CO is mainly impacted by CH_4 and HDO, whereas HDO lines contribute 10% in H_2CO retrieval micro-windows (Fig. A15).

Table 11: Total column difference between PROFFIT9 and SFIT4, and the different updates for SFIT4. Evaluation of CO covers all data from 2019, C_2H_6 and H_2CO have been retrieved from 2020.

ΔTC	CO	C_2H_6*	H_2CO**
(a) SFIT4_NC vs PROFFIT9	**-0.61%**	**6.86%**	**-3.03%**
(b) SFIT4_PF vs PROFFIT9	-0.30%	4.06%	-0.96%*
(c) SFIT4_PF by changing to HITRAN 2020	0.14%	-1.74%	2.92%
(d) SFIT4_PF by changing to IRWG7 (A priori + S_a)	-0.56%	2.10%	-5.58%
(e) SFIT4_PF by changing to pre-retrieved H_2O profiles	0.03%	1.66%	1.51%
(f) SFIT4_PF by changing the retrieval strategy	0%	0.33%	0.55%
Sum: (b)+(c)+(d)+(e)+(f)	**-0.69%**	**6.41%**	**-1.56%**

*The C_2H_6 retrieval uses pseudo lines for both configurations, but interfering gases change from HITRAN 2008 to 2020.
**The H_2CO Spectroscopy is changed from ATM2016 to ATM2020, and comparison of (b) is slightly different for H_2CO, see text.

4.3.4 Post-processing data filters

The data have undergone network standards quality control procedures with outlier filtering to ensure reliability for trend analysis and scientific interpretation. The results obtained from the SFIT4 software inversions are filtered using several parameters before being included in the HDF format data file. In fact, the SFIT4 software allows users to enable certain parameters and apply broad limits for others to filter out bad data, such as negative values for the total and partial columns of the gas under study and H_2O, acceptable SZA values, acceptable DOF range, maximum FITRMS and retrieval convergence status. For the Paris site, we have added a second post-filtering by mixing certain parameters and adjusting the threshold values to reflect the specific conditions at Paris site in order to screen outliers and intend to remove spectra or retrievals with clear quality problems while retaining the natural variability of each species. The filtering method is based on three parameters: the FITRMS, χ^2, and the DOF of the target gas. In addition to these filters, we tested the FITRMS/DOF-ratio following the methane

https://doi.org/10.5194/essd-2026-762
Preprint. Discussion started: 6 November 2026
© Author(s) 2026. CC BY 4.0 License.



retrieval strategy of Sussmann et al. (2011). In that study, the ratio was introduced because both, the FITRMS and the DOF of CH_4, showed a seasonal cycle. We do not apply this ratio as a filter for the other gases, for which the FITRMS and DOF thresholds are used as two independent quality filters.

Filter parameter thresholds are listed in Table 12. They were selected empirically for each species from the observed distributions of the retrieval quality parameters and from inspection of the time series. The aim was to place the limits outside the normal retrieval range, so that isolated outliers are removed while coherent short-term or seasonal atmospheric variability is not compromised.

The expected behaviour of each filtering parameter was considered separately. FITRMS is expected to remain within the main low-residual range for a stable retrieval, but its absolute value is not directly comparable across species because it depends on the selected micro-windows, absorption depths, interfering species, and residual structure. The CO FITRMS limit and the CH_4 FITRMS/DOF criterion should therefore not be interpreted as equivalent normalized constraints, even though both species have strong absorption features. The χ^2 threshold checks whether the residual remains broadly consistent with the assumed retrieval noise. The DOF filter retains retrievals below the species-specific upper thresholds listed in Table 12. As described previously, the additional FITRMS/DOF < 0.25% threshold is introduced for CH_4 to be consistent with Sussmann et al. (2011). For HF and HCl, the different FITRMS and χ^2 limits reflect the different spectral constraints for the two isolated-line retrievals: HF is retrieved from a single MW, whereas HCl is retrieved from three MWs (see Figs. A1 and A3). The HCl spectral fit is therefore better constrained and more stable, allowing stricter FITRMS and χ^2 thresholds of 1% and 2, respectively. The DOF thresholds are similar for the two species, with moderate limits of 3 for HF and 3.5 for HCl. HF also uses a larger daily variation threshold than HCl. This choice is based on the larger scatter observed for the single micro-window HF retrievals. The threshold is kept intentionally tolerant so that the filter removes only pronounced outliers and does not discriminate possible short-term variability. For species with weaker absorption features or stronger sensitivity to spectral interference, such as HCN, H_2CO, NO_2 and OCS, the thresholds are adjusted to avoid rejecting most of the available retrievals while still removing clear outliers. For example, HCN uses a relatively loose FITRMS threshold of 10% because of its weak and variable signal, whereas NO_2 uses a stricter FITRMS threshold of 0.5% to control the spectral fit quality.

The daily variation filter is calculated from the relative difference between each retrieved total column and the daily median. A retrieval is retained when this difference is below the species-specific limit in Table 12. For long-lived and stable products such as CH_4 and N_2O, only small within-day variations are expected, so narrow limits are sufficient to remove isolated retrieval outliers. Larger limits are used for species with weaker absorption features, stronger spectral interference, or larger short-term atmospheric variability.

In summary, the thresholds listed in Table 12 should be understood as broad, species-specific outlier filters. They were chosen to be as non-restrictive as possible while still excluding retrievals with clear spectral-fit problems, inconsistent noise behaviour, or isolated departures from the daily variation. The rejection fractions remain small for all species, between 1.9% and 5.5%, indicating that the filters remove only a limited number of outliers, while retaining the majority of retrievals.

https://doi.org/10.5194/essd-2026-762
Preprint. Discussion started: 6 November 2026
© Author(s) 2026. CC BY 4.0 License.



Open Access Earth System Science Data Discussions

Table 12: Species-dependent post-retrieval filtering thresholds for Paris NDACC-IRWG retrievals. Retrievals are retained only when FITRMS, χ^2, DOF, and daily variation are below their respective thresholds.

Species	FITRMS (%)	χ^2	DOF	Daily variation (%)	Total data filtered out (%)
C_2H_6	4	4	3	18.0	2.6
HF	5	4	3	30.0	3.0
HCl	1	2	3.5	18.0	2.5
N_2O	1.5	2	5	5.0	3.3
CO	5	5	3.5	18.0	2.8
HCN	10	1	3.5	80.0	3.3
CH_4	1	2	3.5	5.0	5.5
H_2CO	1	3	1.5	100.0	1.9
NO_2	0.5	2	2.5	100.0	3.6
OCS	8	1	4	15	1.9

5 The FTS-Paris NDACC-IRWG time series

5.1 Automated SFIT4 processing

To make the Paris product reproducible and to enable faster re-analysis (with less human action) of the data-processing workflow over the full record, the routine SFIT4 processing is automated with our Sfit4Proc software that has been developed in Python. The workflow converts raw spectra into Hierarchical Data Format (HDF) products using the nominal retrieval settings described in Sect. 4. Users define the SFIT4 control file for the selected gas and configure the processing period, optical filter, and a priori options through a configuration file (sft4.ctl) for Sfit4Proc. This design keeps the retrieval recipe explicit while allowing the same processing chain to be applied consistently to all species and evaluation periods.

A key strength of Sfit4Proc is its ability to parallelize large-scale retrievals. Running 12 threads in parallel, a full retrieval cycle from 2011 to 2022 for a single gas takes approximately 40 hours, whereas the same process took more than a week when executed manually and without parallelization. We validated the automation procedure by comparing its output to manually retrieved results, confirming that automated results are consistent with the usual processing.

The retrieved results are then used to study seasonal variations and annual trends discussed in Sect. 5.3. Mean total columns, SNRs, DOFs, and retrieval errors for CH_4, N_2O, CO, C_2H_6, H_2CO, NO_2, OCS, HCl, HF and HCN are given in Table 13. The mean random and systematic errors are consistent with the discussion in Sect. 4.3.1, see Tables 7 and 8. Results of the DOF are also comparable to those of Table 4. The SNR is computed directly from the spectra. It is obtained as the ratio of the signal in the retrieval micro-windows (See Table 2) to the noise level determined from spectral regions out of the optical band, see Table A1.

https://doi.org/10.5194/essd-2026-762
Preprint. Discussion started: 6 November 2026
© Author(s) 2026. CC BY 4.0 License.



690 **Table 13: Summary of the FTS-Paris NDACC-IRWG retrieval products: mean total columns, mean SNR, mean DOF, mean random and systematic errors. Mean values are calculated over 2011-2022, except for HF and HCN, which cover 2018-2022. The errors were calculated during the retrieval using SFIT4_1.0.21 algorithm.**

Species	Mean total column ±1σ (molecules cm^{-2})	Mean SNR±1σ	Mean DOF±1σ	Mean Random error (%)	Mean Systematic error (%)
C_2H_6	(2.20 ± 0.58) E+16	205.16 ± 74.49	1.32 ± 0.18	4.62	10.51
HF	(1.62 ± 0.21) E+15	240.15 ± 100.13	1.96 ± 0.27	1.91	2.58
HCl	(3.66 ± 0.40) E+15	380.33 ± 114.26	2.12 ± 0.31	2.26	2.35
N_2O	(6.67 ± 0.10) E+18	281.26 ± 87.29	3.52 ± 0.28	0.30	5.71
CO	(2.06 ± 0.30) E+18	164.86 ± 60.74	2.07 ± 0.27	1.16	3.17
HCN	(4.97 ± 1.21) E+15	169.03 ± 85.77	1.43 ± 0.27	17.13	11.50
CH_4	(3.89 ± 0.07) E+19	399.65 ± 100.76	2.80 ± 0.26	0.73	3.35
H_2CO	(8.63 ± 5.20) E+15	390.26 ± 107.79	1.04 ± 0.04	6.63	16.88
NO_2	(1.14 ± 0.40) E+16	416.61 ± 112.35	1.39 ± 0.22	20.58	9.16
OCS	(9.92 ± 0.53) E+15	97.27 ± 38.08	2.44 ± 0.33	3.74	2.95

5.2 Seasonal and annual trend fit model

The temporal evolution of the total columns is represented with a linear term and periodic oscillation. The full record for most 695 products is available from 2011 onwards, while HF and HCN cover shorter periods because required filters have become available only later. The fit model is:

$$\hat{y}(t) = C_0 + C_1 * t + C_2 * \cos(2\pi(t - t_0) - \varphi_0), \quad (16)$$

where t is time expressed in fractional years, t_0 is the first day of the time series in fractional year and the coefficients C_0, C_1, C_2 and φ_0 are obtained from an unconstrained linear least square fit to the total column data. C_0 is the initial column value, C_1 700 is its slope, C_2 is the amplitude of the seasonal variation, and $\varphi_0/(2\pi)$ is the fraction of the year indicating the seasonal maximum (Rinsland et al., 2000, 2001). The record is not continuous, because unfavourable meteorological conditions and documented instrumental issues (see description in metadata of NDACC-Paris (https://ndacc.larc.nasa.gov/stations/paris-france) can create gaps in the observations. The fit is therefore applied to the available measurements to estimate annual trends and the amplitude and phase of the seasonal cycle. The interpretation of the fitted trends is given in Sect. 5.3.

705

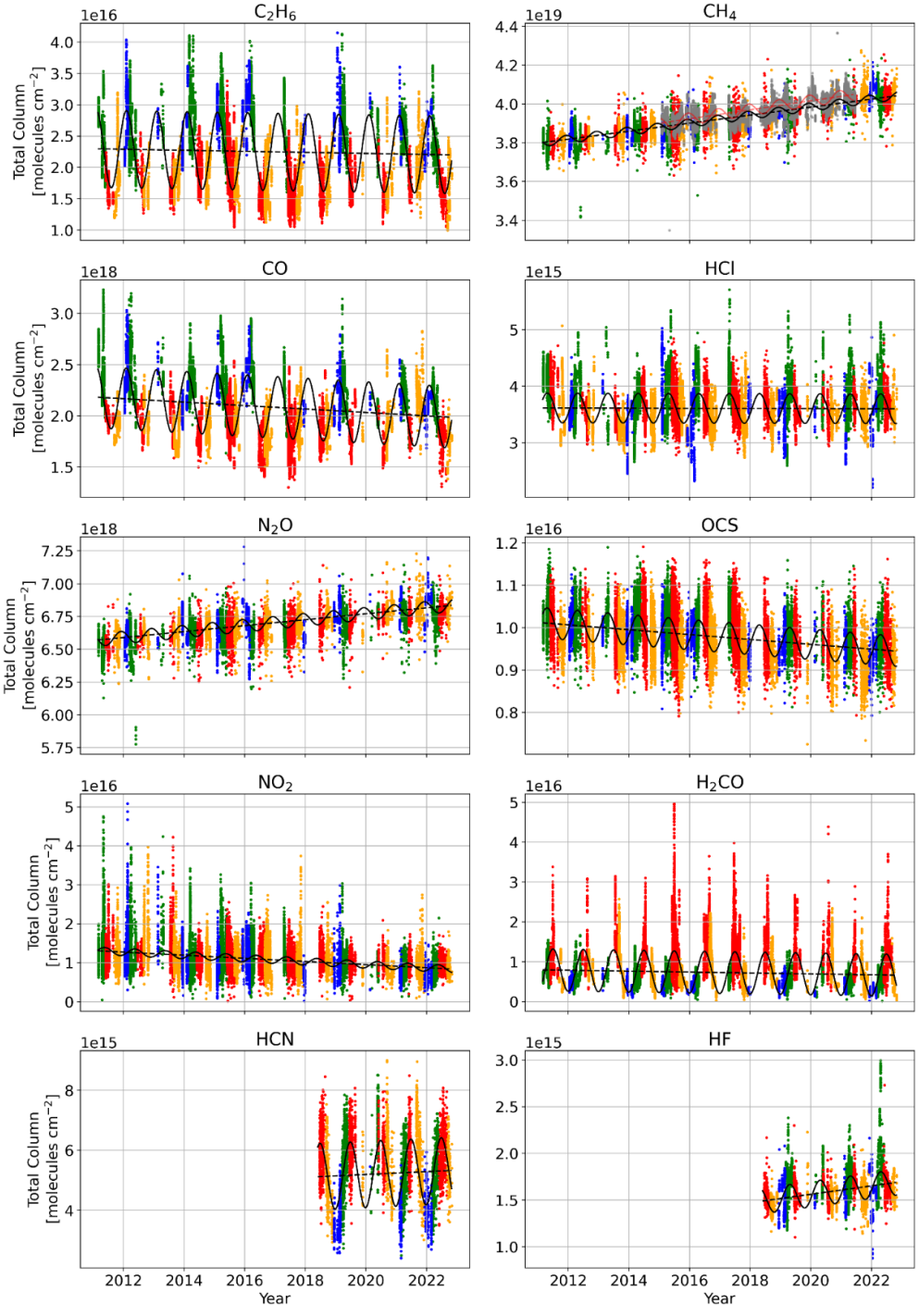
5.3 Trends and seasonal variations

Figure 11 shows the Paris total column time series of all species, together with their fitted seasonal and trend components obtained from Eq. (16). The coloured points denote individual FTIR measurements grouped by season, while the solid black 710 curves show the fitted seasonal cycle and the dashed black lines show the corresponding linear trend. The grey points and red fitting curves for CH_4, show the TCCON record used as an independent check. The detailed discussion of the individual gases focussing on the seasonality and the long-term trends starts with species that show increasing trends over 2011-2022, followed

https://doi.org/10.5194/essd-2026-762
Preprint. Discussion started: 6 November 2026
© Author(s) 2026. CC BY 4.0 License.



by species with decreasing trends, before turning to the records of gases that have only been measured over a much shorter period.



https://doi.org/10.5194/essd-2026-762
Preprint. Discussion started: 6 November 2026
© Author(s) 2026. CC BY 4.0 License.



Figure 11: Total column time series of 10 NDACC-IRWG gases at Paris from 2011 to 2022. Each dot represents an FTIR measurement, with colour coding for the meteorological seasons: green for MAM, red for JJA, orange for SON, and blue for DJF. The solid black curves show the fitted seasonal cycles, and the black dashed lines show the corresponding linear trends. The grey dots in the CH_4 panel represent FTS-Paris TCCON measurements, with the seasonal fit and linear trend shown in red.

Species with positive trends: CH_4 and N_2O

For NDACC-IRWG CH_4, the fitted seasonal amplitude is small but well resolved, 2.12×10^{17} molecules cm^{-2}, with a 2σ uncertainty of 8.79×10^{15} molecules cm^{-2}, corresponding to (0.54 ± 0.02) % of the mean column. Such a weak relative modulation is expected for a long-lived greenhouse gas where the total column is dominated by the hemispheric background. The fitted phase shows higher columns in November-January and lower columns in May-July. The CH_4 total columns exhibit a statistically significant positive trend of (0.53 ± 0.01) %/yr. The independent TCCON CH_4 record at Paris gives a similar trend of (0.58 ± 0.01) %/yr for 2015-2021 (Té et al., 2025), and both datasets display a comparable seasonal cycle (Fig. 11). The mean column difference between the FTS-Paris NDACC-IRWG and TCCON CH_4 measurements is -2.23%, which could be explained by differences in spectroscopy, a priori profile constraints, empirical airmass corrections, and retrieval strategies (Laughner et al., 2024). Published FTIR trends at Izaña ((0.43 ± 0.03) %/yr, 2009–2019), Toronto ((0.41 ± 0.03) %/yr, 2002–2019), Hefei ((0.56 ± 0.15) %/yr, 2014–2017), Maïdo (0.51 ± 0.04) %/yr, and other NDACC sites are also positive, supporting the consistency of the Paris CH_4 product (Bader et al., 2017; García et al., 2021; Tian et al., 2018; Timofeyev et al., 2016; Yamanouchi et al., 2021; Zhou et al., 2018).

For N_2O, the fitted seasonal term is similarly small, with an amplitude of 4.82×10^{16} molecules cm^{-2}, and an uncertainty of 1.60×10^{15} molecules cm^{-2}, equivalent to (0.72 ± 0.01) % of the mean. This weak variability is expected for an even longer-lived greenhouse gas. The phase is similar to CH_4 with a November-January Maximum and a May-July minimum. The N_2O total columns show a positive trend of (0.34 ± 0.01) %/yr over 2011-2022. This value is consistent with documented FTIR trends at Izaña (0.31 ± 0.03) %/yr for 2009-2019 (García et al., 2021), Toronto (0.28 ± 0.02) %/yr for 2002-2019 (Yamanouchi et al., 2021), and the 12 NDACC stations analyzed by Barret et al. (2021), which reported rates between 0.28 and 0.36%/yr over 2008-2018.

Species with negative trends: CO, C_2H_6, H_2CO, NO_2 and OCS

CO has one of the clearest seasonal cycles among the Paris products. The fitted amplitude reaches 3.01×10^{17} molecules cm^{-2}, with an uncertainty of 3.36×10^{15} molecules cm^{-2}, or (14.60 ± 0.16) % of the mean. The January-March maximum and July-September minimum are expected for CO at northern mid-latitudes, reflecting higher winter-to-spring columns under weaker OH removal, followed by more efficient photochemical loss in summer (Té et al., 2016). Between 2011 and 2022, CO at Paris exhibits a decreasing trend of (−0.80 ± 0.04) %/yr. This decrease is consistent with published FTIR trends at Eureka ((−0.84 ± 0.23) %/yr, 2006-2020), Thule ((−0.76 ± 0.17) %/yr, 1999-2022), Toronto ((−0.90 ± 0.07) %/yr, 2002-2019), Lauder ((−0.94

https://doi.org/10.5194/essd-2026-762
Preprint. Discussion started: 6 November 2026
© Author(s) 2026. CC BY 4.0 License.



± 0.29) %/yr, 2007-2017), Kiruna ((−0.61 ± 0.16) %/yr, 1996-2006), Zugspitze ((−1.00 ± 0.24) %/yr, 1996-2006), and Arrival Heights ((−0.92 ± 0.46) %/yr, 1997-2009), while the magnitude differs among sites because of differences in period, latitude, altitude, and regional emissions (Angelbratt et al., 2011b; Bader et al., 2017; García et al., 2021; Smale et al., 2019; Wizenberg et al., 2024; Yamanouchi et al., 2021). The Paris result therefore falls within the range of decrease rates reported for northern hemispheric FTIR CO. Overall, CO trends have remained consistently negative across both recent and historical datasets.

C_2H_6 follows the same winter-high/summer-low phase as CO, but with a stronger relative modulation. The fitted amplitude is 6.17×10^{15} molecules cm^{-2}, with an uncertainty of 6.04×10^{13} molecules cm^{-2}, corresponding to (28.08 ± 0.27) % of the mean. The C_2H_6 record shows an overall decrease of (−0.37 ± 0.01) %/yr over 2011-2022. This weak negative long-term trend is compatible with the broader picture from published northern hemispheric FTIR studies, which report strong regional and temporal variability and a transition from early-2010s increases to later stagnation or decline (Angot et al., 2021; Franco et al., 2016; Friedrich et al., 2020; García et al., 2021; Sun et al., 2021; Wizenberg et al., 2024; Yamanouchi et al., 2021; Zhu et al., 2024). A separate global NDACC ethane breakpoint analysis (Friedrich et al., 2026) identified an increase before 2013 followed by stagnation or slight decline thereafter.

The seasonal behaviour of H_2CO differs from CO and C_2H_6 as expected for a short-lived species with strong photochemical production. The fitted maximum occurs in June-August and the minimum in December-February, with an amplitude of 5.27×10^{15} molecules cm^{-2} and an uncertainty of 8.14×10^{13} molecules cm^{-2}, representing (61.10 ± 0.94) % of the mean. This large relative cycle is consistent with VOC oxidation during the summer season and the short lifetime of H_2CO (Luecken et al., 2018; Vigouroux et al., 2018). Without additional modelling, however, it cannot be interpreted as a regional source trend. H_2CO total columns over Paris show a negative trend of (-1.58 ± 0.23) %/yr from 2011 to 2022. Published FTIR records also report negative trends at several urban or continental sites, including Toronto ((-0.43 ± 0.25) %/yr, 2002–2019), Hefei ((-2.31 ± 0.01) %/yr, 2015–2021), Zugspitze ((-0.77 ± 0.77) %/yr, 1995–2017), Saint Petersburg ((-0.39 ± 0.33) %/yr, 2009-2017), Mexico City ((-0.96 ± 0.51) %/yr, 2013-2016), and Wollongong ((-1.88 ± 1.08) %/yr, 1996-2016). Given its relatively short lifetime, the spatial distribution of H_2CO is highly inhomogeneous, with peaks near the sources. Trends vary from site to site and some sites close to the ocean show even positive trends, such as Izaña and Saint-Denis (Zhu et al., 2024; Yamanouchi et al., 2021; Lieschke et al., 2019; Vigouroux et al., 2018).

The NO_2 annual cycle is weaker than that of the short-lived carbon species, but remains visible in the fit. Its amplitude is 9.35×10^{14} molecules cm^{-2}, with an uncertainty of 7.92×10^{13} molecules cm^{-2}, equal to (8.22 ± 0.70) % of the mean. The fitted maximum occurs in May-July and the minimum in November-January. NO_2 shows the strongest relative decline among Paris products. The total columns decrease by (-3.80 ± 0.15) %/yr. This decrease agrees with a post-2011 decline in stratospheric NO_2 reported by García et al. (2021), and with earlier satellite-derived trends at Paris of about -4%/yr for 2002-2012 (Schneider

https://doi.org/10.5194/essd-2026-762
Preprint. Discussion started: 6 November 2026
© Author(s) 2026. CC BY 4.0 License.



et al., 2015). Other ground-based and satellite studies also report decreasing NO_2 over parts of Europe and East Asia, although the magnitude depends strongly on the column type, region and period (Diémoz et al., 2021; Han, 2019).

The seasonal cycle of OCS is modest compared to that of the reactive carbon species. The fitted amplitude is 3.60×10^{14} molecules cm^{-2}, with an uncertainty of is 8.08×10^{12} molecules cm^{-2}, corresponding to (3.63 ± 0.08) % of the mean. The phase shows higher columns in April-June and lower columns in October-December. The magnitude of the seasonality is consistent with OCS being a relatively long-lived sulfur species with distributed sources and sinks. Being outside the scope of this paper, we do not attempt to discuss the detailed partitioning between biospheric uptake, oceanic sources, and stratospheric processes at Paris. The FTS-Paris OCS total columns show a decreasing trend of (-0.59 ± 0.02) %/yr from 2011 to 2022. This is consistent with the recent slowdown and decline discussed by Hannigan et al. (2022a), who reported two tropospheric trend periods, with increases before 2016 and likely decreases afterwards.

Halogen reservoir records: HCl and HF

Stratospheric components such as HF and HCl provide critical information on the atmospheric halogen load. As long-lived and stable chemical species in the stratosphere, they serve as dominant reservoirs of stratospheric fluorine and chlorine, (Mahieu et al., 2008, 2014; Steffen et al., 2019) and can serve as conservative tracers (Akishina et al., 2024). HCl is a major chlorine reservoir linked to ozone depletion, whereas HF is a stable fluorine reservoir and tracer of halogenated organic source gases (Chipperfield et al., 1997).

The HCl seasonal cycle is well defined despite the weak long-term trend. Its amplitude is 2.63×10^{14} molecules cm^{-2}, with an uncertainty of 6.23×10^{12} molecules cm^{-2}, or (7.17 ± 0.17) % of the mean. Maxima are found in April-June and minima in October-December. This is consistent with previously reported FTIR HCl seasonal cycles, for which lower-stratospheric dynamical variability and tropopause height changes have been identified as important drivers, rather than local source seasonality (Kohlhepp et al., 2012; Rinsland et al., 1991; Yin et al., 2020). The HCl total column over Paris shows a non-significant trend of (−0.03 ± 0.04) %/yr from 2011 to 2022. This weak trend is consistent with the slight negative or near-stagnant HCl trends reported at Toronto ((−0.21 ± 0.19) %/yr, 2002-2019), Izaña ((−0.11 ± 0.04) %/yr, 1999-2019), and St. Petersburg ((−0.26 ± 0.21) %/yr, 2009-2023) (Akishina et al., 2024; García et al., 2021; Yamanouchi et al., 2021). The levelling-off relative to previously reported negative trends can be linked to the change of sources: Reductions of chlorofluorocarbons (CFCs) under the Montreal Protocol decreased the chlorine load, whereas hydrochlorofluorocarbons (HCFCs) and related substitutes continued to contribute chlorine and fluorine during later periods (Zhou et al., 2016).

The shorter HF record gives a seasonal amplitude of 1.37×10^{14} molecules cm^{-2}, with an uncertainty of is 7.39×10^{12} molecules cm^{-2}, equivalent to (8.42 ± 0.46) % of the mean. The April-June maximum and October-December minimum are close to those found for HCl. This agreement is consistent with the common stratospheric character of the two halogen-reservoir columns; although the shorter Paris HF record means that the fitted amplitude and phase should be reported as descriptive rather than

https://doi.org/10.5194/essd-2026-762
Preprint. Discussion started: 6 November 2026
© Author(s) 2026. CC BY 4.0 License.



climatological parameters. The HF time series starting in 2018 shows a clear positive trend of (2.84 ± 0.22) %/yr. This is similar to earlier FTIR observations from other sites. The Toronto Atmospheric Observatory has observed a rise of (0.59 ± 0.11) %/yr between 2002 and 2019 (Yamanouchi et al., 2021), and Izaña recorded a (0.98 ± 0.27) %/yr increase from 1999 to 2019 (García et al., 2021). Akishina et al. (2024) also reported positive trends for St. Petersburg ((0.59 ± 0.27) %/yr, 2009-2023), Kiruna ((0.67 ± 0.35) %/yr, 2009-2023), and Harestua (0.43 ± 0.27) %/yr, while trends over earlier periods were weaker or ambiguous (Kohlhepp et al., 2012).

Short-record case: HCN

Even though the observational record is very short, HCN shows a clear and substantial seasonal cycle, with an amplitude of 1.11×10^{15} molecules cm^{-2} and an uncertainty of is 3.79×10^{13} molecules cm^{-2}, representing (20.16 ± 0.69) % of the mean. The fitted maximum occurs in June-August and the minimum in December-February. Such a large relative seasonal term is not unexpected for HCN, given its sensitivity to biomass burning plumes and episodic long-range transport reported in previous FTIR studies (Viatte et al., 2013; Zeng et al., 2012; Zhu et al., 2024). The FTS-Paris HCN record shows a positive, but statistically uncertain trend of (0.51 ± 0.43) %/yr from 2018 to 2022 (Fig. 11). In contrast, negative trends were reported at Toronto (-0.51 ± 0.21) %/yr, 2002–2019 and Hefei (-2.31 ± 0.09) %/yr, 2015–2021 (Zhu et al., 2024; Yamanouchi et al., 2021). Earlier measurements from 1999 to 2009 also show negative trends at Fort Lauder (-0.62 ± 0.31) %/yr and Arrival Heights (-0.75 ± 0.38) %/yr (Zeng et al., 2012).

6 Summary and conclusions

The SFIT4 processing at FTS-Paris provides a quality-controlled urban NDACC-IRWG product record for CO, C_2H_6, CH_4, N_2O, HF, HCl, HCN, H_2CO, NO_2 and OCS. The record covers 2011-2022 for most species and 2018-2022 for HF and HCN, with species-specific retrieval settings in accordance with NDACC-IRWG recommendations and adapted to observing conditions at Paris. The use of updated spectroscopy, IRWG a priori information, and pre-retrieved H_2O supports a consistent retrieval framework for long-term analysis and future network intercomparisons.

The retrieval tests lead to a nominal configuration, with OEM retained for HF, HCl, CO, and OCS, and TP retained for N_2O, C_2H_6, CH_4, HCN, H_2CO, and NO_2. This configuration should be understood as the most appropriate retrieval strategy for the Paris spectra and observing conditions, rather than as a universal prescription for other sites or implementations. Different spectral conditions, target gas sensitivities, noise levels, and profile constraints, may demonstrate another preference for either OEM or TP in terms of effectiveness and stability. The preferred strategy should therefore be selected following site-specific tests for each species. The associated quality assessment defines the strengths and limitations of the product. Random errors are mainly driven by retrieval noise, while systematic errors are mainly linked to spectroscopy. The ILS approximation impacts total columns by less than 1%. About 2-6% of the observations are removed by the post-processing filtering on average. The comparison with previous PROFFIT9 products shows differences below 1% for CO and H_2CO and about 4% for C_2H_6. This

https://doi.org/10.5194/essd-2026-762
Preprint. Discussion started: 6 November 2026
© Author(s) 2026. CC BY 4.0 License.



article also presents an investigation of updating to the latest a priori profile and spectroscopy database. The main change is due to the updated a priori model, which introduces biases of –5.6% for H_2CO and +2.1% for C_2H_6. The spectroscopic update contributes +2.9% to H_2CO and –1.7% for C_2H_6. Using pre-retrieved water vapor contributes about +1.5% to columns of H_2CO and C_2H_6, whereas the change in retrieval strategy accounts for less than 0.6% of the total column difference. CO shows the most stable results of the three gases, with each update contributing less than 0.6% in absolute value. Unlike CO and C_2H_6, for which calculated and theoretical error summations agree closely, H_2CO shows a slightly larger discrepancy, mainly because SFIT4 could not fully reproduce the vertical constraints for interfering species HDO and CH_4 used in the previous PROFFIT9 setup.

While CH_4 and N_2O exhibit positive trends over the 2011-2022 period, CO, C_2H_6, H_2CO, NO_2 and OCS decrease. HCl remains close to stagnant over the same period. HF shows a clear positive tendency over the short 2018-2022 record. The positive HF trend observed at Paris, which is larger than those already published and covering longer periods, calls for observations from other sites over the same period to assess whether our observation reflects a recent general change. HCN also has a shorter record with a positive but statistically uncertain trend. These tendencies are presented as Paris site results, rather than as a new multi-site assessment. Comparisons within NDACC are therefore limited to previously published site studies, and both, the HF and HCN products must be interpreted cautiously because of their relatively short record.

Hannigan et al. (2022a) reported a positive global OCS trend from 2008 to 2016 followed by an inflection and less certain behaviour afterwards. The decrease in OCS total columns observed at Paris during 2011-2022 is consistent with this suggested decline. A more comprehensive global analysis combining observations from multiple sites is however needed to clarify the timing, magnitude, and geographical extent of these changes. Attributing their causes will require public multi-site products and comprehensive chemistry-transport modelling and is beyond the scope of this paper. Published FTIR studies also report contrasting trends. Overall, the NDACC-Paris dataset fills an important gap in high-precision, ground-based observations of atmospheric trace gases in the Paris region and provides a reference for future validation and network studies.

Code and data availability

The SFIT4 retrieval code is available at https://wiki.ucar.edu/spaces/sfit4/overview (Hannigan et al., 2022b). The Paris FTIR data are regularly archived in the NDACC repository at https://www-air.larc.nasa.gov/pub/NDACC/PUBLIC/stations/paris/hdf/ftir/, and the data presented in this work are available on Zenodo at https://doi.org/10.5281/zenodo.23359690 (Té et al., 2026).

https://doi.org/10.5194/essd-2026-762
Preprint. Discussion started: 6 November 2026
© Author(s) 2026. CC BY 4.0 License.



Open Access Earth System Science Data Discussions

Appendix A: Additional material

Appendices A1 and A2 provide the retrieval output examples from raw spectra obtained at around 12:00 UTC, 6 August 2020 for the gases not shown in the main text. The main text uses CO and CH_4 for illustrating the OEM and the TP retrievals, respectively. The appendix figures keep the same format, showing the retrieval micro-windows and the corresponding retrieved vertical profiles, so that the retrieval of these remaining species is well illustrated and accessible.

A1 OEM retrieval examples

This appendix presents the retrieval micro-windows and vertical profiles for all gases (HF, HCl, OCS and H_2O) retrieved with the OEM method except for CO which is discussed in Sect. 4.2.2 of the main text.

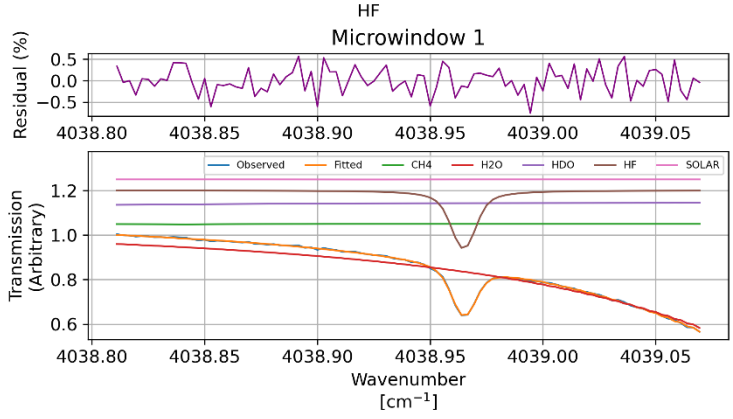


Figure A1: Measured (blue) and fitted (orange) spectrum in the 1 HF MW's recorded on 6 of August 2020 at Paris. The residuals are shown in purple.

https://doi.org/10.5194/essd-2026-762
Preprint. Discussion started: 6 November 2026
© Author(s) 2026. CC BY 4.0 License.

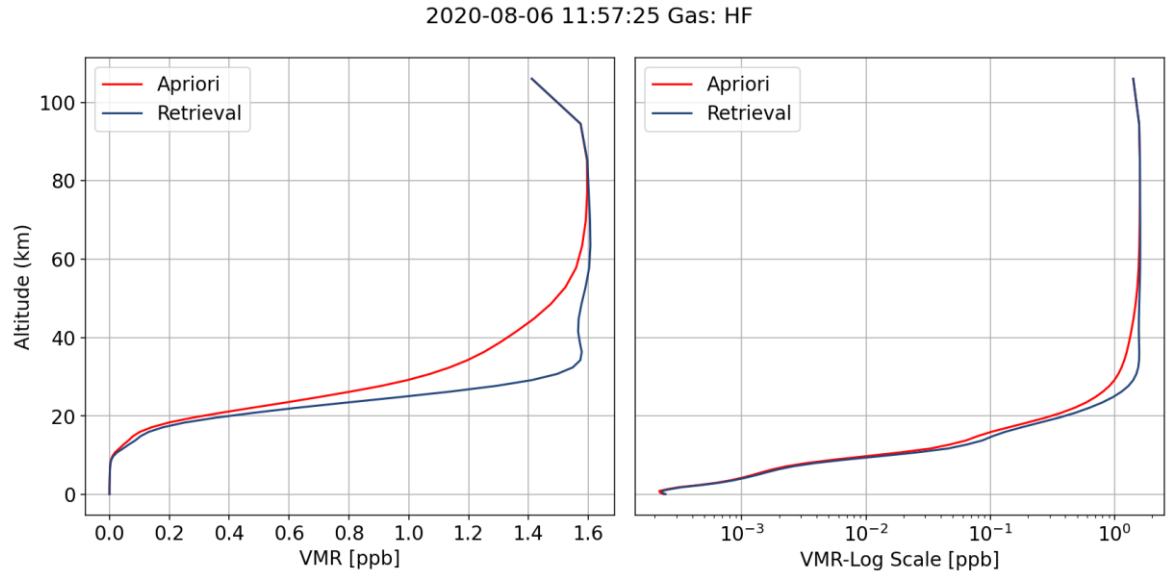


Figure A2: A priori (red) and retrieved (blue) HF profiles of the spectrum shown above. Left: volume mixing ratio in normal scale. Right: volume mixing ratio in logarithmic scale.

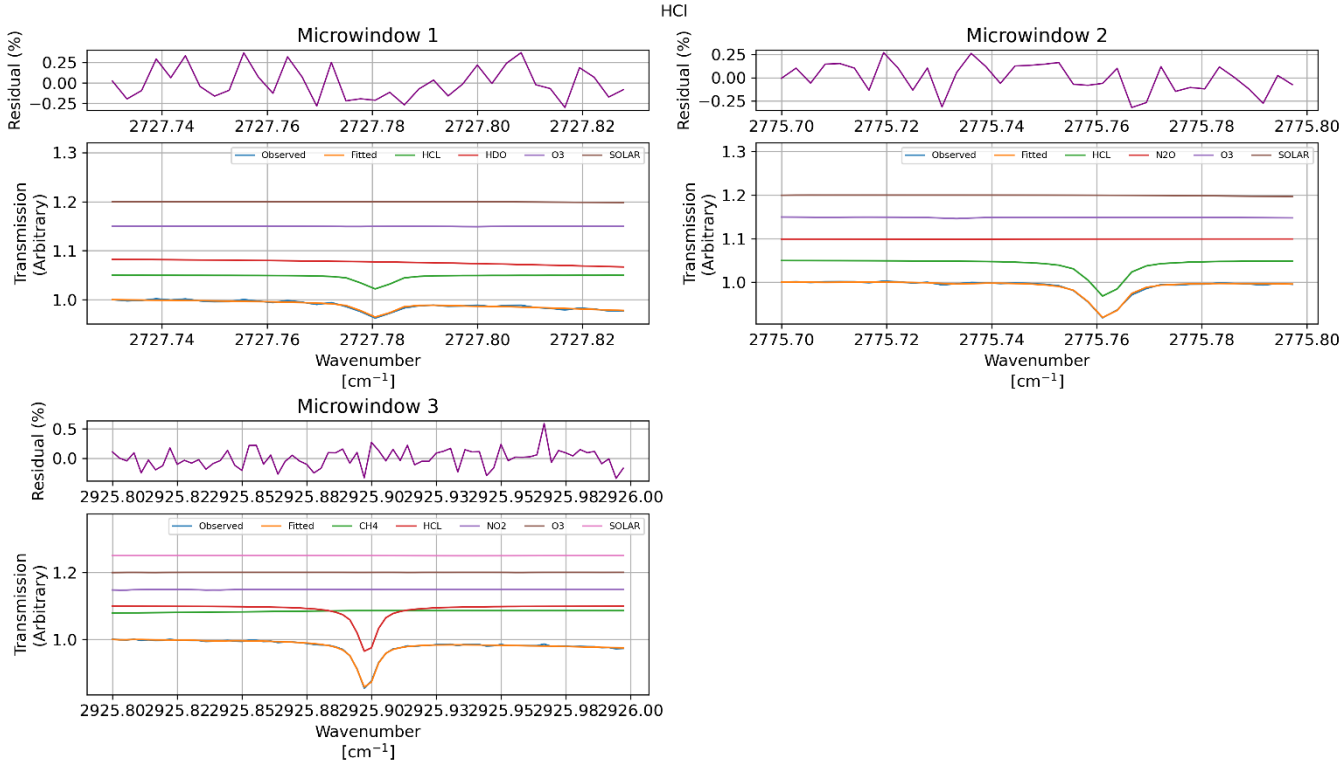


Figure A3: Measured (blue) and fitted (orange) spectrum in the 3 HCl MW's recorded on 6 of August 2020 at Paris. The residuals are shown in purple.

https://doi.org/10.5194/essd-2026-762
Preprint. Discussion started: 6 November 2026
© Author(s) 2026. CC BY 4.0 License.

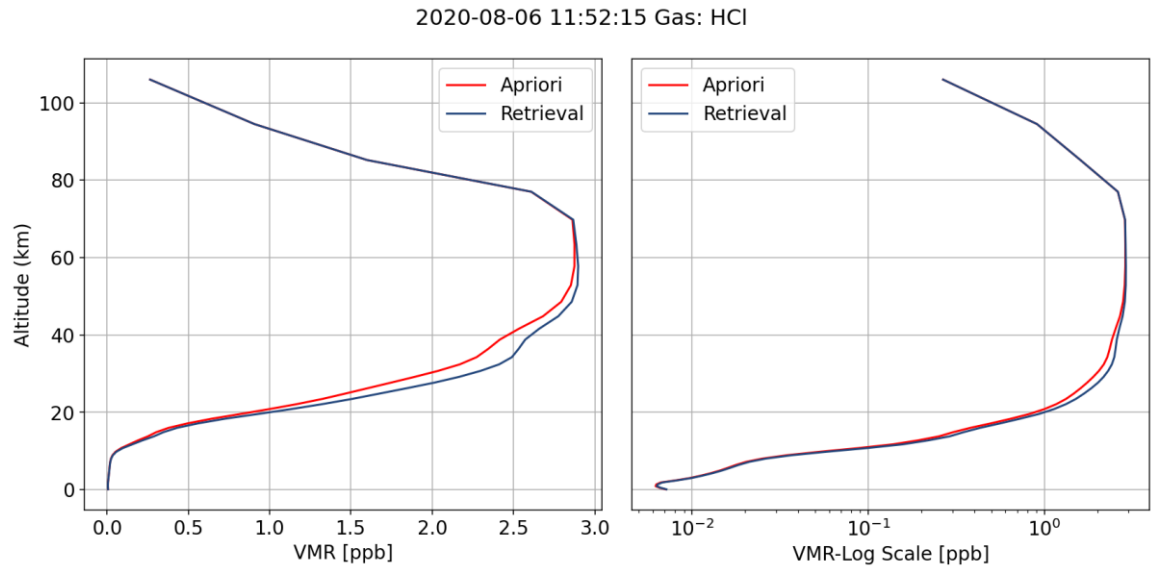


Figure A4: A priori (red) and retrieved (blue) HCl profiles of the spectrum shown above. Left: volume mixing ratio in normal scale. Right: volume mixing ratio in logarithmic scale.

https://doi.org/10.5194/essd-2026-762
Preprint. Discussion started: 6 November 2026
© Author(s) 2026. CC BY 4.0 License.

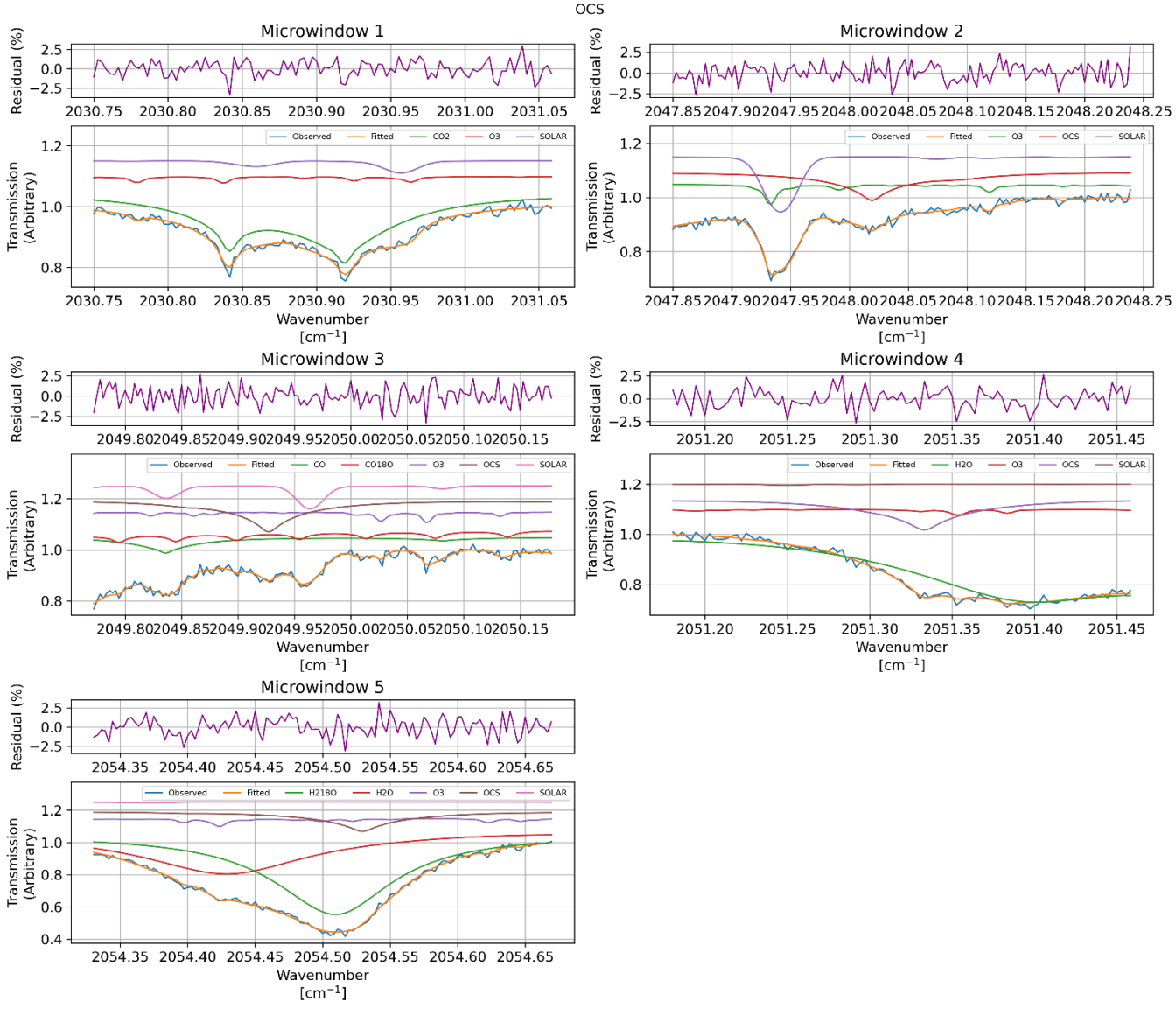


Figure A5: Measured (blue) and fitted (orange) spectrum in the 5 OCS MW's recorded on 6 of August 2020 at Paris. The residuals are shown in purple.

900

https://doi.org/10.5194/essd-2026-762
Preprint. Discussion started: 6 November 2026
© Author(s) 2026. CC BY 4.0 License.

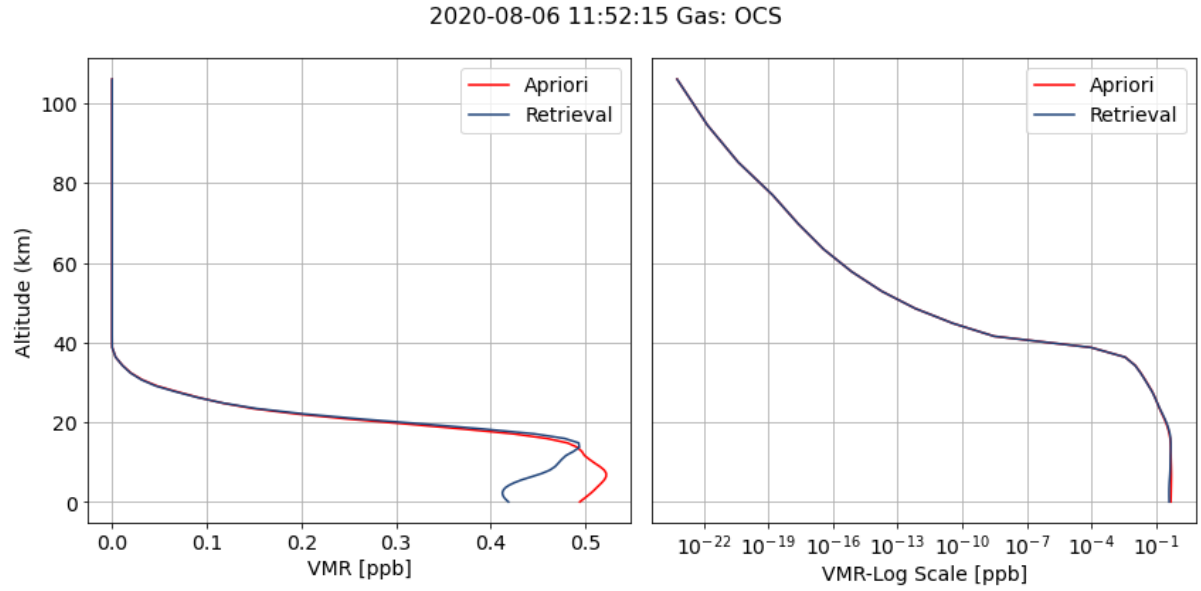


Figure A6: A priori (red) and retrieved (blue) OCS profiles of the spectrum shown above. Left: volume mixing ratio in normal scale. Right: volume mixing ratio in logarithmic scale.

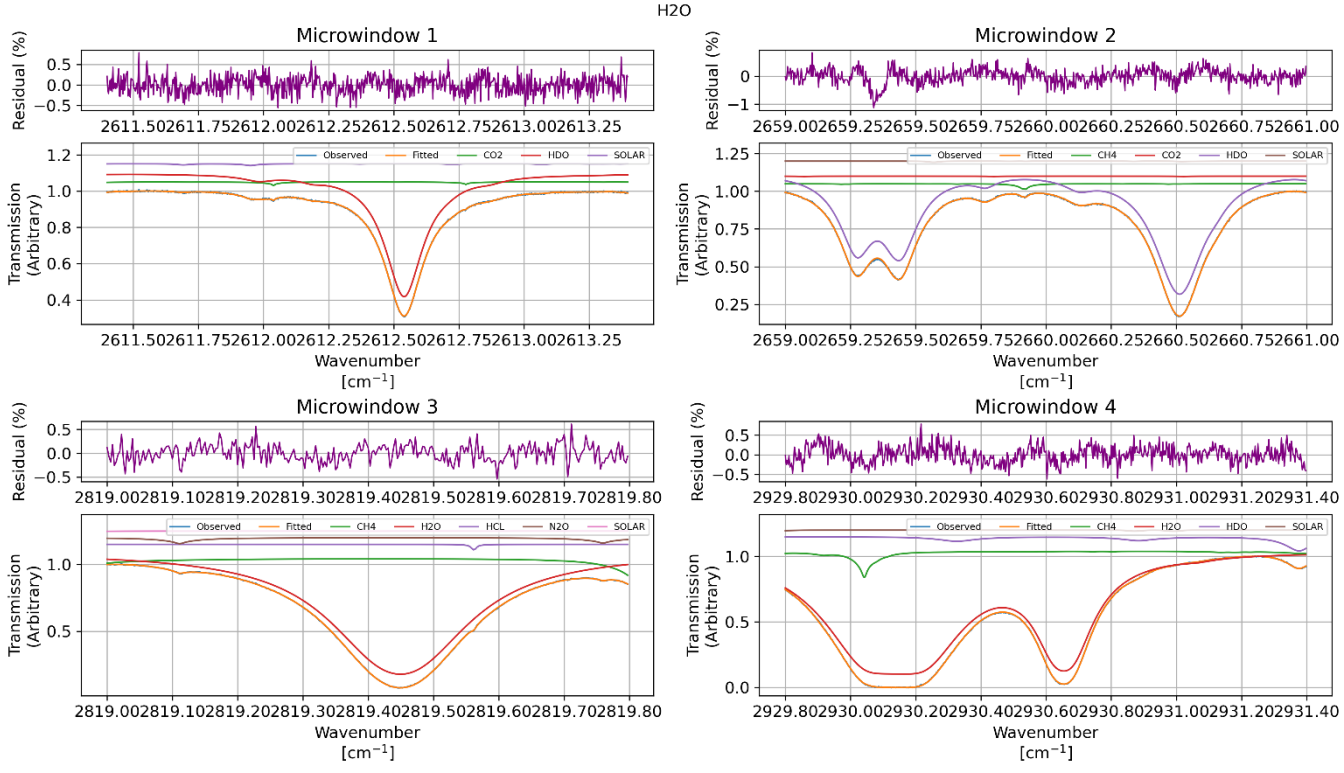


Figure A7: Measured (blue) and fitted (orange) spectrum in the 4 H_2O MW's recorded on 6 of August 2020 at Paris. The residuals are shown in purple.

https://doi.org/10.5194/essd-2026-762
Preprint. Discussion started: 6 November 2026
© Author(s) 2026. CC BY 4.0 License.

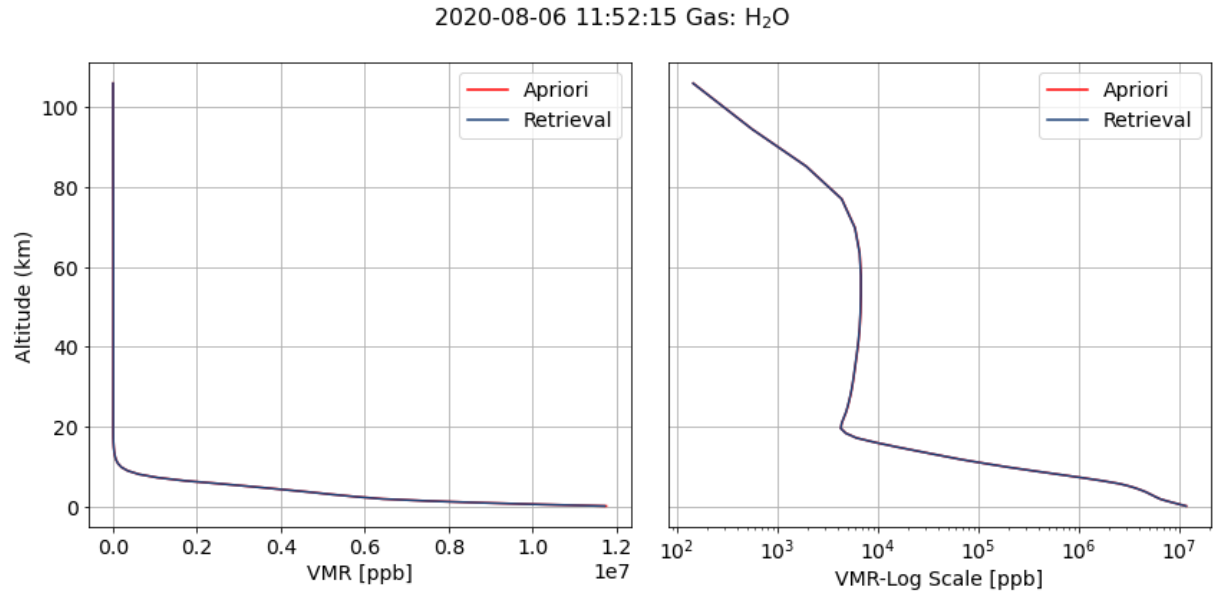


Figure A8: A priori (red) and retrieved (blue) H_2O profiles of the spectrum shown above. Left: volume mixing ratio in normal scale. Right: volume mixing ratio in logarithmic scale.

A2 TP retrieval examples

This appendix presents the retrieval micro-windows and vertical profiles for all gases (N_2O, C_2H_6, HCN, H_2CO and NO_2) retrieved using the TP strategy except for CH_4 which is discussed in Sect. 4.2.3 of the main text.

https://doi.org/10.5194/essd-2026-762
Preprint. Discussion started: 6 November 2026
© Author(s) 2026. CC BY 4.0 License.

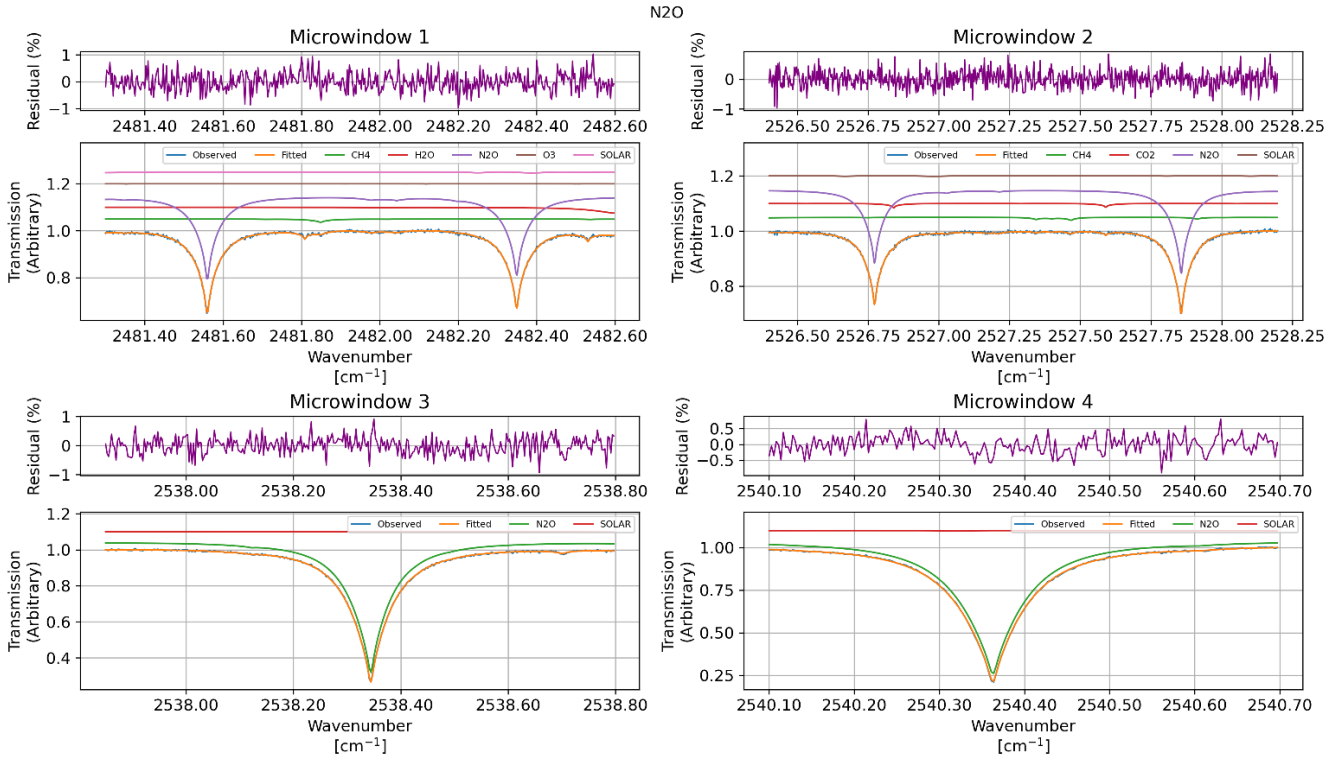


Figure A9: Measured (blue) and fitted (orange) spectrum in the 4 N_2O MW's recorded on 6 of August 2020 at Paris. The residuals are shown in purple.

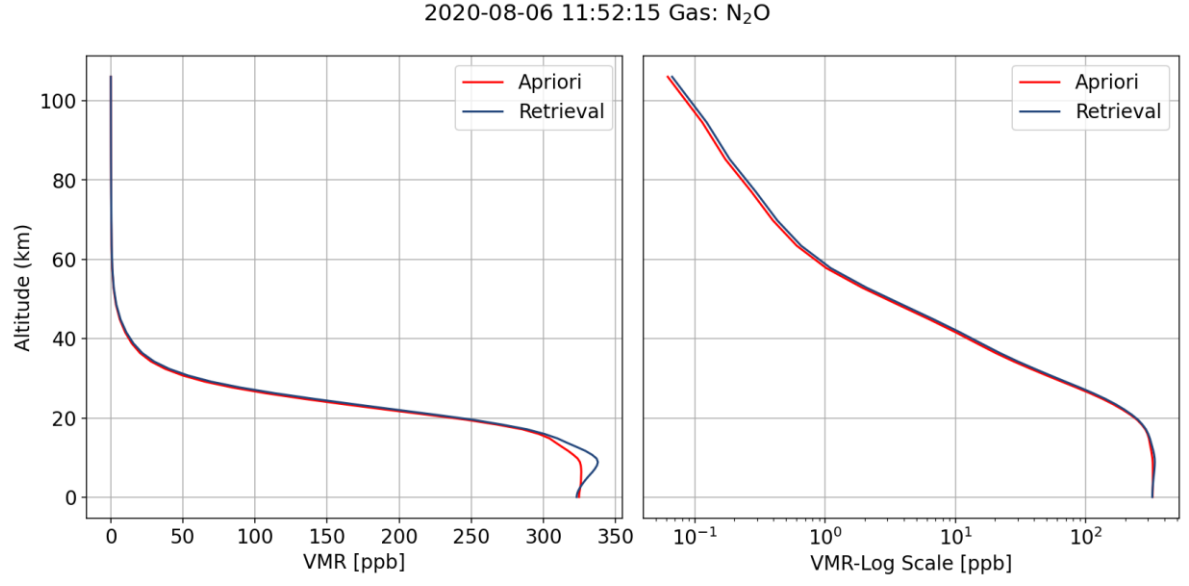


Figure A10: A priori (red) and retrieved (blue) N_2O profiles of the spectrum shown above. Left: volume mixing ratio in normal scale. Right: volume mixing ratio in logarithmic scale.

https://doi.org/10.5194/essd-2026-762
Preprint. Discussion started: 6 November 2026
© Author(s) 2026. CC BY 4.0 License.

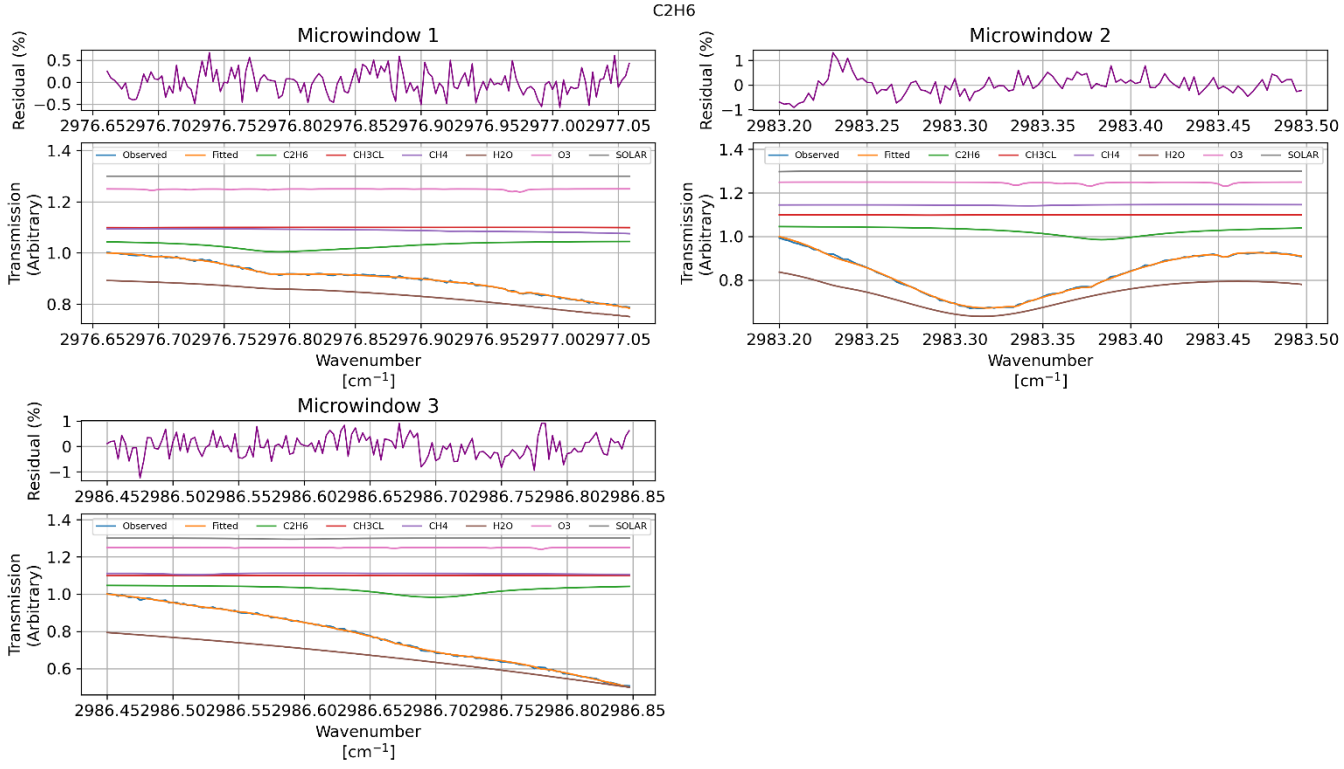


Figure A11: Measured (blue) and fitted (orange) spectrum in the 3 C_2H_6 MW's recorded on 6 of August 2020 at Paris. The residuals are shown in purple.

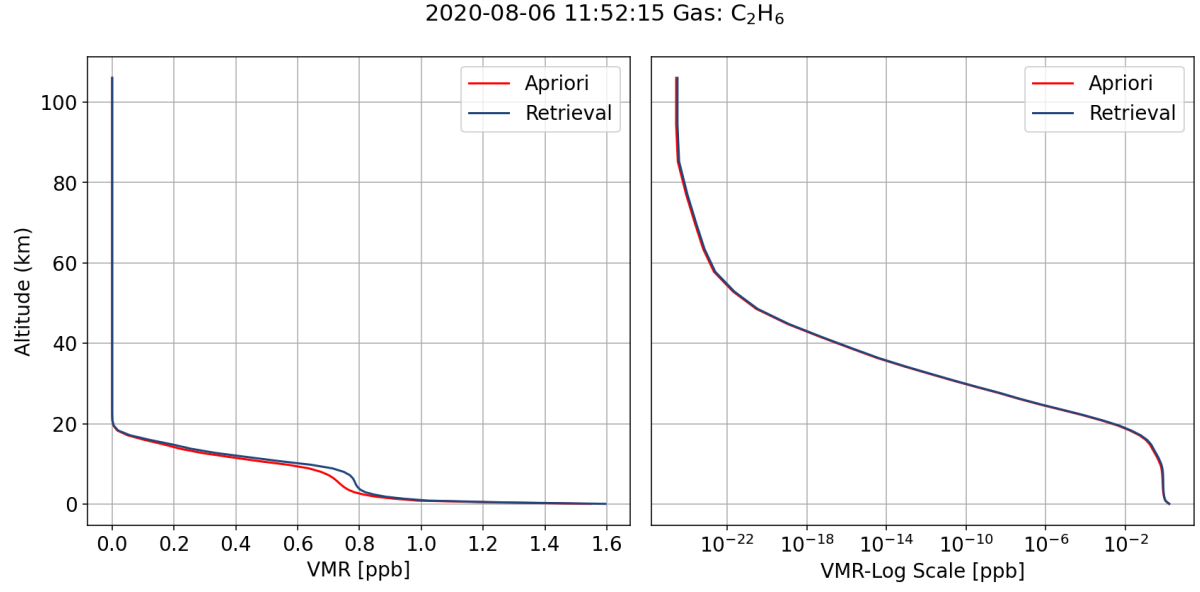


Figure A12: A priori (red) and retrieved (blue) C_2H_6 profiles of the spectrum shown above. Left: volume mixing ratio in normal scale. Right: volume mixing ratio in logarithmic scale.

https://doi.org/10.5194/essd-2026-762
Preprint. Discussion started: 6 November 2026
© Author(s) 2026. CC BY 4.0 License.

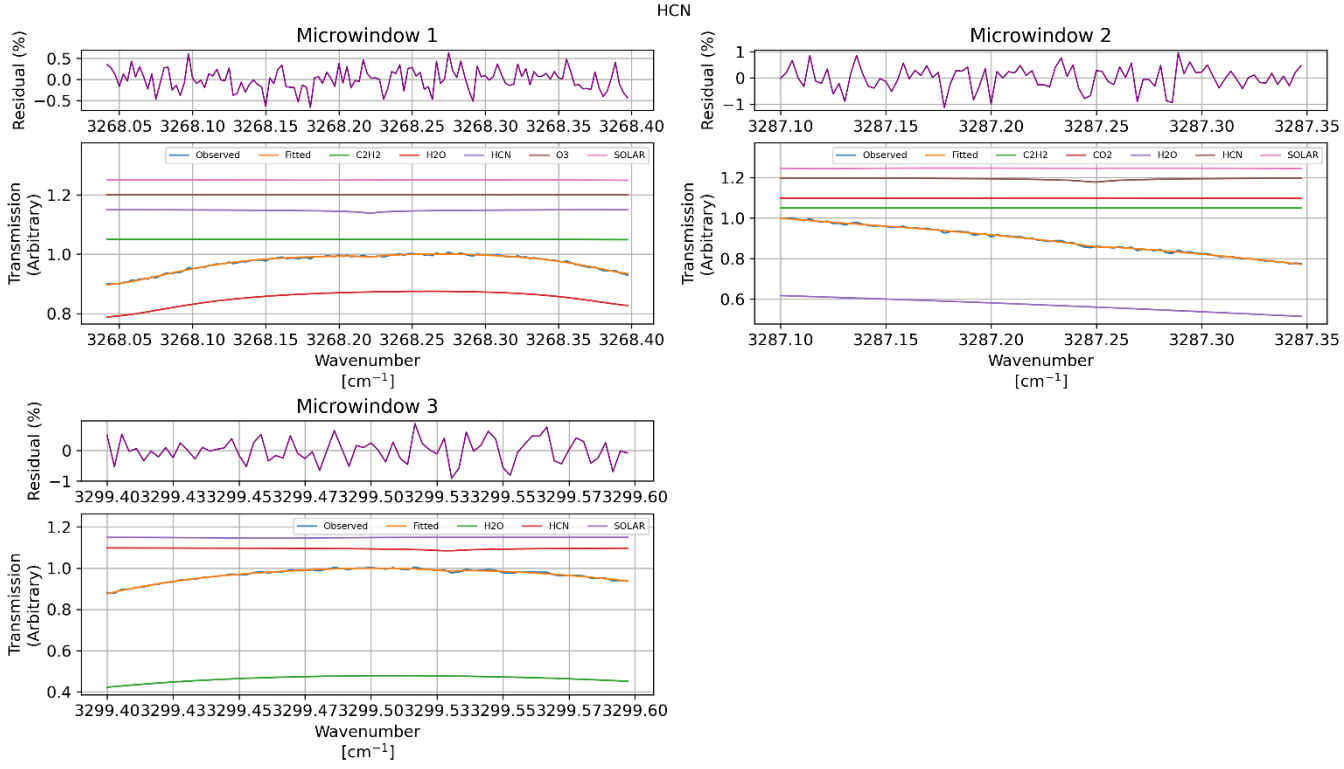


Figure A13: Measured (blue) and fitted (orange) spectrum in the 3 HCN MW's recorded on 6 of August 2020 at Paris. The residuals are shown in purple.

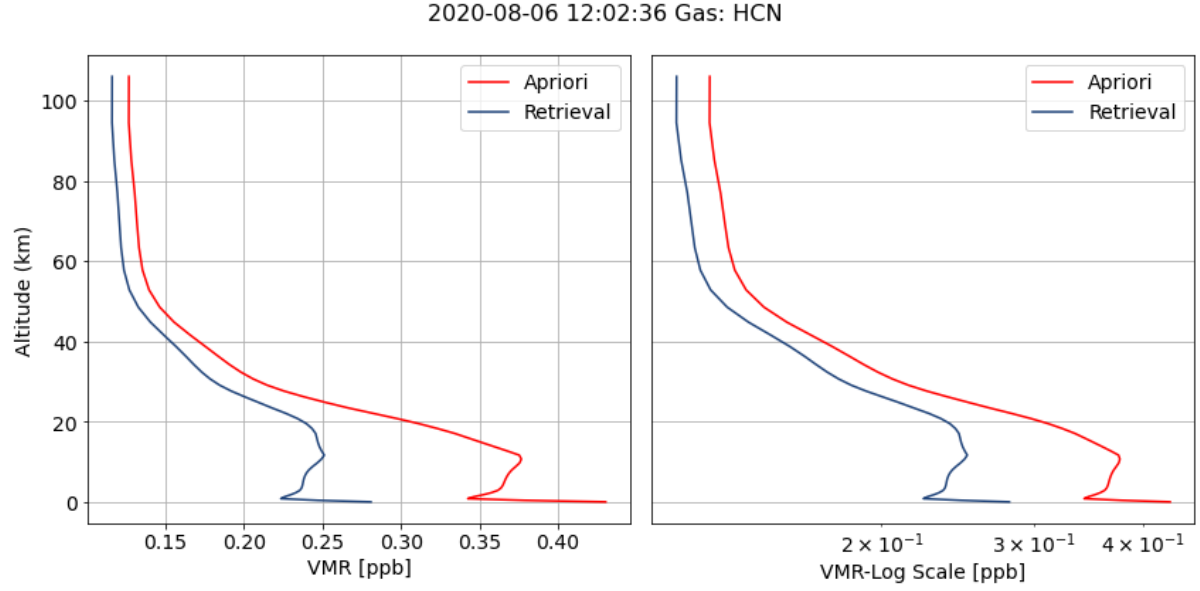


Figure A14: A priori (red) and retrieved (blue) HCN profiles of the spectrum shown above. Left: volume mixing ratio in normal scale. Right: volume mixing ratio in logarithmic scale.

https://doi.org/10.5194/essd-2026-762
Preprint. Discussion started: 6 November 2026
© Author(s) 2026. CC BY 4.0 License.

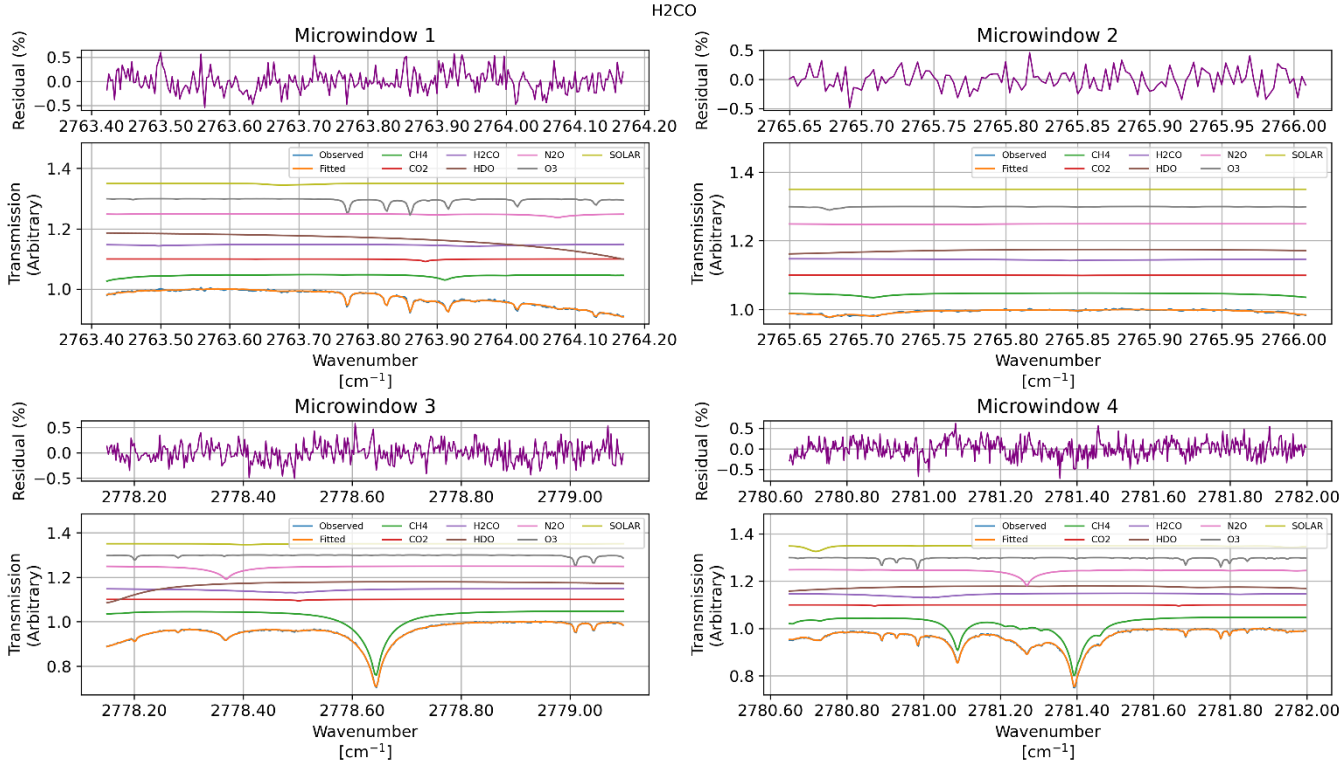


Figure A15: Measured (blue) and fitted (orange) spectrum in the 4 H_2CO MW's recorded on 6 of August 2020 at Paris. The residuals are shown in purple.

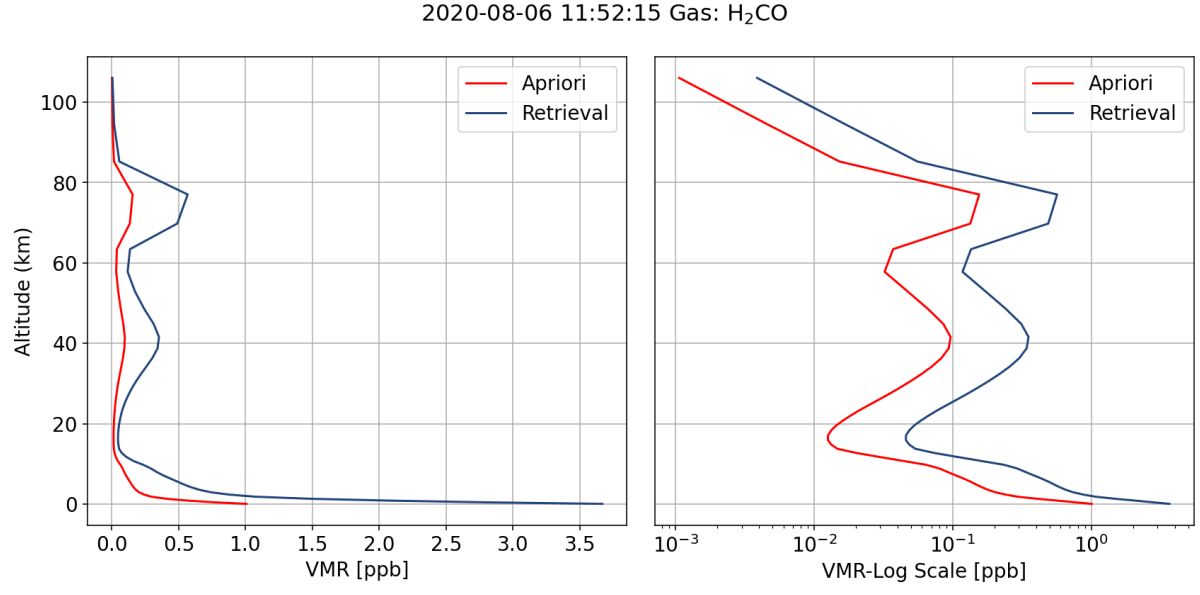


Figure A16: A priori (red) and retrieved (blue) H_2CO profiles of the spectrum shown above. Left: volume mixing ratio in normal scale. Right: volume mixing ratio in logarithmic scale.

https://doi.org/10.5194/essd-2026-762
Preprint. Discussion started: 6 November 2026
© Author(s) 2026. CC BY 4.0 License.

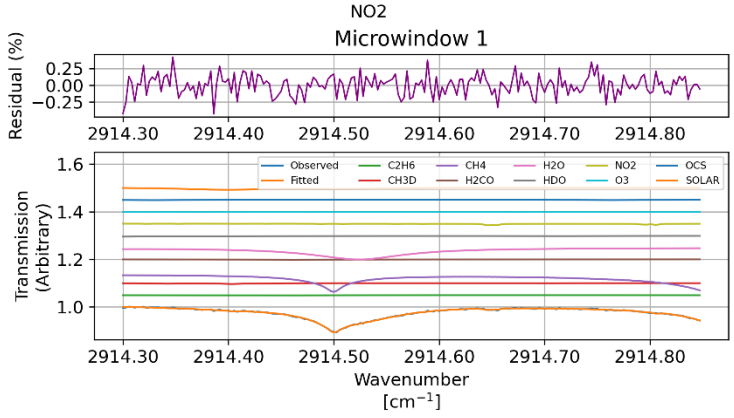


Figure A17: Measured (blue) and fitted (orange) spectrum in the NO_2 MW's recorded on 6 of August 2020 at Paris. The residuals are shown in purple.

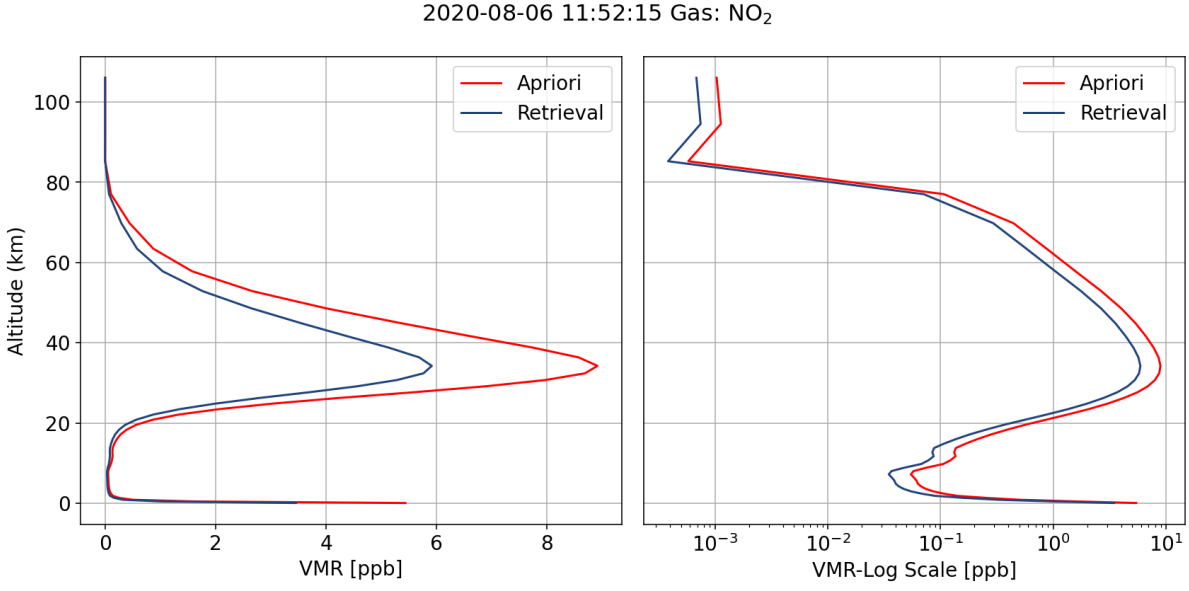


Figure A18: A priori (red) and retrieved (sky-blue) NO_2 profiles of the spectrum shown above. Left: volume mixing ratio in normal scale. Right: volume mixing ratio in logarithmic scale.

https://doi.org/10.5194/essd-2026-762
Preprint. Discussion started: 6 November 2026
© Author(s) 2026. CC BY 4.0 License.

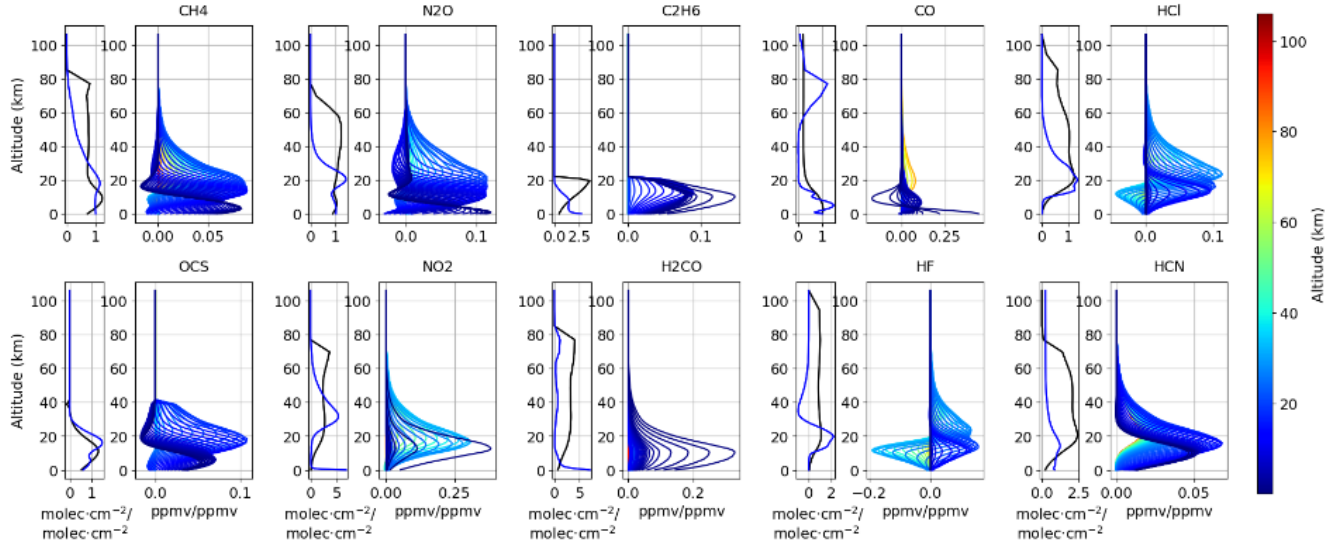


Figure A19: Averaging kernel (AVK) for the VMR profile retrieval of each gas at Paris using the final retrieval strategy. The plot shows AK rows indicating the sensitivities to anomalies in different altitudes (colours) of the true atmosphere. The AVK matrix has no unit, but is calculated for volume mixing ratios (ppmv/ppmv). Total column AVK (black) and Sum of AVK (blue).

Appendix B: SNR pre-retrieval filtering

As discussed in Section 4, spectra with SNR below 50 are excluded before the retrieval. The SNR is calculated from different signal and noise intervals for each NDACC filter, which are listed in Table A1.

Table A1: SNR calculation intervals for NDACC filters at Paris NDACC-IRWG site.

Optical filters	Signal interval (cm^{-1})	Noise interval (cm^{-1})
NDACC 01	4162.0 to 4162.4	3700.0 to 3750.0
NDACC 02	3160.0 to 3161.0	3700.0 to 3750.0
NDACC 05	2143.0 to 2143.5	2300.0 to 2350.0
NDACC 11	2610.0 to 2612.0	2300.0 to 2300.5

Author contributions

HF performed the SFIT4 retrievals, analysed the results, prepared the figures and tables, and wrote the draft manuscript. YT, CJ, PJ and HF designed the study. YT, CJ, PJ, CB, HF, CR, and PMJ contributed to the operation of the FTS-Paris instrument, its maintenance, and the data acquisition. JR and TAK contributed to the automation of the instrument and software, respectively. All authors reviewed and edited the manuscript.

https://doi.org/10.5194/essd-2026-762
Preprint. Discussion started: 6 November 2026
© Author(s) 2026. CC BY 4.0 License.



Competing interests

The contact author has declared that none of the authors has any competing interests.

Disclaimer

Copernicus Publications remains neutral with regard to jurisdictional claims made in the text, published maps, institutional affiliations, or any other geographical representation in this paper. While Copernicus Publications makes every effort to include appropriate place names, the final responsibility lies with the authors. Views expressed in the text are those of the authors and do not necessarily reflect the views of the publisher.

Acknowledgements

We would like to thank the China Scholarship Council (CSC) for financial support. The Paris site has received funding from Sorbonne Université, the French research center CNRS and the French space agency CNES. The authors would like to acknowledge the QUALAIR team and infrastructure for their scientific support. QUALAIR is an observation platform of the OSU Ecce Terra of Sorbonne University operated by LATMOS with the support of IPSL.

Financial support

This research has been supported by the China Scholarship Council (grant no. 202108070058). Operation of the FTS instrument at Paris is funded by Sorbonne Université, the French research organisation CNRS and the French space agency CNES.

References

Aigner, P., Makowski, M., Luther, A., Dietrich, F., and Chen, J.: Pyra: Automated EM27/SUN Greenhouse Gas Measurement Software, Journal of Open Source Software, 8, 5131, https://doi.org/10.21105/joss.05131, 2023.

Akishina, S., Polyakov, A., and Virolainen, Y.: Ground-based measurements of HF and HCl total columns in atmosphere near Saint Petersburg (2009–2023), International Journal of Remote Sensing, 45, 2315–2336, https://doi.org/10.1080/01431161.2024.2326536, 2024.

Angelbratt, J., Mellqvist, J., Blumenstock, T., Borsdorff, T., Brohede, S., Duchatelet, P., Forster, F., Hase, F., Mahieu, E., Murtagh, D., Petersen, A. K., Schneider, M., Sussmann, R., and Urban, J.: A new method to detect long term trends of methane (CH_4) and nitrous oxide (N_2O) total columns measured within the NDACC ground-based high resolution solar FTIR network, Atmospheric Chemistry and Physics, 11, 6167–6183, https://doi.org/10.5194/acp-11-6167-2011, 2011a.

Angelbratt, J., Mellqvist, J., Simpson, D., Jonson, J. E., Blumenstock, T., Borsdorff, T., Duchatelet, P., Forster, F., Hase, F., Mahieu, E., De Mazière, M., Notholt, J., Petersen, A. K., Raffalski, U., Servais, C., Sussmann, R., Warneke, T., and Vigouroux,

https://doi.org/10.5194/essd-2026-762
Preprint. Discussion started: 6 November 2026
© Author(s) 2026. CC BY 4.0 License.



C.: Carbon monoxide (CO) and ethane (C_2H_6) trends from ground-based solar FTIR measurements at six European stations, comparison and sensitivity analysis with the EMEP model, Atmospheric Chemistry and Physics, 11, 9253–9269, https://doi.org/10.5194/acp-11-9253-2011, 2011b.

Angot, H., Davel, C., Wiedinmyer, C., Pétron, G., Chopra, J., Hueber, J., Blanchard, B., Bourgeois, I., Vimont, I., Montzka, S. A., Miller, B. R., Elkins, J. W., and Helmig, D.: Temporary pause in the growth of atmospheric ethane and propane in 2015–2018, Atmos. Chem. Phys., 21, 15153–15170, https://doi.org/10.5194/acp-21-15153-2021, 2021.

Ayazpour, Z., González Abad, G., Nowlan, C. R., Sun, K., Kwon, H.-A., Chan Miller, C., Chong, H., Wang, H., Liu, X., Chance, K., O'Sullivan, E., Zhu, L., Vigouroux, C., De Smedt, I., Stremme, W., Hannigan, J. W., Notholt, J., Sun, X., Palm, M., Petri, C., Strong, K., Röhling, A. N., Mahieu, E., Smale, D., Té, Y., Morino, I., Murata, I., Nagahama, T., Kivi, R., Makarova, M., Jones, N., Sussmann, R., and Zhou, M.: Aura Ozone Monitoring Instrument (OMI) Collection 4 Formaldehyde Products, Earth and Space Science, 12, e2024EA003792, https://doi.org/10.1029/2024EA003792, 2025.

Bader, W., Bovy, B., Conway, S., Strong, K., Smale, D., Turner, A., Blumenstock, T., Boone, C., Collaud Coen, M., Coulon, A., García, O., Griffith, D., Hase, F., Hausmann, P., Jones, N., Krummel, P., Murata, I., Morino, I., Nakajima, H., and Mahieu, E.: The recent increase of atmospheric methane from 10 years of ground-based NDACC FTIR observations since 2005, Atmospheric Chemistry and Physics, 17, 2255–2277, https://doi.org/10.5194/acp-17-2255-2017, 2017.

Barret, B., Gouzenes, Y., Le Flochmoen, E., and Ferrant, S.: Retrieval of Metop-A/IASI N2O Profiles and Validation with NDACC FTIR Data, Atmosphere, 12, 219, https://doi.org/10.3390/atmos12020219, 2021.

Bell, R. J.: Introductory Fourier Transform Spectroscopy, https://doi.org/10.1016/B978-0-12-085150-8.X5001-3, 1972.

Buchholz, R. R., Deeter, M. N., Worden, H. M., Gille, J., Edwards, D. P., Hannigan, J. W., Jones, N. B., Paton-Walsh, C., Griffith, D. W. T., Smale, D., Robinson, J., Strong, K., Conway, S., Sussmann, R., Hase, F., Blumenstock, T., Mahieu, E., and Langerock, B.: Validation of MOPITT carbon monoxide using ground-based Fourier transform infrared spectrometer data from NDACC, Atmospheric Measurement Techniques, 10, 1927–1956, https://doi.org/10.5194/amt-10-1927-2017, 2017.

Chesnokova, T. Yu., Makarova, M. V., Chentsov, A. V., Kostsov, V. S., Poberovskii, A. V., Zakharov, V. I., and Rokotyan, N. V.: Estimation of the impact of differences in the CH_4 absorption line parameters on the accuracy of methane atmospheric total column retrievals from ground-based FTIR spectra, Journal of Quantitative Spectroscopy and Radiative Transfer, 254, 107187, https://doi.org/10.1016/j.jqsrt.2020.107187, 2020.

Chipperfield, M. P., Burton, M., Bell, W., Walsh, C. P., Blumenstock, T., Coffey, M. T., Hannigan, J. W., Mankin, W. G., Galle, B., Mellqvist, J., Mahieu, E., Zander, R., Notholt, J., Sen, B., and Toon, G. C.: On the use of HF as a reference for the comparison of stratospheric observations and models, J. Geophys. Res., 102, 12901–12919, https://doi.org/10.1029/96JD03964, 1997.

De Mazière, M., Thompson, A. M., Kurylo, M. J., Wild, J. D., Bernhard, G., Blumenstock, T., Braathen, G. O., Hannigan, J. W., Lambert, J.-C., Leblanc, T., McGee, T. J., Nedoluha, G., Petropavlovskikh, I., Seckmeyer, G., Simon, P. C., Steinbrecht, W., and Strahan, S. E.: The Network for the Detection of Atmospheric Composition Change (NDACC): history, status and perspectives, Atmospheric Chemistry and Physics, 18, 4935–4964, https://doi.org/10.5194/acp-18-4935-2018, 2018.

Diémoz, H., Siani, A. M., Casadio, S., Iannarelli, A. M., Casale, G. R., Savastiouk, V., Cede, A., Tiefengraber, M., and Müller, M.: Advanced NO_2 retrieval technique for the Brewer spectrophotometer applied to the 20-year record in Rome, Italy, Earth System Science Data, 13, 4929–4950, https://doi.org/10.5194/essd-13-4929-2021, 2021.

Duchon, C. E. and O'Malley, M. S.: Estimating Cloud Type from Pyranometer Observations, J. Appl. Meteorol., 38, 132–141, https://doi.org/10.1175/1520-0450(1999)038<0132:ECTFPO>2.0.CO;2, 1999.

https://doi.org/10.5194/essd-2026-762
Preprint. Discussion started: 6 November 2026
© Author(s) 2026. CC BY 4.0 License.

Franco, B., Bader, W., Toon, G. C., Bray, C., Perrin, A., Fischer, E. V., Sudo, K., Boone, C. D., Bovy, B., Lejeune, B., Servais, C., and Mahieu, E.: Retrieval of ethane from ground-based FTIR solar spectra using improved spectroscopy: Recent burden increase above Jungfraujoch, Journal of Quantitative Spectroscopy and Radiative Transfer, 160, 36–49, https://doi.org/10.1016/j.jqsrt.2015.03.017, 2015.

Franco, B., Mahieu, E., Emmons, L., Tzompa-Sosa, Z., Fischer, E., Sudo, K., Bovy, B., Conway, S., Griffin, D., Hannigan, J., Strong, K., and Walker, K.: Evaluating ethane and methane emissions associated with the development of oil and natural gas extraction in North America, Environmental Research Letters, 11, 044010, https://doi.org/10.1088/1748-9326/11/4/044010, 2016.

Friedrich, M., Beutner, E., Reuvers, H., Smeekes, S., Urbain, J.-P., Bader, W., Franco, B., Lejeune, B., and Mahieu, E.: A statistical analysis of time trends in atmospheric ethane, Climatic Change, 162, 105–125, https://doi.org/10.1007/s10584-020-02806-2, 2020.

Friedrich, M., Koopman, S. J., Lin, Y., Mahieu, E., Smeekes, S., De Mazière, M., Flood, V., Frey, M. M., Grutter, M., Hannigan, J. W., Hase, F., Jones, N., Kivi, R., Makarova, M., Morino, I., Murata, I., Nagahama, T., Notholt, J., Ortega, I., Prignon, M., Röhling, A. N., Smale, D., Strong, K., Té, Y., and Zhou, M.: Identifying trend reversals in atmospheric ethane from a multi-site analysis, Climatic Change, 179, 66, https://doi.org/10.1007/s10584-026-04153-0, 2026.

García, O. E., Schneider, M., Sepúlveda, E., Hase, F., Blumenstock, T., Cuevas, E., Ramos, R., Gross, J., Barthlott, S., Röhling, A. N., Sanromá, E., González, Y., Gómez-Peláez, Á. J., Navarro-Comas, M., Puentedura, O., Yela, M., Redondas, A., Carreño, V., León-Luis, S. F., Reyes, E., García, R. D., Rivas, P. P., Romero-Campos, P. M., Torres, C., Prats, N., Hernández, M., and López, C.: Twenty years of ground-based NDACC FTIR spectrometry at Izaña Observatory – overview and long-term comparison to other techniques, Atmos. Chem. Phys., 21, 15519–15554, https://doi.org/10.5194/acp-21-15519-2021, 2021.

Gettelman, A., Mills, M. J., Kinnison, D. E., Garcia, R. R., Smith, A. K., Marsh, D. R., Tilmes, S., Vitt, F., Bardeen, C. G., McInerny, J., Liu, H.-L., Solomon, S. C., Polvani, L. M., Emmons, L. K., Lamarque, J.-F., Richter, J. H., Glanville, A. S., Bacmeister, J. T., Phillips, A. S., Neale, R. B., Simpson, I. R., DuVivier, A. K., Hodzic, A., and Randel, W. J.: The Whole Atmosphere Community Climate Model Version 6 (WACCM6), Journal of Geophysical Research: Atmospheres, 124, 12380–12403, https://doi.org/10.1029/2019JD030943, 2019.

Gisi, M., Hase, F., Dohe, S., and Blumenstock, T.: Camtracker: a new camera controlled high precision solar tracker system for FTIR-spectrometers, Atmospheric Measurement Techniques, 4, 47–54, https://doi.org/10.5194/amt-4-47-2011, 2011.

Gordon, I. E., Rothman, L. S., Hargreaves, R. J., Hashemi, R., Karlovets, E. V., Skinner, F. M., Conway, E. K., Hill, C., Kochanov, R. V., Tan, Y., Wcisło, P., Finenko, A. A., Nelson, K., Bernath, P. F., Birk, M., Boudon, V., Campargue, A., Chance, K. V., Coustenis, A., Drouin, B. J., Flaud, B. J.-M., Gamache, R. R., Hodges, J. T., Jacquemart, D., Mlawer, E. J., Nikitin, A. V., Perevalov, V. I., Rotger, M., Tennyson, J., Toon, G. C., Tran, H., Tyuterev, V. G., Adkins, E. M., Baker, A., Barbe, A., Canè, E., Császár, A. G., Dudaryonok, A., Egorov, O., Fleisher, A. J., Fleurbaey, H., Foltynowicz, A., Furtenbacher, T., Harrison, J. J., Hartmann, J.-M., Horneman, V.-M., Huang, X., Karman, T., Karns, J., Kassi, S., Kleiner, I., Kofman, V., Kwabia-Tchana, F., Lavrentieva, N. N., Lee, T. J., Long, D. A., Lukashevskaya, A. A., Lyulin, O. M., Makhnev, V. Yu., Matt, W., Massie, S. T., Melosso, M., Mikhailenko, S. N., Mondelain, D., Müller, H. S. P., Naumenko, O. V., Perrin, A., Polyansky, O. L., Raddaoui, E., Raston, P. L., Reed, Z. D., Rey, M., Richard, C., Tóbiás, R., Sadiek, I., Schwenke, D. W., Starikova, E., Sung, K., Tamassia, F., Tashkun, S. A., Vander Auwera, J., Vasilenko, I. A., Vigasin, A. A., Villanueva, G. L., Vispoel, B., Wagner, G., Yachmenev, A., and Yurchenko, S. N.: The HITRAN2020 molecular spectroscopic database, Journal of Quantitative Spectroscopy and Radiative Transfer, 277, 107949, https://doi.org/10.1016/j.jqsrt.2021.107949, 2022.

Griffiths, P. R. and de Haseth, J. A.: Fourier Transform Infrared Spectrometry, 557, https://doi.org/10.1002/047010631X, 2006.

© Author(s) 2026. CC BY 4.0 License.

Guan, Y., Keppel-Aleks, G., Doney, S. C., Petri, C., Pollard, D., Wunch, D., Hase, F., Ohyama, H., Morino, I., Notholt, J., Shiomi, K., Strong, K., Kivi, R., Buschmann, M., Deutscher, N., Wennberg, P., Sussmann, R., Velazco, V. A., and Té, Y.: Characteristics of interannual variability in space-based XCO_2 global observations, Atmospheric Chemistry and Physics, 23, 5355–5372, https://doi.org/10.5194/acp-23-5355-2023, 2023.

Han, K. M.: Temporal Analysis of OMI-Observed Tropospheric NO_2 Columns over East Asia during 2006–2015, Atmosphere, 10, 658, https://doi.org/10.3390/atmos10110658, 2019.

Hannigan, J. W. and Mahieu, E.: IRWG 2023 Wrap-Up, NDACC-IRWG/TCCON/COCCON Annual Meeting 2023, Spa, Belgium, 16 June 2023, https://events.spacepole.be/event/160/page/316-agenda, 2023.

Hannigan, J. W., Ortega, I., Shams, S. B., Blumenstock, T., Campbell, J. E., Conway, S., Flood, V., Garcia, O., Griffith, D., Grutter, M., Hase, F., Jeseck, P., Jones, N., Mahieu, E., Makarova, M., De Mazière, M., Morino, I., Murata, I., Nagahama, T., Nakijima, H., Notholt, J., Palm, M., Poberovskii, A., Rettinger, M., Robinson, J., Röhling, A. N., Schneider, M., Servais, C., Smale, D., Stremme, W., Strong, K., Sussmann, R., Té, Y., Vigouroux, C., and Wizenberg, T.: Global Atmospheric OCS Trend Analysis From 22 NDACC Stations, Journal of Geophysical Research: Atmospheres, 127, e2021JD035764, https://doi.org/10.1029/2021JD035764, 2022a.

Hannigan, J. W., Palm, M., Ortega, I., and Langerock, B.: Infrared Working Group Retrieval Code, SFIT [code], https://wiki.ucar.edu/spaces/sfit4/overview (last access: 17 March 2025), 2022b.

Harrison, J. J., Allen, N. D. C., and Bernath, P. F.: Infrared absorption cross sections for ethane (C_2H_6) in the 3μm region, Journal of Quantitative Spectroscopy and Radiative Transfer, 111, 357–363, https://doi.org/10.1016/j.jqsrt.2009.09.010, 2010.

Hase, F., Blumenstock, T., and Paton-Walsh, C.: Analysis of the instrumental line shape of high-resolution Fourier transform IR spectrometers with gas cell measurements and new retrieval software, Appl. Opt., 38, 3417–3422, https://doi.org/10.1364/AO.38.003417, 1999.

Hase, F., Hannigan, J. W., Coffey, M. T., Goldman, A., Höpfner, M., Jones, N. B., Rinsland, C. P., and Wood, S. W.: Intercomparison of retrieval codes used for the analysis of high-resolution, ground-based FTIR measurements, Journal of Quantitative Spectroscopy and Radiative Transfer, 87, 25–52, https://doi.org/10.1016/j.jqsrt.2003.12.008, 2004.

Kipp & Zonen: SMP3-A Pyranometer, 4–20 mA, 10 m cable, Product Number 0374900-202, OTT HydroMet B.V., https://www.kippzonen.com/products/0374900-202 (last access: 8 July 2026), 2026.

Kohlhepp, R., Ruhnke, R., Chipperfield, M. P., De Mazière, M., Notholt, J., Barthlott, S., Batchelor, R. L., Blatherwick, R. D., Blumenstock, T., Coffey, M. T., Demoulin, P., Fast, H., Feng, W., Goldman, A., Griffith, D., Hamann, K., Hannigan, J. W., Hase, F., Jones, N., Kagawa, A., Kaiser, I., Kasai, Y., Kirner, O., Kouker, W., Lindenmaier, R., Mahieu, E., Mittermeier, R. L., Monge-Sanz, B., Morino, I., Murata, I., Nakajima, H., Palm, M., Murphy, H., Raffalski, U., Reddmann, T., Rettinger, M., Rinsland, C. P., Rozanov, E., Schneider, M., Senten, C., Servais, C., Sinnhuber, B. M., Smale, D., Strong, K., Sussmann, R., Taylor, J. R., Vanhaelewyn, G., Warneke, T., Whaley, C., Wiehle, M., and Wood, S. W.: Observed and simulated time evolution of HCl, $ClONO_2$, and HF total column abundances, Atmos. Chem. Phys., 12, 3527–3556, https://doi.org/10.5194/acp-12-3527-2012, 2012.

Koshelev, D.: First ground based FTIR-TCCON measurements of CO_2 in a European megacity : comparison with a rural site and validation of satellite measurements, PhD thesis, Sorbonne Université, Paris, France, https://theses.hal.science/tel-02890503, 2018.

Kwon, H.-A., Abad, G. G., Nowlan, C. R., Chong, H., Souri, A. H., Vigouroux, C., Röhling, A., Kivi, R., Makarova, M., Notholt, J., Palm, M., Winkler, H., Té, Y., Sussmann, R., Rettinger, M., Mahieu, E., Strong, K., Lutsch, E., Yamanouchi, S.,

https://doi.org/10.5194/essd-2026-762
Preprint. Discussion started: 6 November 2026
© Author(s) 2026. CC BY 4.0 License.



Nagahama, T., Hannigan, J. W., Zhou, M., Murata, I., Grutter, M., Stremme, W., De Mazière, M., Jones, N., Smale, D., and Morino, I.: Validation of OMPS Suomi NPP and OMPS NOAA-20 Formaldehyde Total Columns With NDACC FTIR Observations, Earth and Space Science, 10, e2022EA002778, https://doi.org/10.1029/2022EA002778, 2023.

Laughner, J. L., Toon, G. C., Mendonca, J., Petri, C., Roche, S., Wunch, D., Blavier, J.-F., Griffith, D. W. T., Heikkinen, P., Keeling, R. F., Kiel, M., Kivi, R., Roehl, C. M., Stephens, B. B., Baier, B. C., Chen, H., Choi, Y., Deutscher, N. M., DiGangi, J. P., Gross, J., Herkommer, B., Jeseck, P., Laemmel, T., Lan, X., McGee, E., McKain, K., Miller, J., Morino, I., Notholt, J., Ohyama, H., Pollard, D. F., Rettinger, M., Riris, H., Rousogenous, C., Sha, M. K., Shiomi, K., Strong, K., Sussmann, R., Té, Y., Velazco, V. A., Wofsy, S. C., Zhou, M., and Wennberg, P. O.: The Total Carbon Column Observing Network's GGG2020 data version, Earth System Science Data, 16, 2197–2260, https://doi.org/10.5194/essd-16-2197-2024, 2024.

Lieschke, K. J., Fisher, J. A., Paton-Walsh, C., Jones, N. B., Greenslade, J. W., Burden, S., and Griffith, D. W. T.: Decreasing Trend in Formaldehyde Detected From 20-Year Record at Wollongong, Southeast Australia, Geophysical Research Letters, 46, 8464–8473, https://doi.org/10.1029/2019GL083757, 2019.

Luecken, D. J., Napelenok, S. L., Strum, M., Scheffe, R., and Phillips, S.: Sensitivity of Ambient Atmospheric Formaldehyde and Ozone to Precursor Species and Source Types Across the United States, Environ. Sci. Technol., 52, 4668–4675, https://doi.org/10.1021/acs.est.7b05509, 2018.

Mahieu, E., Duchatelet, P., Demoulin, P., Walker, K. A., Dupuy, E., Froidevaux, L., Randall, C., Catoire, V., Strong, K., Boone, C. D., Bernath, P. F., Blavier, J.-F., Blumenstock, T., Coffey, M., De Mazière, M., Griffith, D., Hannigan, J., Hase, F., Jones, N., Jucks, K. W., Kagawa, A., Kasai, Y., Mebarki, Y., Mikuteit, S., Nassar, R., Notholt, J., Rinsland, C. P., Robert, C., Schrems, O., Senten, C., Smale, D., Taylor, J., Tétard, C., Toon, G. C., Warneke, T., Wood, S. W., Zander, R., and Servais, C.: Validation of ACE-FTS v2.2 measurements of HCl, HF, CCl_3F and CCl_2F_2 using space-, balloon- and ground-based instrument observations, Atmospheric Chemistry and Physics, 8, 6199–6221, https://doi.org/10.5194/acp-8-6199-2008, 2008.

Mahieu, E., Chipperfield, M. P., Notholt, J., Reddmann, T., Anderson, J., Bernath, P. F., Blumenstock, T., Coffey, M. T., Dhomse, S. S., Feng, W., Franco, B., Froidevaux, L., Griffith, D. W. T., Hannigan, J. W., Hase, F., Hossaini, R., Jones, N. B., Morino, I., Murata, I., Nakajima, H., Palm, M., Paton-Walsh, C., Russell III, J. M., Schneider, M., Servais, C., Smale, D., and Walker, K. A.: Recent Northern Hemisphere stratospheric HCl increase due to atmospheric circulation changes, Nature, 515, 104–107, https://doi.org/10.1038/nature13857, 2014.

Marsh, D. R., Mills, M. J., Kinnison, D. E., Lamarque, J.-F., Calvo, N., and Polvani, L. M.: Climate Change from 1850 to 2005 Simulated in CESM1(WACCM), J. Climate, 26, 7372–7391, https://doi.org/10.1175/JCLI-D-12-00558.1, 2013.

Meyers, T. P. and Dale, R. F.: Predicting Daily Insolation with Hourly Cloud Height and Coverage, J. Climate Appl. Meteor., 22, 537–545, https://doi.org/10.1175/1520-0450(1983)022<0537:PDIWHC>2.0.CO;2, 1983.

Müller, J.-F., Stavrakou, T., Oomen, G.-M., Opacka, B., De Smedt, I., Guenther, A., Vigouroux, C., Langerock, B., Aquino, C. A. B., Grutter, M., Hannigan, J., Hase, F., Kivi, R., Lutsch, E., Mahieu, E., Makarova, M., Metzger, J.-M., Morino, I., Murata, I., Nagahama, T., Notholt, J., Ortega, I., Palm, M., Röhling, A., Stremme, W., Strong, K., Sussmann, R., Té, Y., and Fried, A.: Bias correction of OMI HCHO columns based on FTIR and aircraft measurements and impact on top-down emission estimates, Atmospheric Chemistry and Physics, 24, 2207–2237, https://doi.org/10.5194/acp-24-2207-2024, 2024.

Oomen, G.-M., Müller, J.-F., Stavrakou, T., De Smedt, I., Blumenstock, T., Kivi, R., Makarova, M., Palm, M., Röhling, A., Té, Y., Vigouroux, C., Friedrich, M. M., Frieß, U., Hendrick, F., Merlaud, A., Piters, A., Richter, A., Van Roozendael, M., and Wagner, T.: Weekly derived top-down volatile-organic-compound fluxes over Europe from TROPOMI HCHO data from 2018 to 2021, Atmospheric Chemistry and Physics, 24, 449–474, https://doi.org/10.5194/acp-24-449-2024, 2024.

https://doi.org/10.5194/essd-2026-762
Preprint. Discussion started: 6 November 2026
© Author(s) 2026. CC BY 4.0 License.



Ortega, I., Buchholz, R. R., Hall, E. G., Hurst, D. F., Jordan, A. F., and Hannigan, J. W.: Tropospheric water vapor profiles obtained with FTIR: comparison with balloon-borne frost point hygrometers and influence on trace gas retrievals, Atmospheric Measurement Techniques, 12, 873–890, https://doi.org/10.5194/amt-12-873-2019, 2019.

Ortega, I., Gaubert, B., Hannigan, J. W., Brasseur, G., Worden, H. M., Blumenstock, T., Fu, H., Hase, F., Jeseck, P., Jones, N., Liu, C., Mahieu, E., Morino, I., Murata, I., Notholt, J., Palm, M., Röhling, A., Té, Y., Strong, K., Sun, Y., and Yamanouchi, S.: Anomalies of O_3, CO, C_2H_2, H_2CO, and C_2H_6 detected with multiple ground-based Fourier-transform infrared spectrometers and assessed with model simulation in 2020: COVID-19 lockdowns versus natural variability, Elem Sci Anth, 11, 00015, https://doi.org/10.1525/elementa.2023.00015, 2023.

Ortega, I., Hannigan, J. W., Baier, B. C., McKain, K., and Smale, D.: Advancing CH_4 and N_2O retrieval strategies for NDACC/IRWG FTIR observations with the support of airborne in situ measurements, Atmospheric Measurement Techniques, 18, 2353–2371, https://doi.org/10.5194/amt-18-2353-2025, 2025.

Phillips, D. L.: A Technique for the Numerical Solution of Certain Integral Equations of the First Kind, J. ACM, 9, 84–97, https://doi.org/10.1145/321105.321114, 1962.

Pougatchev, N. S., Connor, B. J., and Rinsland, C. P.: Infrared measurements of the ozone vertical distribution above Kitt Peak, Journal of Geophysical Research: Atmospheres, 100, 16689–16697, https://doi.org/10.1029/95JD01296, 1995.

Rinsland, C. P., Levine, J. S., Goldman, A., Sze, N. D., Ko, M. K. W., and Johnson, D. W.: Infrared measurements of HF and HCl total column abundances above Kitt Peak, 1977–1990: Seasonal cycles, long-term increases, and comparisons with model calculations, Journal of Geophysical Research: Atmospheres, 96, 15523–15540, https://doi.org/10.1029/91JD01249, 1991.

Rinsland, C. P., Jones, N. B., Connor, B. J., Logan, J. A., Pougatchev, N. S., Goldman, A., Murcray, F. J., Stephen, T. M., Pine, A. S., Zander, R., Mahieu, E., and Demoulin, P.: Northern and southern hemisphere ground-based infrared spectroscopic measurements of tropospheric carbon monoxide and ethane, Journal of Geophysical Research: Atmospheres, 103, 28197–28217, https://doi.org/10.1029/98JD02515, 1998.

Rinsland, C. P., Mahieu, E., Zander, R., Demoulin, P., Forrer, J., and Buchmann, B.: Free tropospheric CO, C_2H_6, and HCN above central Europe: Recent measurements from the Jungfraujoch station including the detection of elevated columns during 1998, Journal of Geophysical Research: Atmospheres, 105, 24235–24249, https://doi.org/10.1029/2000JD900371, 2000.

Rinsland, C. P., Meier, A., Griffith, D. W. T., and Chiou, L. S.: Ground-based measurements of tropospheric CO, C_2H_6, and HCN from Australia at 34°S latitude during 1997–1998, Journal of Geophysical Research: Atmospheres, 106, 20913–20924, https://doi.org/10.1029/2000JD000318, 2001.

Rodgers, C. D.: Inverse Methods for Atmospheric Sounding: Theory and Practice, WORLD SCIENTIFIC, https://doi.org/10.1142/3171, 2000.

Rothman, L. S., Gordon, I. E., Barbe, A., Benner, D. C., Bernath, P. F., Birk, M., Boudon, V., Brown, L. R., Campargue, A., Champion, J.-P., Chance, K., Coudert, L. H., Dana, V., Devi, V. M., Fally, S., Flaud, J.-M., Gamache, R. R., Goldman, A., Jacquemart, D., Kleiner, I., Lacome, N., Lafferty, W. J., Mandin, J.-Y., Massie, S. T., Mikhailenko, S. N., Miller, C. E., Moazzen-Ahmadi, N., Naumenko, O. V., Nikitin, A. V., Orphal, J., Perevalov, V. I., Perrin, A., Predoi-Cross, A., Rinsland, C. P., Rotger, M., Šimečková, M., Smith, M. A. H., Sung, K., Tashkun, S. A., Tennyson, J., Toth, R. A., Vandaele, A. C., and Vander Auwera, J.: The HITRAN 2008 molecular spectroscopic database, Journal of Quantitative Spectroscopy and Radiative Transfer, 110, 533–572, https://doi.org/10.1016/j.jqsrt.2009.02.013, 2009.

Rozé, J., Jeseck, P., Rouillé, C., Marie-Jeanne, P., Boursier, C., Té, Y.-V., Fu, H., and Janssen, C.: FTSpectRA - a new software for the automation of the FTS-Paris measurements, poster presented at the NDACC/IRWG-TCCON-COCCON Annual

© Author(s) 2026. CC BY 4.0 License.

Meeting 2024, NSF NCAR Mesa Laboratory, Boulder, CO, USA, 8-12 July 2024, https://www2.acom.ucar.edu/sites/default/files/2024-07/Posters-NDACC_IRWG-TCCON-COCCON%20Annual%20Meeting%20224_0.pdf, 2024.

Schneider, P., Lahoz, W. A., and van der A, R.: Recent satellite-based trends of tropospheric nitrogen dioxide over large urban agglomerations worldwide, Atmospheric Chemistry and Physics, 15, 1205–1220, https://doi.org/10.5194/acp-15-1205-2015, 2015.

Sha, M. K., Langerock, B., Blavier, J.-F. L., Blumenstock, T., Borsdorff, T., Buschmann, M., Dehn, A., De Mazière, M., Deutscher, N. M., Feist, D. G., García, O. E., Griffith, D. W. T., Grutter, M., Hannigan, J. W., Hase, F., Heikkinen, P., Hermans, C., Iraci, L. T., Jeseck, P., Jones, N., Kivi, R., Kumps, N., Landgraf, J., Lorente, A., Mahieu, E., Makarova, M. V., Mellqvist, J., Metzger, J.-M., Morino, I., Nagahama, T., Notholt, J., Ohyama, H., Ortega, I., Palm, M., Petri, C., Pollard, D. F., Rettinger, M., Robinson, J., Roche, S., Roehl, C. M., Röhling, A. N., Rousogenous, C., Schneider, M., Shiomi, K., Smale, D., Stremme, W., Strong, K., Sussmann, R., Té, Y., Uchino, O., Velazco, V. A., Vigouroux, C., Vrekoussis, M., Wang, P., Warneke, T., Wizenberg, T., Wunch, D., Yamanouchi, S., Yang, Y., and Zhou, M.: Validation of methane and carbon monoxide from Sentinel-5 Precursor using TCCON and NDACC-IRWG stations, Atmos. Meas. Tech., 14, 6249–6304, https://doi.org/10.5194/amt-14-6249-2021, 2021.

Smale, D., Sherlock, V., Griffith, D. W. T., Moss, R., Brailsford, G., Nichol, S., and Kotkamp, M.: A decade of CH_4, CO and N_2O in situ measurements at Lauder, New Zealand: assessing the long-term performance of a Fourier transform infrared trace gas and isotope analyser, Atmospheric Measurement Techniques, 12, 637–673, https://doi.org/10.5194/amt-12-637-2019, 2019.

Steck, T.: Methods for determining regularization for atmospheric retrieval problems, Appl. Opt., 41, 1788, https://doi.org/10.1364/AO.41.001788, 2002.

Steffen, J., Bernath, P. F., and Boone, C. D.: Trends in halogen-containing molecules measured by the Atmospheric Chemistry Experiment (ACE) satellite, Journal of Quantitative Spectroscopy and Radiative Transfer, 238, 106619, https://doi.org/10.1016/j.jqsrt.2019.106619, 2019.

Sun, Y., Yin, H., Liu, C., Mahieu, E., Notholt, J., Té, Y., Lu, X., Palm, M., Wang, W., Shan, C., Hu, Q., Qin, M., Tian, Y., and Zheng, B.: The reduction in C_2H_6 from 2015 to 2020 over Hefei, eastern China, points to air quality improvement in China, Atmospheric Chemistry and Physics, 21, 11759–11779, https://doi.org/10.5194/acp-21-11759-2021, 2021.

Sun, Y., Yin, H., Wang, W., Shan, C., and Liu, C.: Ground-based remote sensing of nitrous oxide (N2O) over Hefei, eastern China from high-resolution solar spectra, Geo-spatial Information Science, 0, 1–12, https://doi.org/10.1080/10095020.2023.2208616, 2023.

Sussmann, R., Forster, F., Rettinger, M., and Jones, N.: Strategy for high-accuracy-and-precision retrieval of atmospheric methane from the mid-infrared FTIR network, Atmospheric Measurement Techniques, 4, 1943–1964, https://doi.org/10.5194/amt-4-1943-2011, 2011.

Taylor, T. E., O'Dell, C. W., Crisp, D., Kuze, A., Lindqvist, H., Wennberg, P. O., Chatterjee, A., Gunson, M., Eldering, A., Fisher, B., Kiel, M., Nelson, R. R., Merrelli, A., Osterman, G., Chevallier, F., Palmer, P. I., Feng, L., Deutscher, N. M., Dubey, M. K., Feist, D. G., García, O. E., Griffith, D. W. T., Hase, F., Iraci, L. T., Kivi, R., Liu, C., De Mazière, M., Morino, I., Notholt, J., Oh, Y.-S., Ohyama, H., Pollard, D. F., Rettinger, M., Schneider, M., Roehl, C. M., Sha, M. K., Shiomi, K., Strong, K., Sussmann, R., Té, Y., Velazco, V. A., Vrekoussis, M., Warneke, T., and Wunch, D.: An 11-year record of XCO_2 estimates derived from GOSAT measurements using the NASA ACOS version 9 retrieval algorithm, Earth System Science Data, 14, 325–360, https://doi.org/10.5194/essd-14-325-2022, 2022.

https://doi.org/10.5194/essd-2026-762
Preprint. Discussion started: 6 November 2026
© Author(s) 2026. CC BY 4.0 License.

Té, Y., Jeseck, P., Payan, S., Pépin, I., and Camy-Peyret, C.: The Fourier transform spectrometer of the Université Pierre et Marie Curie QualAir platform, Rev Sci Instrum, 81, 103102, https://doi.org/10.1063/1.3488357, 2010.

Té, Y., Dieudonné, E., Jeseck, P., Hase, F., Hadji-Lazaro, J., Clerbaux, C., Ravetta, F., Payan, S., Pépin, I., Hurtmans, D., Pelon, J., and Camy-Peyret, C.: Carbon Monoxide Urban Emission Monitoring: A Ground-Based FTIR Case Study, Journal of Atmospheric and Oceanic Technology, 29, 911–921, https://doi.org/10.1175/JTECH-D-11-00040.1, 2012.

Té, Y., Jeseck, P., Franco, B., Mahieu, E., Jones, N., Paton-Walsh, C., Griffith, D. W. T., Buchholz, R. R., Hadji-Lazaro, J., Hurtmans, D., and Janssen, C.: Seasonal variability of surface and column carbon monoxide over the megacity Paris, high-altitude Jungfraujoch and Southern Hemispheric Wollongong stations, Atmos. Chem. Phys., 16, 10911–10925, https://doi.org/10.5194/acp-16-10911-2016, 2016.

Té, Y., Jeseck, P., and Janssen, C.: TCCON data from Paris (FR), Release GGG2020.R0 (Version R0), CaltechData [Dataset], https://doi.org/10.14291/TCCON.GGG2020.PARIS01.R0, 2025.

Té, Y., Fu, H., Jeseck, P., Boursier, C., and Janssen, C.: FTS-PARIS OCS, HF, C_2H_6, CH_4, CO, H_2CO, HCl, HCN, N_2O, NO_2 total columns from 2011 to 2022, Zenodo [Dataset], https://doi.org/10.5281/zenodo.23359690, 2026.

Tian, Y., Sun, Y., Liu, C., Wang, W., Shan, C., Xu, X., and Hu, Q.: Characterisation of methane variability and trends from near-infrared solar spectra over Hefei, China, Atmospheric Environment, 173, 198–209, https://doi.org/10.1016/j.atmosenv.2017.11.001, 2018.

Tikhonov, A. N.: On the solution of ill-posed problems and the method of regularization, Dokl. Akad. Nauk SSSR, 151, 501–504, https://www.mathnet.ru/eng/dan28329, 1963.

Timofeyev, Y., Virolainen, Y., Makarova, M., Poberovsky, A., Polyakov, A., Ionov, D., Osipov, S., and Imhasin, H.: Ground-based spectroscopic measurements of atmospheric gas composition near Saint Petersburg (Russia), Journal of Molecular Spectroscopy, 323, 2–14, https://doi.org/10.1016/j.jms.2015.12.007, 2016.

Tsuruta, A., Kuze, A., Shiomi, K., Kataoka, F., Kikuchi, N., Aalto, T., Backman, L., Kivimäki, E., Tenkanen, M. K., McKain, K., García, O. E., Hase, F., Kivi, R., Morino, I., Ohyama, H., Pollard, D. F., Sha, M. K., Strong, K., Sussmann, R., Té, Y., Velazco, V. A., Vrekoussis, M., Warneke, T., Zhou, M., and Suto, H.: Global CH_4 Fluxes Derived from JAXA/GOSAT Lower Tropospheric Partial Column Data and the CTE-CH_4 Atmospheric Inverse Model, Atmos. Chem. Phys., 25, 15527–15565, https://doi.org/10.5194/acp-25-15527-2025, 2025.

Viatte, C., Strong, K., Paton-Walsh, C., Mendonca, J., O'Neill, N. T., and Drummond, J. R.: Measurements of CO, HCN, and C_2H_6 Total Columns in Smoke Plumes Transported from the 2010 Russian Boreal Forest Fires to the Canadian High Arctic, Atmosphere-Ocean, 51, 522–531, https://doi.org/10.1080/07055900.2013.823373, 2013.

Viatte, C., Strong, K., Walker, K. A., and Drummond, J. R.: Five years of CO, HCN, C_2H_6, C_2H_2, CH_3OH, HCOOH and H_2CO total columns measured in the Canadian high Arctic, Atmospheric Measurement Techniques, 7, 1547–1570, https://doi.org/10.5194/amt-7-1547-2014, 2014.

Vigouroux, C., Bauer Aquino, C. A., Bauwens, M., Becker, C., Blumenstock, T., De Mazière, M., García, O., Grutter, M., Guarin, C., Hannigan, J., Hase, F., Jones, N., Kivi, R., Koshelev, D., Langerock, B., Lutsch, E., Makarova, M., Metzger, J.-M., Müller, J.-F., Notholt, J., Ortega, I., Palm, M., Paton-Walsh, C., Poberovskii, A., Rettinger, M., Robinson, J., Smale, D., Stavrakou, T., Stremme, W., Strong, K., Sussmann, R., Té, Y., and Toon, G.: NDACC harmonized formaldehyde time series from 21 FTIR stations covering a wide range of column abundances, Atmospheric Measurement Techniques, 11, 5049–5073, https://doi.org/10.5194/amt-11-5049-2018, 2018.

https://doi.org/10.5194/essd-2026-762
Preprint. Discussion started: 6 November 2026
© Author(s) 2026. CC BY 4.0 License.



Voshtani, S., Jones, D. B. A., Wunch, D., Pendergrass, D. C., Wennberg, P. O., Pollard, D. F., Morino, I., Ohyama, H., Deutscher, N. M., Hase, F., Sussmann, R., Weidmann, D., Kivi, R., García, O., Té, Y., Chen, J., Anderson, K., Stevens, R., Kondragunta, S., Zhu, A., Worthy, D., Racki, S., McKain, K., Makarova, M. V., Jones, N., Mahieu, E., Cadena-Caicedo, A., Cristofanelli, P., Labuschagne, C., Kozlova, E., Seitz, T., Steinbacher, M., Mahdi, R., and Murata, I.: Quantifying CO emissions from boreal wildfires by assimilating TROPOMI and TCCON observations, EGUsphere, 1–60, https://doi.org/10.5194/egusphere-2025-858, 2025.

Whaley, C.: Improvements to our Understanding of Toronto-area Atmospheric Composition, PhD thesis, University of Toronto, Toronto, Canada, https://hdl.handle.net/1807/68411, 2014.

Wizenberg, T., Strong, K., Jones, D. B. A., Hannigan, J. W., Ortega, I., and Mahieu, E.: Measured and Modeled Trends of Seven Tropospheric Pollutants in the High Arctic From 1999 to 2022, Journal of Geophysical Research: Atmospheres, 129, e2023JD040544, https://doi.org/10.1029/2023JD040544, 2024.

Wunch, D., Toon, G. C., Blavier, J.-F. L., Washenfelder, R. A., Notholt, J., Connor, B. J., Griffith, D. W. T., Sherlock, V., and Wennberg, P. O.: The Total Carbon Column Observing Network, Philosophical Transactions of the Royal Society A: Mathematical, Physical and Engineering Sciences, 369, 2087–2112, https://doi.org/10.1098/rsta.2010.0240, 2011.

Wunch, D., Toon, G. C., Hedelius, J. K., Vizenor, N., Roehl, C. M., Saad, K. M., Blavier, J.-F. L., Blake, D. R., and Wennberg, P. O.: Quantifying the loss of processed natural gas within California's South Coast Air Basin using long-term measurements of ethane and methane, Atmospheric Chemistry and Physics, 16, 14091–14105, https://doi.org/10.5194/acp-16-14091-2016, 2016.

Yamanouchi, S., Strong, K., Colebatch, O., Conway, S., Jones, D. B. A., Lutsch, E., and Roche, S.: Atmospheric trace gas trends obtained from FTIR column measurements in Toronto, Canada from 2002-2019, Environ. Res. Commun., 3, 051002, https://doi.org/10.1088/2515-7620/abfa65, 2021.

Yamanouchi, S., Conway, S., Strong, K., Colebatch, O., Lutsch, E., Roche, S., Taylor, J., Whaley, C. H., and Wiacek, A.: Network for the Detection of Atmospheric Composition Change (NDACC) Fourier transform infrared (FTIR) trace gas measurements at the University of Toronto Atmospheric Observatory from 2002 to 2020, Earth System Science Data, 15, 3387–3418, https://doi.org/10.5194/essd-15-3387-2023, 2023.

Yin, H., Sun, Y., Liu, C., Lu, X., Smale, D., Blumenstock, T., Nagahama, T., Wang, W., Tian, Y., Hu, Q., Shan, C., Zhang, H., and Liu, J.: Ground-based FTIR observation of hydrogen chloride (HCl) over Hefei, China, and comparisons with GEOS-Chem model data and other ground-based FTIR stations data, Opt. Express, 28, 8041–8055, https://doi.org/10.1364/OE.384377, 2020.

Zeng, G., Wood, S. W., Morgenstern, O., Jones, N. B., Robinson, J., and Smale, D.: Trends and variations in CO, C_2H_6, and HCN in the Southern Hemisphere point to the declining anthropogenic emissions of CO and C_2H_6, Atmospheric Chemistry and Physics, 12, 7543–7555, https://doi.org/10.5194/acp-12-7543-2012, 2012.

Zhou, M., Vigouroux, C., Langerock, B., Wang, P., Dutton, G., Hermans, C., Kumps, N., Metzger, J.-M., Toon, G., and De Mazière, M.: CFC-11, CFC-12 and HCFC-22 ground-based remote sensing FTIR measurements at Réunion Island and comparisons with MIPAS/ENVISAT data, Atmospheric Measurement Techniques, 9, 5621–5636, https://doi.org/10.5194/amt-9-5621-2016, 2016.

Zhou, M., Langerock, B., Vigouroux, C., Sha, M. K., Ramonet, M., Delmotte, M., Mahieu, E., Bader, W., Hermans, C., Kumps, N., Metzger, J.-M., Duflot, V., Wang, Z., Palm, M., and De Mazière, M.: Atmospheric CO and CH_4 time series and seasonal variations on Reunion Island from ground-based in situ and FTIR (NDACC and TCCON) measurements, Atmospheric Chemistry and Physics, 18, 13881–13901, https://doi.org/10.5194/acp-18-13881-2018, 2018.

https://doi.org/10.5194/essd-2026-762
Preprint. Discussion started: 6 November 2026
© Author(s) 2026. CC BY 4.0 License.



Zhu, Q., Wang, W., Shan, C., Xie, Y., Zeng, X., Wu, P., Liang, B., and Liu, C.: Effects of biomass burning on CO, HCN, C_2H_6, C_2H_2 and H_2CO during long-term FTIR measurements in Hefei, China, Opt. Express, 32, 8343–8363, https://doi.org/10.1364/OE.516258, 2024.

1305